

DESY 05-011
January 2005

Study of deep inelastic inclusive and diffractive scattering with the ZEUS forward plug calorimeter

ZEUS Collaboration

Abstract

Deep inelastic scattering and its diffractive component, $ep \rightarrow e'\gamma^*p \rightarrow e'XN$, have been studied at HERA with the ZEUS detector using an integrated luminosity of 4.2 pb^{-1} . The measurement covers a wide range in the γ^*p c.m. energy W (37 - 245 GeV), photon virtuality Q^2 (2.2 - 80 GeV^2) and mass M_X . The diffractive cross section for $M_X > 2 \text{ GeV}$ rises strongly with W ; the rise is steeper with increasing Q^2 . The latter observation excludes the description of diffractive deep inelastic scattering in terms of the exchange of a single Pomeron. The ratio of diffractive to total cross section is constant as a function of W , in contradiction to the expectation of Regge phenomenology combined with a naive extension of the optical theorem to γ^*p scattering. Above M_X of 8 GeV, the ratio is flat with Q^2 , indicating a leading-twist behaviour of the diffractive cross section. The data are also presented in terms of the diffractive structure function, $F_2^{D(3)}(\beta, x_{_P}, Q^2)$, of the proton. For fixed β , the Q^2 dependence of $x_{_P}F_2^{D(3)}$ changes with $x_{_P}$ in violation of Regge factorisation. For fixed $x_{_P}$, $x_{_P}F_2^{D(3)}$ rises as $\beta \rightarrow 0$, the rise accelerating with increasing Q^2 . These positive scaling violations suggest substantial contributions of perturbative effects in the diffractive DIS cross section.

The ZEUS Collaboration

S. Chekanov, M. Derrick, S. Magill, S. Miglioranzi¹, B. Musgrave, J. Repond, R. Yoshida
Argonne National Laboratory, Argonne, Illinois 60439-4815, USA ⁿ

M.C.K. Mattingly

Andrews University, Berrien Springs, Michigan 49104-0380, USA

N. Pavel, A.G. Yagües Molina

Institut für Physik der Humboldt-Universität zu Berlin, Berlin, Germany

P. Antonioli, G. Bari, M. Basile, L. Bellagamba, D. Boscherini, A. Bruni, G. Bruni, G. Cara Romeo, L. Cifarelli, F. Cindolo, A. Contin, M. Corradi, S. De Pasquale, P. Giusti, G. Iacobucci, A. Margotti, A. Montanari, R. Nania, F. Palmonari, A. Pesci, A. Polini, L. Rinaldi, G. Sartorelli, A. Zichichi

University and INFN Bologna, Bologna, Italy ^e

G. Aghuzumtsyan, D. Bartsch, I. Brock, S. Goers, H. Hartmann, E. Hilger, P. Irrgang, H.-P. Jakob, O. Kind, U. Meyer, E. Paul², J. Rautenberg, R. Renner, K.C. Voss³, M. Wang, M. Wlasenko

Physikalisches Institut der Universität Bonn, Bonn, Germany ^b

D.S. Bailey⁴, N.H. Brook, J.E. Cole, G.P. Heath, T. Namsoo, S. Robins

H.H. Wills Physics Laboratory, University of Bristol, Bristol, United Kingdom ^m

M. Capua, A. Mastroberardino, M. Schioppa, G. Susinno, E. Tassi

Calabria University, Physics Department and INFN, Cosenza, Italy ^e

J.Y. Kim, K.J. Ma

Chonnam National University, Kwangju, South Korea ^g

M. Helbich, Y. Ning, Z. Ren, W.B. Schmidke, F. Sciulli

Nevis Laboratories, Columbia University, Irvington on Hudson, New York 10027 ^o

J. Chwastowski, A. Eskreys, J. Figiel, A. Galas, K. Olkiewicz, P. Stopa, D. Szuba, L. Zawiejski

Institute of Nuclear Physics, Cracow, Poland ⁱ

L. Adamczyk, T. Bołd, I. Grabowska-Bołd, D. Kisielewska, A.M. Kowal, J. Łukasik, M. Przybycień, L. Suszycki, J. Szuba⁵

Faculty of Physics and Applied Computer Science, AGH-University of Science and Technology, Cracow, Poland ^p

A. Kotański⁶, W. Słomiński

Department of Physics, Jagellonian University, Cracow, Poland

V. Adler, U. Behrens, I. Bloch, K. Borras, D.G. Cassel⁷, G. Drews, J. Fourletova, A. Geiser, D. Gladkov, F. Goebel⁸, P. Göttlicher⁹, R. Graciani Diaz¹⁰, O. Gutsche, T. Haas, W. Hain, C. Horn, B. Kahle, M. Kasemann¹¹, U. Kötz, H. Kowalski, G. Kramberger, D. Lelas¹², H. Lim, B. Löhr, R. Mankel, M. Martinez¹³, I.-A. Melzer-Pellmann, C.N. Nguyen, D. Notz, A.E. Nuncio-Quiroz, A. Raval, R. Santamarta, U. Schneekloth, U. Stösslein, G. Wolf, C. Youngman, W. Zeuner

Deutsches Elektronen-Synchrotron DESY, Hamburg, Germany

S. Schlenstedt

Deutsches Elektronen-Synchrotron DESY, Zeuthen, Germany

G. Barbagli, E. Gallo, C. Genta, P. G. Pelfer

University and INFN, Florence, Italy ^e

A. Bamberger, A. Benen, F. Karstens, D. Dobur, N.N. Vlasov¹⁴

Fakultät für Physik der Universität Freiburg i.Br., Freiburg i.Br., Germany ^b

P.J. Bussey, A.T. Doyle, J. Ferrando, J. Hamilton, S. Hanlon, D.H. Saxon, I.O. Skillicorn
Department of Physics and Astronomy, University of Glasgow, Glasgow, United Kingdom ^m

I. Gialas¹⁵

Department of Engineering in Management and Finance, Univ. of Aegean, Greece

T. Carli, T. Gosau, U. Holm, N. Krumnack¹⁶, E. Lohrmann, M. Milite, H. Salehi, P. Schleper, T. Schörner-Sadenius, S. Stonjek¹⁷, K. Wichmann, K. Wick, A. Ziegler, Ar. Ziegler

Hamburg University, Institute of Exp. Physics, Hamburg, Germany ^b

C. Collins-Tooth¹⁸, C. Foudas, C. Fry, R. Gonçalo¹⁹, K.R. Long, A.D. Tapper

Imperial College London, High Energy Nuclear Physics Group, London, United Kingdom ^m

M. Kataoka²⁰, K. Nagano, K. Tokushuku²¹, S. Yamada, Y. Yamazaki

Institute of Particle and Nuclear Studies, KEK, Tsukuba, Japan ^f

A.N. Barakbaev, E.G. Boos, N.S. Pokrovskiy, B.O. Zhautykov

Institute of Physics and Technology of Ministry of Education and Science of Kazakhstan, Almaty, Kazakhstan

D. Son

Kyungpook National University, Center for High Energy Physics, Daegu, South Korea ^g

J. de Favereau, K. Piotrzkowski

Institut de Physique Nucléaire, Université Catholique de Louvain, Louvain-la-Neuve, Belgium ^q

F. Barreiro, C. Glasman²², O. González, M. Jimenez, L. Labarga, J. del Peso, J. Terrón, M. Zambrana

Departamento de Física Teórica, Universidad Autónoma de Madrid, Madrid, Spain ^l

M. Barbi, F. Corriveau, C. Liu, S. Padhi, M. Plamondon, D.G. Stairs, R. Walsh, C. Zhou
Department of Physics, McGill University, Montréal, Québec, Canada H3A 2T8 ^a

T. Tsurugai

Meiji Gakuin University, Faculty of General Education, Yokohama, Japan ^f

A. Antonov, P. Danilov, B.A. Dolgoshein, V. Sosnovtsev, A. Stifutkin, S. Suchkov
Moscow Engineering Physics Institute, Moscow, Russia ^j

R.K. Dementiev, P.F. Ermolov, L.K. Gladilin, I.I. Katkov, L.A. Khein, I.A. Korzhavina, V.A. Kuzmin, B.B. Levchenko, O.Yu. Lukina, A.S. Proskuryakov, L.M. Shcheglova, D.S. Zotkin, S.A. Zotkin

Moscow State University, Institute of Nuclear Physics, Moscow, Russia ^k

I. Abt, C. Büttner, A. Caldwell, X. Liu, J. Sutiak

Max-Planck-Institut für Physik, München, Germany

N. Coppola, G. Grigorescu, S. Grijpink, A. Keramidas, E. Koffeman, P. Kooijman, E. Maddox, A. Pellegrino, S. Schagen, H. Tiecke, M. Vázquez, L. Wiggers, E. de Wolf
NIKHEF and University of Amsterdam, Amsterdam, Netherlands ^h

N. Brümmer, B. Bylsma, L.S. Durkin, T.Y. Ling

Physics Department, Ohio State University, Columbus, Ohio 43210 ⁿ

P.D. Allfrey, M.A. Bell, A.M. Cooper-Sarkar, A. Cottrell, R.C.E. Devenish, B. Foster, G. Grzelak, C. Gwenlan²³, T. Kohno, S. Patel, P.B. Straub, R. Walczak

Department of Physics, University of Oxford, Oxford United Kingdom ^m

P. Bellan, A. Bertolin, R. Brugnera, R. Carlin, R. Ciesielski, F. Dal Corso, S. Dusini, A. Garfagnini, S. Limentani, A. Longhin, L. Stanco, M. Turcato

Dipartimento di Fisica dell' Università and INFN, Padova, Italy ^e

E.A. Heaphy, F. Metlica, B.Y. Oh, J.J. Whitmore²⁴

Department of Physics, Pennsylvania State University, University Park, Pennsylvania 16802 ^o

Y. Iga

Polytechnic University, Sagamihara, Japan ^f

G. D'Agostini, G. Marini, A. Nigro

Dipartimento di Fisica, Università 'La Sapienza' and INFN, Rome, Italy ^e

J.C. Hart

Rutherford Appleton Laboratory, Chilton, Didcot, Oxon, United Kingdom ^m

H. Abramowicz²⁵, A. Gabareen, M. Groys, S. Kananov, A. Kreisel, A. Levy

Raymond and Beverly Sackler Faculty of Exact Sciences, School of Physics, Tel-Aviv University, Tel-Aviv, Israel ^d

M. Kuze

Department of Physics, Tokyo Institute of Technology, Tokyo, Japan ^f

S. Kagawa, T. Tawara

Department of Physics, University of Tokyo, Tokyo, Japan ^f

R. Hamatsu, H. Kaji, S. Kitamura²⁶, K. Matsuzawa, O. Ota, Y.D. Ri

Tokyo Metropolitan University, Department of Physics, Tokyo, Japan ^f

M. Costa, M.I. Ferrero, V. Monaco, R. Sacchi, A. Solano

Università di Torino and INFN, Torino, Italy ^e

M. Arneodo, M. Ruspa

Università del Piemonte Orientale, Novara, and INFN, Torino, Italy ^e

S. Fourletov, T. Koop, J.F. Martin, A. Mirea

Department of Physics, University of Toronto, Toronto, Ontario, Canada M5S 1A7 ^a

J.M. Butterworth²⁷, R. Hall-Wilton, T.W. Jones, J.H. Loizides²⁸, M.R. Sutton⁴, C. Targett-Adams, M. Wing

Physics and Astronomy Department, University College London, London, United Kingdom ^m

J. Ciborowski²⁹, P. Kulinski, P. Łužniak³⁰, J. Malka³⁰, R.J. Nowak, J.M. Pawlak, J. Sztuk³¹,

T. Tymieniecka, A. Tyszkiewicz³⁰, A. Ukleja, J. Ukleja³², A.F. Żarnecki

Warsaw University, Institute of Experimental Physics, Warsaw, Poland

M. Adamus, P. Plucinski

Institute for Nuclear Studies, Warsaw, Poland

Y. Eisenberg, D. Hochman, U. Karshon, M.S. Lightwood

Department of Particle Physics, Weizmann Institute, Rehovot, Israel ^c

A. Everett, D. Kçira, S. Lammers, L. Li, D.D. Reeder, M. Rosin, P. Ryan, A.A. Savin, W.H. Smith

Department of Physics, University of Wisconsin, Madison, Wisconsin 53706, USA ⁿ

S. Dhawan

Department of Physics, Yale University, New Haven, Connecticut 06520-8121, USA ⁿ

S. Bhadra, C.D. Catterall, Y. Cui, G. Hartner, S. Menary, U. Noor, M. Soares, J. Standage,
J. Whyte

Department of Physics, York University, Ontario, Canada M3J 1P3 ^a

¹ also affiliated with University College London, UK

² retired

³ now at the University of Victoria, British Columbia, Canada

⁴ PPARC Advanced fellow

⁵ partly supported by Polish Ministry of Scientific Research and Information Technology, grant no.2P03B 12625

⁶ supported by the Polish State Committee for Scientific Research, grant no. 2 P03B 09322

⁷ on leave of absence from Cornell University, Ithaca, NY, USA

⁸ now at Max-Planck-Institut für Physik, München, Germany

⁹ now at DESY group FEB, Hamburg, Germany

¹⁰ now at Dept. Estructura; Constituentes de la Materia, Faculta de Fisica, Universitat de Barcelona, Spain

¹¹ now at DESY group FLC, Hamburg, Germany

¹² now at LAL, Université de Paris-Sud, IN2P3-CNRS, Orsay, France

¹³ now at Institut de Fisica d'Altes Energias (IFAE), Universitat de Barcelona, Spain

¹⁴ partly supported by Moscow State University, Russia

¹⁵ also affiliated with DESY

¹⁶ now at Baylor University, USA

¹⁷ now at University of Oxford, UK

¹⁸ now at the Department of Physics and Astronomy, University of Glasgow, UK

¹⁹ now at Royal Holloway University of London, UK

²⁰ also at Nara Women's University, Nara, Japan

²¹ also at University of Tokyo, Japan

²² Ramón y Cajal Fellow

²³ PPARC Postdoctoral Research Fellow

²⁴ on leave of absence at The National Science Foundation, Arlington, VA, USA

²⁵ also at Max Planck Institute, Munich, Germany, Alexander von Humboldt Research Award

²⁶ present address: Tokyo Metropolitan University of Health Sciences, Tokyo 116-8551, Japan

²⁷ also at University of Hamburg, Germany, Alexander von Humboldt Fellow

²⁸ partially funded by DESY

²⁹ also at Łódź University, Poland

³⁰ Łódź University, Poland

³¹ Łódź University, Poland, supported by the KBN grant 2P03B12925

³² supported by the KBN grant 2P03B12725

- ^a supported by the Natural Sciences and Engineering Research Council of Canada (NSERC)
- ^b supported by the German Federal Ministry for Education and Research (BMBF), under contract numbers HZ1GUA 2, HZ1GUB 0, HZ1PDA 5, HZ1VFA 5
- ^c supported in part by the MINERVA Gesellschaft für Forschung GmbH, the Israel Science Foundation (grant no. 293/02-11.2), the U.S.-Israel Binational Science Foundation and the Benoziyo Center for High Energy Physics
- ^d supported by the German-Israeli Foundation and the Israel Science Foundation
- ^e supported by the Italian National Institute for Nuclear Physics (INFN)
- ^f supported by the Japanese Ministry of Education, Culture, Sports, Science and Technology (MEXT) and its grants for Scientific Research
- ^g supported by the Korean Ministry of Education and Korea Science and Engineering Foundation
- ^h supported by the Netherlands Foundation for Research on Matter (FOM)
- ⁱ supported by the Polish State Committee for Scientific Research, grant no. 620/E-77/SPB/DESY/P-03/DZ 117/2003-2005 and grant no. 1P03B07427/2004-2006
- ^j partially supported by the German Federal Ministry for Education and Research (BMBF)
- ^k supported by RF Presidential grant N 1685.2003.2 for the leading scientific schools and by the Russian Ministry of Education and Science through its grant for Scientific Research on High Energy Physics
- ^l supported by the Spanish Ministry of Education and Science through funds provided by CICYT
- ^m supported by the Particle Physics and Astronomy Research Council, UK
- ⁿ supported by the US Department of Energy
- ^o supported by the US National Science Foundation
- ^p supported by the Polish Ministry of Scientific Research and Information Technology, grant no. 112/E-356/SPUB/DESY/P-03/DZ 116/2003-2005 and 1 P03B 065 27
- ^q supported by FNRS and its associated funds (IISN and FRIA) and by an Inter-University Attraction Poles Programme subsidised by the Belgian Federal Science Policy Office

1 Introduction

Inclusive deep inelastic lepton-nucleon scattering (DIS) has been measured over a wide kinematic range. This has allowed a precise description of the nucleon structure functions obtained through QCD analyses using the DGLAP evolution equations [1, 2]. It has been established at HERA, that diffraction, where the proton or a low-mass nucleonic system emerge from the interaction with almost the full energy of the incident proton, contributes substantially to the DIS cross section [3]. Extensive measurements of diffractive DIS have been made by both the ZEUS and H1 collaborations [4–7].

The diffractive component of DIS is analysed in terms of conditional parton distribution functions (PDFs) [4, 7]. According to the QCD factorisation theorem [8, 9], these diffractive PDFs will also undergo QCD evolution as a function of the photon virtuality Q^2 in the same way as the inclusive proton PDFs. The dipole model [10–13] provides an appealing picture that can be applied in DIS to both inclusive and diffractive scattering. In this model, the virtual photon dissociates into $q\bar{q}$ and $q\bar{q}g$ dipoles which then interact with the proton target, predominantly through gluon exchange. The size of the dipole is given by Q^2 and, in the kinematic range of HERA, varies from a typical hadron size down to much smaller values.

For hadron-hadron collisions, a large body of data on total, elastic and diffractive cross sections [14] has been parameterised in Regge phenomenology by the exchange of the Pomeron trajectory. An early seminal suggestion to combine Regge phenomenology with QCD [15] in a t -channel picture introduced the idea of a Pomeron structure function. Assuming that diffraction can be described by the exchange of the Pomeron, its partonic structure can be determined in diffractive DIS. Such an approach depends on the validity of Regge factorisation, which implies a Pomeron flux that is independent of Q^2 .

For scattering of on-shell particles, such as $\gamma p \rightarrow \gamma p$, the optical theorem relates the imaginary part of the forward elastic amplitude to the total γp cross section. Similarly, diffractive scattering of *virtual* photons leading to a low-mass hadronic system should also be closely related to the total virtual photon-proton cross section.

This paper reports high statistics results from the ZEUS experiment on e^-p deep inelastic scattering (Fig. 1),

$$ep \rightarrow e + \text{anything},$$

with the focus on diffractive production by virtual photon-proton scattering (Fig. 2),

$$\gamma^* p \rightarrow XN,$$

(where N is a proton or a low-mass nucleonic state) and a comparison with the total $\gamma^* p$ cross section.

In comparison to previous ZEUS measurements of diffraction [5], the detector configuration was improved in the following way. The installation of a forward plug calorimeter (FPC) in the beam hole of the forward uranium calorimeter extended the forward rapidity coverage. As a result, the measurable range in the mass of the system X was increased by a factor of 1.7. At the same time, the contribution of nucleon dissociation was limited to masses $M_N \leq 2.3$ GeV. The rear beam hole in the detector was decreased in size by moving the calorimeter modules above and below closer to the beams. This increased the acceptance for low Q^2 and large W events. These measures substantially improved the precision and kinematic coverage in comparison to previous HERA measurements [4–6].

This paper is organized as follows. The experimental setup is described in Section 2. Reconstruction of event kinematics and event selection are described in Section 3. Models for inclusive and diffractive DIS are presented in Section 4. Extraction of the diffractive contribution is discussed in Section 5. Evaluation of the total and diffractive cross sections is described in Section 6. Section 7 presents the results on the proton structure function and the total γ^*p cross section. The diffractive cross section is presented in terms of M_X , W and Q^2 , and compared to the total cross section in Section 8. The diffractive structure function of the proton is discussed in Section 9.

2 Experimental set-up

The data used for this measurement were taken at the HERA ep collider using the ZEUS detector in 1998–1999 when electrons of 27.5 GeV collided with protons of 920 GeV. The data correspond to an integrated luminosity of 4.2 pb^{-1} .

A detailed description of the ZEUS detector can be found elsewhere [16, 17]. A brief outline of the components that are most relevant for this analysis is given below.

Deep inelastic scattering events were identified using information from the uranium-scintillator calorimeter (CAL), the forward plug calorimeter (FPC), the central tracking detector (CTD), the small angle rear tracking detector (SRTD) and the rear part of the hadron-electron separator (RHES).

Charged particles are tracked in the CTD [18]. The CTD consists of 72 cylindrical drift chamber layers, organized in nine superlayers covering the polar-angle¹ region $15^\circ < \theta < 164^\circ$. The CTD operates in a magnetic field of 1.43 T provided by a thin solenoid. The

¹ The ZEUS coordinate system is a right-handed Cartesian system, with the Z axis pointing in the proton direction, referred to as the “forward direction”, and the X axis pointing left towards the centre of HERA. The coordinate origin is at the nominal interaction point.

transverse-momentum resolution for full-length tracks is $\sigma(p_T)/p_T = 0.0058p_T \oplus 0.0065 \oplus 0.0014/p_T$, with p_T in GeV.

The CAL [19] consists of three parts: the forward (FCAL), the barrel (BCAL) and the rear (RCAL) calorimeters. Each part is subdivided transversely into towers and longitudinally into one electromagnetic section (EMC) and either one (in RCAL) or two (in BCAL and FCAL) hadronic sections (HAC). The smallest subdivision of the calorimeter is called a cell. The CAL energy resolutions, as measured under test-beam conditions, are $\sigma(E)/E = 0.18/\sqrt{E}$ for electrons and $\sigma(E)/E = 0.35/\sqrt{E}$ for hadrons (E in GeV). The CAL covers 99.7% of the total solid angle. The beam hole in the RCAL was $20 \times 8 \text{ cm}^2$ [20].

The position of electrons scattered at small angles to the electron-beam direction was determined including the information from the SRTD [20, 21]. The SRTD is attached to the front face of the RCAL and consists of two planes of scintillator strips, 1 cm wide and 0.5 cm thick, arranged in orthogonal orientations. Ambiguities in SRTD hits were resolved with the help of the RHES [22], which consists of a layer of approximately 10,000 ($2.96 \times 3.32 \text{ cm}^2$) silicon-pad detectors inserted in the RCAL at a depth of 3.3 radiation lengths. Electrons scattered at higher Q^2 were also measured in the CTD.

The FPC [23] was used to measure the energy of particles in the pseudorapidity range $\eta \approx 4.0 - 5.0$. It was a lead-scintillator sandwich calorimeter read out by wavelength-shifter (WLS) fibers and photomultipliers (PMT). It was installed in the $20 \times 20 \text{ cm}^2$ beam hole of FCAL. The FPC had outer dimensions of $192 \times 192 \times 1080 \text{ mm}^3$ and a hole of 3.15 cm radius for the passage of the beams. The minimum angle for particle detection was 12 mrad which corresponds to a pseudorapidity of 5.1. In the FPC, 15 mm-thick lead plates alternated with 2.6-mm thick scintillator layers. The WLS fibers of 1.2 mm diameter passed through 1.4 mm holes located on a 12 mm grid in the lead and scintillator layers. The FPC was subdivided longitudinally into an electromagnetic (10 layers) and a hadronic section (50 layers) representing a total of 5.4 nuclear absorption lengths. The scintillator layers consisted of tiles forming towers which are read out individually. The cell cross sections were $24 \times 24 \text{ mm}^2$ in the electromagnetic and $48 \times 48 \text{ mm}^2$ in the hadronic section. The FPC was tested and calibrated at CERN with electron, muon and hadron beams. The measured energy resolution for electrons was $\sigma_E/E = (0.41 \pm 0.02)/\sqrt{E} \oplus 0.062 \pm 0.002$, (E in GeV). When installed in the FCAL, the energy resolution for pions was $\sigma_E/E = (0.65 \pm 0.02)/\sqrt{E} \oplus 0.06 \pm 0.01$ (E in GeV) and the e/h ratio was close to unity. The relative calibration of the FPC cells was regularly adjusted using measurements from a ^{60}Co source, resulting in an average energy scale uncertainty of 4% (3%) for the EMC

(HAC) cells [24] as determined with DIS events at high Q^2 ².

3 Reconstruction of kinematics and event selection

This section describes event reconstruction and selection common to DIS inclusive and diffractive data samples.

The reaction $e^-(k) p(P) \rightarrow e^-(k') + \text{anything}$ at fixed squared centre-of-mass (c.m.) energy, $s = (k + P)^2$, is described in terms of $Q^2 \equiv -q^2 = -(k - k')^2$, Bjorken $x = Q^2/(2P \cdot q)$ and $s \approx 4E_e E_p$, where E_e and E_p denote the electron and proton beam energies, respectively. For this data set, $\sqrt{s} = 318$ GeV. The fractional energy transferred to the proton in its rest system is $y \approx Q^2/(sx)$. The c.m. energy of the total hadronic system, W , is given by $W^2 = [p + (k - k')]^2 = m_p^2 + Q^2(1/x - 1) \approx Q^2/x = ys$, where m_p is the mass of the proton.

Diffraction, $e^-(k) p(P) \rightarrow e^-(k') + N(N) + X$, is described in terms of the mass M_X of the system X , and the mass M_N of the system N . Since t , the four-momentum transfer squared, between the incoming proton and the outgoing system N , $t = (p - N)^2$, was not measured, the results presented are integrated over t .

The diffractive structure function was analyzed in terms of the momentum fraction of the proton carried by the Pomeron, $x_{_P} = [(P - N) \cdot q]/(P \cdot q) \approx (M_X^2 + Q^2)/(W^2 + Q^2)$, and the fraction of the Pomeron momentum carried by the struck quark, $\beta = Q^2/[2(P - N) \cdot q] \approx Q^2/(M_X^2 + Q^2)$. The variables $x_{_P}$ and β are related to the Bjorken scaling variable, x , via $x = \beta x_{_P}$.

The events studied are of the type

$$ep \rightarrow e' \mathcal{X} + \text{rest}, \quad (1)$$

where \mathcal{X} denotes the hadronic system observed in the detector and ‘rest’ the particle system escaping detection through the forward and/or rear beam holes.

Scattered electrons were identified with an algorithm based on a neural network [25]. The direction and energy of the scattered electron were determined from the combined information given by CAL, SRTD, RHES and CTD. The impact point of the electron on the face of the RCAL had to lie outside an area of 26.6 cm \times 17 cm (box cut) centred on

² Throughout the running period, DIS neutral current events, $ep \rightarrow eX$, with $Q^2 > 80$ GeV², were selected without using information from the FPC. The average energy deposited by the hadronic system in the individual FPC cells was used to monitor the energy calibration of each cell during the data-taking period.

the beam axis. Further fiducial cuts on the impact point were imposed to ensure reliable measurement of the electron energy.

The value of Q^2 was reconstructed from the measured energy E'_e and scattering angle θ_e , of the electron, $Q^2 = 2E_e E'_e (1 + \cos \theta_e)$. The hadronic system was reconstructed from energy-flow objects (EFO) [24, 26] which combine the information from CAL and FPC clusters and from CTD tracks, and which were not assigned to the scattered electron (hadronic EFOs).

The value of W was determined using the weighted average of the values given by the electron and the hadron measurements (see Appendix A).

The mass of the system \mathcal{X} was determined by summing over all hadronic EFOs,

$$M_{\mathcal{X}}^2 = (\sum P_h)^2,$$

where P_h is the four-momentum vector of each EFO h . All kinematic variables used to describe inclusive and diffractive scattering were derived from $M_{\mathcal{X}}$, W and Q^2 .

The coordinates X_{vtx} , Y_{vtx} , Z_{vtx} of the event vertex were determined with tracks reconstructed in the CTD. The average X_{vtx} , Y_{vtx} values varied by ± 0.1 cm and ± 0.03 cm, respectively, over the data-taking period. Since the variations were small, and the transverse size of the beams were smaller than the resolution, the average X_{vtx} , Y_{vtx} values were used. The distribution of Z_{vtx} was approximately Gaussian with an r.m.s. of ± 11 cm. The value of Z_{vtx} was taken from the reconstructed event vertex. For events without a measured primary vertex, the average Z vertex for each data run was used.

If a scattered-electron candidate was found, the following criteria were imposed to select the DIS events:

- the scattered-electron energy E'_e be at least 10 GeV;
- the total measured energy of the hadronic system be at least 400 MeV;
- $y_{\text{JB}}^{\text{FB}} > 0.004$, where $y_{\text{JB}}^{\text{FB}} = \sum_h (E_h - P_{Zh}) / (2E_e)$, summed over all hadronic EFOs in FCAL plus BCAL; or at least 400 MeV be deposited in the BCAL or in the RCAL outside of the ring of towers closest to the beamline;
- $-54 < Z_{\text{vtx}} < 50$ cm;
- $46 < \sum_{i=e,h} (E_i - P_{Zi}) < 64$ GeV, where the sum runs over both the scattered electron and all hadronic EFOs. This cut reduces the background from photoproduction and beam-gas scattering and removes events with large initial-state QED radiation;
- candidates for QED-Compton events, consisting of a scattered electron candidate and a photon candidate with mass $M_{e\gamma}$ less than 0.25 GeV and total transverse momentum less than ≈ 1.5 GeV, were removed.

The contamination from electron (proton) beam-gas scattering was measured using non-colliding electron (proton) bunches and found to be negligible.

About 800,000 events passed the selection cuts. The kinematic range for inclusive and diffractive events was chosen taking into account detector resolution and statistics. About 612,000 events were retained which satisfied $37 < W < 245$ GeV and $2.2 < Q^2 < 80$ GeV 2 .

The resolutions of the reconstructed kinematic variables were estimated using Monte Carlo (MC) simulation of diffractive events of the type $\gamma^*p \rightarrow XN$ (see Section 4). For the M_X , W and Q^2 bins considered in this analysis, the resolutions are approximately $\frac{\sigma(W)}{W} = \frac{1}{W^{1/2}}$, $\frac{\sigma(Q^2)}{Q^2} = \frac{0.25}{(Q^2)^{1/3}}$ and $\frac{\sigma(M_X)}{M_X} = \frac{c}{M_X^{1/3}}$, where $c = 0.6$ GeV $^{1/3}$ for $M_X < 1$ GeV and $c = 0.4$ GeV $^{1/3}$ for $M_X \geq 1$ GeV, with M_X, W in units of GeV and Q^2 in GeV 2 .

Results are presented for seven bins in W , seven bins in Q^2 and six bins in M_X , as shown in Table 1. The QED-Born-level cross sections and structure functions are determined as averages over these intervals and transported (see Section 6) to the reference values $(M_{X\text{ ref}}, W_{\text{ref}}, Q_{\text{ref}}^2)$ listed in Table 1.

4 Monte Carlo simulations

The data were corrected for detector acceptance and resolution with suitable combinations of several MC models. Events from inclusive DIS, including radiative effects, were simulated using the HERACLES 4.6.1 [27] program with the DJANGOH 1.1 [28] interface to the hadronisation programs and using the CTEQ4D next-to-leading-order PDFs [29]. In order to improve the description of the existing measurements at $Q^2 < 2$ GeV 2 , a parametrisation [30] of the measured F_2 data was used to reweight the generated non-diffractive events. In HERACLES, $O(\alpha)$ electroweak corrections are included. The colour-dipole model of ARIADNE 4 [31], including boson-gluon fusion, was used to simulate the $O(\alpha_S)$ plus leading-logarithmic corrections to the quark-parton model. The Lund string model as implemented in JETSET 7.4 [32] was used by ARIADNE for hadronisation.

Diffractive DIS in which the proton does not dissociate, $ep \rightarrow eXp$ (including the production of ω and ϕ mesons via $ep \rightarrow eV^0p$, $V = \omega, \phi$ but excluding ρ^0 production), were simulated with SATRAP which is based on a saturation model [12] and is interfaced to the RAPGAP 2.08 framework [33]. The QED radiative effects were simulated with HERACLES. The QCD parton showers were simulated with LEPTO 6.5 [34]. The production of ρ^0 mesons, $ep \rightarrow e\rho^0p$, was simulated with JETSET 7.4 interfaced to the module ZEUSVM [35] which uses a parametrisation of the measured ρ^0 cross sections as well as of the production and decay angular distributions [36, 37].

The diffractive process in which the proton dissociates, $ep \rightarrow eXN$, was simulated with SATRAP interfaced to a module called SANG [38]. SANG includes the production of ρ^0 mesons. The mass spectrum of the system N was generated according to $d\sigma/dM_N^2 \propto (1/M_N^2)^n$ with $n = 1$. The fragmentation of the system N was simulated using JETSET 7.4. The reweighting procedure used to match the generated M_N spectrum with that of the data is described in Section 5.2.

All DIS processes except for those simulated by ZEUSVM were generated starting at $Q^2 = 0.5$ GeV 2 ; events from ZEUSVM were generated starting at $Q^2 = 0.7$ GeV 2 , since the contribution from lower values of Q^2 was negligible. Since the diffractive events in data and MC showed different W and β dependences, events generated by SATRAP, which were the bulk of MC diffractive events, were reweighted to match the data.

In order to test for a possible contribution from Reggeon exchange to the final state reaction $\gamma^*p \rightarrow XN$, events were generated with RAPGAP in accordance with the analysis of the Regge contribution given in Appendix C. The background from photoproduction was estimated with events generated by PYTHIA 5.7 [32].

The ZEUS detector response was simulated using a program based on GEANT 3.13 [39]. The generated events were passed through the detector and trigger simulation and processed by the same reconstruction and analysis programs as the data. The Z_{vtx} distribution used in the MC was reweighted to agree with the data.

The simulation of the measured total hadronic energy was checked with the balance of the measured transverse momenta of the scattered electron and that of the observed total hadronic system. For both MC and data, an average transverse momentum balance was achieved by increasing the measured hadronic energies by a factor of 1.065. The mass M_{χ} reconstructed from the energy-corrected EFOs, in the M_{χ} region analyzed, required an additional correction factor of 1.10 which was determined from MC simulation ³.

Good agreement between data and simulated event distributions was obtained for both the inclusive and diffractive samples. More details on the event simulation can be found elsewhere [24, 38].

³ The hadrons produced in diffractive events, on average, have lower momenta than those for hadrons from non-peripheral events, and their fractional energy loss in the material in front of the calorimeter is larger.

5 Determination of the diffractive contribution

5.1 The M_X method

The diffractive contribution was extracted from the data using the M_X method [5, 40].

The virtual photon-proton collision can be described as (see Eq. (1)) $\gamma^* p \rightarrow \mathcal{X} + \text{rest}$, where \mathcal{X} represents all particles measured in the detector and ‘rest’ all particles that escape through the beam holes. In the QCD picture of non-peripheral DIS, \mathcal{X} is related to the struck quark and ‘rest’ to the proton remnant, both of which are coloured states. The final-state particles are expected to be uniformly emitted in rapidity along the $\gamma^* p$ collision axis leading to final-state particles which populate uniformly the rapidity gap between the struck quark and the proton remnant [41]. In this case, it can be shown from general arguments (see Appendix B) that the mass, $M_{\mathcal{X}}$, is distributed as

$$\frac{d\mathcal{N}^{\text{non-diff}}}{d \ln M_{\mathcal{X}}^2} = c \cdot \exp(b \cdot \ln M_{\mathcal{X}}^2), \quad (2)$$

where b and c are constants. DJANGOH predicts, for non-peripheral DIS, $b \approx 1.9$.

The diffractive reaction, $\gamma^* p \rightarrow XN$, on the other hand, has different characteristics. The incoming proton undergoes a small perturbation and emerges either intact, or as a low-mass nucleonic state, carrying a large fraction, x_L , of the incoming proton momentum. Diffractive scattering shows up as a peak near $x_L = 1$, the mass of the system X being limited by kinematics to $M_X^2/W^2 \lesssim 1-x_L$. Moreover, the distance in rapidity between the outgoing nucleon system N and the system X is $\Delta\eta \approx \ln(1/(1-x_L))$ [42], becoming large when x_L is close to one. Combined with the limited values of M_X and the peaking of the diffractive cross section near $x_L = 1$, this leads to a large separation in rapidity between N and any other hadronic activity in the event. For the vast majority of diffractive events, the decay particles from the system N leave undetected through the forward beam hole. For a wide range of M_X values, the particles of the system X are emitted entirely within the acceptance of the detector and the measured system \mathcal{X} can be identified with X . Monte Carlo studies show that X can be reliably reconstructed over the full M_X range of this analysis: Fig. 3 shows the distribution of the measured versus the generated value of $\ln M_X^2$ for the lowest and highest W bins at two different Q^2 values. The horizontal bars indicate the maximum values of $\ln M_X^2$ up to which the diffractive contribution was extracted. There is a close correlation between the measured and the generated $\ln M_X^2$ value. From this point on, the distinction between \mathcal{X} and X will be omitted.

Regge phenomenology predicts the shape of the M_X distribution for peripheral processes (see Appendix B). Diffractive production by Pomeron exchange in the t -channel, which dominates x_L values close to unity, leads to an approximately constant $\ln M_X^2$ distribution

($b \approx 0$). Figure 4 shows the distribution of $\ln M_X^2$ for the lowest and highest W bins at low and high Q^2 for the data together with the expectations from MC simulation for non-peripheral DIS (DJANGOH) and for diffractive processes (SATRAP + ZEUSVM and SANG). The observed distributions agree well with the expectation for a non-diffractive component giving rise to an exponentially growing $\ln M_X^2$ distribution, and for a diffractive component producing an almost constant distribution in a large part of the $\ln M_X^2$ range.

The recent ZEUS measurement of diffraction in DIS with the leading proton spectrometer (LPS) [7] allows the Reggeon exchange contribution (Fig. 5) to be estimated, as discussed in Appendix C. Figure 6 compares, for the same (W, Q^2) bins as in Fig. 4, the $\ln M_X^2$ distributions for the data with those expected from Reggeon exchange. In this case, the $\ln M_X^2$ distribution increases exponentially with increasing $\ln M_X^2$ with a slope value of $b \approx 1.3$.

The exponential rise of the $\ln M_X^2$ distribution for non-diffractive processes permits the subtraction of this component and, therefore, the extraction of the diffractive contribution without assumptions about its exact M_X dependence. The distribution is of the form:

$$\frac{dN}{d \ln M_X^2} = D + c \cdot \exp(b \ln M_X^2), \quad \ln M_X^2 < \ln W^2 - \eta_0, \quad (3)$$

where D is the diffractive contribution and the second term represents the non-diffractive contributions. The quantity $(\ln W^2 - \eta_0)$ specifies the maximum value of $\ln M_X^2$ up to which the exponential behaviour of the non-diffractive contribution holds. A value of $\eta_0 = 2.2$ was found from the data. Equation (3) was fitted to the data in the limited range $\ln W^2 - 5.6 < \ln M_X^2 < \ln W^2 - \eta_0$ in order to determine the parameters b and c . The diffractive contribution is expected to be a slowly varying function of $\ln M_X^2$ when $M_X^2 > Q^2$, and to approach, for large M_X^2 , an approximately constant $\ln M_X^2$ distribution [11, 43, 44]. Therefore, D was assumed to be constant over the fit range. However, the diffractive contribution was not taken from the fit but was obtained from the observed number of events after subtracting the non-diffractive contribution determined using the fitted values of b and c .

The non-diffractive contribution in the (M_X, W, Q^2) bins was measured in two steps. In the first step, the slope b was determined as an average of the values obtained from the fits to the data for the intervals with $134 < W < 245$ GeV and $2.2 < Q^2 < 10$ GeV 2 . The fits yielded $b_{\text{nom}} = 1.63 \pm 0.07$. In the second step, the fits were repeated for all (W, Q^2) intervals, using $b = b_{\text{nom}}$ as a fixed parameter and assuming D to be constant. Good fits with χ^2 per degree of freedom (dof) of about unity were obtained. The statistical error of the diffractive contribution includes the uncertainty of b_{nom} .

Figures 4 and 6 show the results from the fit according to Eq. (3) for the non-diffractive and the sum of the non-diffractive and diffractive contributions. Figure 6 shows the M_X

distribution of the RAPGAP Reggeon simulation described in Section 4. As discussed above, the Reggeon contribution to the M_X spectra is similar in slope to the non-peripheral contribution described by Eq. (2), and is always smaller than the nondiffractive contributions ⁴. The same conclusions hold for all other (W, Q^2) bins considered in this analysis.

Finally, a MC event sample was prepared which consisted of the sum of the contributions from diffraction (SATRAP+ZEUSVM+SANG) and non-peripheral scattering (DJANGOH). The MC event sample was subjected to the same analysis procedure as the data and the diffractive contribution was extracted for all (M_X, W, Q^2) bins. For all bins, the accuracy of the determination of the fraction of diffractive events in the MC sample was better than the statistical precision of the data. The same test was repeated with the RAPGAP Reggeon sample included in the summed MC event sample. The normalisation of the Reggeon sample was increased by a factor of two - with respect to that found in the study of Appendix C - in order to test the robustness of the M_X -method extraction of the diffractive component against the large uncertainties of the Reggeon contribution. The result showed that the diffractive component was extracted with accuracy similar to that of the extraction without the Reggeon component.

For the final analysis of the diffractive cross section and structure function, only (M_X, W, Q^2) bins where the non-diffractive background was less than 50% were kept.

5.2 Contribution from diffractive proton dissociation

In addition to single dissociation, $\gamma^*p \rightarrow Xp$, processes where the proton also dissociates, $\gamma^*p \rightarrow XN$, can contribute to the diffractive event sample. Events from double dissociation can be grouped into those events where N has a low mass and disappears in the forward beam hole without energy deposition in the calorimeters FPC or CAL, and into those where decay particles deposit energy in the calorimeters. The probability of depositing energy in the calorimeters depends on the mass M_N . On average, in events where N has a mass below 2.3 GeV, the system N disappears in the forward beam hole without energy deposition in the FPC or the CAL, while for those events with $M_N > 2.3$ GeV, the system N deposits energy in the calorimeters. In the latter case, the reconstructed mass of the total hadronic system is larger than the mass of X . Such events lead to a distortion of the $\ln M_X^2$ distribution at high M_X values. In order to study this effect, double dissociative events were generated using SANG.

⁴ A recent determination of the diffractive contribution based on the presence of a leading proton [7] has been limited to the region $x_{IP} < 0.01$ to exclude contributions from Reggeon exchange. The fact that the M_X method excludes the Reggeon contribution allows the diffractive component to be extracted also in the region $x_{IP} > 0.01$.

The parameters of SANG, in particular those determining the shape of the M_N spectrum and the overall normalization, were checked with the subset of the data dominated by the contribution from double dissociation. Events in this subset were required to have a minimum rapidity gap $\Delta\eta > \eta_{\min}$ between at least one EFO and its neighbours. Good sensitivity for double dissociation was obtained with $\eta_{\min} = 3.0$ for $W = 55 - 99$ GeV and $\eta_{\min} = 4.0$ for $W = 99 - 245$ GeV. The study was performed with four event samples for the kinematic regions shown in Figs. 7 and 8.

The mass of the hadronic system reconstructed from the energy deposits in FPC+FCAL, M_{FFCAL} , depends approximately linearly on the mass M_N^{gen} of the generated system N . The distribution of M_{FFCAL} at low M_{FFCAL} is dominated by double dissociation. After reweighting the M_N distribution generated for the process $\gamma^*p \rightarrow XN$, good agreement was obtained between the number of events measured and the number of events predicted from the sum of the simulated Xp , ρ^0p , XN and non-diffractive processes.

Figure 7 demonstrates the sensitivity of the M_{FFCAL} distribution to the shape of the M_N -spectrum: it shows, for the four (Q^2, W) regions, the distribution of M_{FFCAL} as predicted by SANG, and after reweighting SANG for $M_N > M_{N0} = 2.3$ GeV by $(\frac{M_N}{M_{N0}})^{+1}$, or by $(\frac{M_N}{M_{N0}})^{-1}$. In the first case, the event rate increases (e.g. near $M_{\text{FFCAL}} = 1$ GeV by roughly a factor of two); in the second case, the event rate decreases (near $M_{\text{FFCAL}} = 1$ GeV by about a factor of 1.5). To achieve agreement with the data (see Fig. 8) SANG was reweighted for $M_N \leq 4$ GeV by a factor of $0.89\sqrt{M_N/4}$ (M_N in GeV), and for $M_N > 4$ GeV by a factor of $(2.5/M_N)^{0.25}$. In this exercise, the diffractive contribution for $M_N > 2.3$ GeV is assumed not to change with W . The good description of the data obtained from this simulation supports this assumption (see below).

The data distributions of M_{FFCAL} at low M_{FFCAL} and the reweighted MC predictions are compared in Fig. 8 for the four (Q^2, W) regions. The sum of the contributions calculated for Xp , ρ^0p and the non-diffractive component are shown, as well as the XN contribution which dominates the region of low M_{FFCAL} values. The sum of the four contributions reproduces the data well. Double dissociation, $(\gamma^*p \rightarrow XN)$, accounts for more than 80% of the events predicted by MC: for Fig. 8a when $M_{\text{FFCAL}} < 2.5$ GeV, for Fig. 8b when $M_{\text{FFCAL}} < 2$ GeV, for Fig. 8c when $M_{\text{FFCAL}} < 5$ GeV and for Fig. 8d when $M_{\text{FFCAL}} < 3$ GeV.

This study showed that, approximately, events generated with $M_N < 2.3$ GeV deposit less than 1 GeV of energy in the FPC, while events with $M_N \geq 2.3$ GeV deposit more than 1 GeV. No information could be gained from the data on the contribution from double dissociation with $M_N > 2.3$ GeV. Figure 9 shows the $\ln M_X^2$ spectra for the same W and Q^2 regions as in Fig. 4 together with the expected contribution from double dissociation, $\gamma^*p \rightarrow XN$, for those events with $M_N \geq 2.3$ GeV. This contribution is of the order of 6% (18%, 36%) for $M_X/W < 0.05$ ($M_X/W = 0.1, 0.14$). Since this contribution can affect the

determination of the slope b for the non-diffractive contribution, it has been subtracted, using the MC simulation, from the data as a function of M_X , W and Q^2 . The systematic error (see Section 6.1) allows for a 30% increase/decrease of the number of events removed. The diffractive cross section presented later is therefore the sum of the contributions from the Xp and XN ($M_N < 2.3$ GeV) final states.

Also shown in Fig. 9 is the expected contribution from photoproduction which is negligible, except at high W .

5.3 The $\ln M_X^2$ distributions

The $\ln M_X^2$ spectra for all (W, Q^2) bins studied in this analysis are displayed in Fig. 10. The data distributions, from which the contributions from double dissociation ($M_N < 2.3$ GeV) and from photoproduction background have been subtracted, are shown. They are compared with the MC predictions for the contributions from non-peripheral and diffractive production. It can be seen that the events at low and medium values of $\ln M_X^2$ originate exclusively from diffractive production. The MC simulations are in good agreement with the data.

6 Evaluation of cross sections and systematic uncertainties

The total and diffractive cross sections for ep scattering in a given (W, Q^2) bin were determined from the number of observed events, corrected for background, acceptance and smearing, and corrected to the QED Born level.

The cross sections and structure functions are presented at the reference values W_{ref} , Q_{ref}^2 , and $M_{X\text{ref}}$. This was achieved as follows: first, the cross sections and structure functions were determined at the weighted average of each (M_X, W, Q^2) bin. They were then transported to the reference position using a parametrisation [30] in the case of the proton structure function F_2 , and the result of the BEKW(mod) fit (see Section 9.3) for the diffractive cross sections and structure functions. The resulting changes to the cross section and structure function values from the average to those at the reference positions were 5 - 15%.

6.1 Systematic uncertainties

A study of the main sources contributing to the systematic uncertainties of the measurements were performed. The systematic uncertainties were calculated by varying the cuts or modifying the analysis procedure and repeating the full analysis for every variation. The size of the variations of cuts and the changes of the energy scales were chosen commensurate with the resolutions or the uncertainties of the relevant variables:

- the acceptance at low values of Q^2 depends critically on the position measurement of the scattered electron. The vertical separation of the upper and lower halves of the SRTD was increased (decreased) by 0.2 cm in the data (systematic uncertainties 1a,b) while their positions in the MC were left unchanged. The resulting deviations of the cross sections were typically 5 - 7 %;
- the box cut was changed from 26.6 cm \times 17 cm to 27.6 cm \times 18 cm (systematic uncertainty 2). This affected the low- Q^2 region. Changes of 5 - 15% were observed, mainly for $W < 100$ GeV;
- the measured energy of the scattered electron was increased (decreased) by 2% in the data, but not in the MC (systematic uncertainties 3a,b). In most cases the changes were smaller than, or of the order of, the statistical error;
- the lower cut for the energy of the scattered electron was lowered to 8 GeV (raised to 12 GeV) (systematic uncertainties 4a,b). This produced changes of 0 - 2%;
- to estimate the systematic uncertainties due to the uncertainty in the hadronic energy, the analysis was repeated after increasing (decreasing) the hadronic energy measured by the CAL by 2% in the data but not in MC (systematic uncertainties 5a,b). The typical changes were below 5%;
- the energies measured by the FPC were increased (decreased) by 10% in the data but not in MC (systematic uncertainties 6a,b). The effect was negligible;
- the minimum hadronic energy cut of 400 MeV was increased by 50% (systematic uncertainty 7). This led to changes at the 1-3% level;
- in order to check the simulation of the hadronic final state, the selection on $\sum_{i=e,h} (E_i - P_{Zi})$ was changed from (46 to 64) to (43 to 64) GeV (systematic uncertainty 8), leading to changes at the level of 20 to 30% of the statistical uncertainty except for one measurement at low Q^2 and high W . Also in this case, the change was small compared to the total systematic uncertainty;
- the reconstructed mass M_X of the system X was increased (decreased) by 5% in the data but not in the MC (systematic uncertainties 9a,b). Changes of the order of 5 -

10% were observed for the lowest M_X bin while, for the higher M_X bins, the changes were much smaller;

- a substantial fraction of events at $W > 164$ GeV, low M_X and low Q^2 have no measured primary vertex. The position of the vertex affects the measurement of the polar angle of the scattered electron and so of Q^2 . For these events, the average vertex for each data-taking run was used. The fraction of events with no vertex found in the data agrees well with the MC predictions ⁵. The difference between the observed fraction of events and that predicted by MC was used as a systematic uncertainty (systematic error 10) which amounted to 5 - 10% for low M_X and Q^2 , and to much smaller values elsewhere;
- the contribution from double dissociation with $M_N > 2.3$ GeV was determined with the help of the reweighted SANG simulation and was subtracted from the data. The diffractive cross section was redetermined by increasing (decreasing) the predicted contribution from SANG by 30% (systematic uncertainties 11a,b). The resulting changes in the diffractive cross section were well below the statistical uncertainty except for four data points, where they were of similar magnitude.

In order to evaluate the uncertainties arising from the form of the $\ln M_X^2$ distribution assumed for the diffractive contribution ($D = \text{constant}$, see Eq. (3)), the fits were repeated with the form $D = d_0(1 - \beta)[\beta(1 - \beta) + d_1(1 - \beta)^\kappa]$, where d_0, d_1, κ are fit parameters [11, 43–45]. Negligible changes were found.

The total systematic error for each bin was determined by adding the individual contributions in quadrature.

In the fits reported below, except for the BEKW(mod) fit, the fits were performed (a) to the nominal values, (b) to every data set (j) obtained by shifting the measured values by the amount given by the systematic uncertainty (j). The statistical uncertainties were included in each fit. The fit parameters quoted are those given by the fit to the nominal values; the systematic uncertainties were obtained as the square root of the sum of the squares of the differences between the fit parameters obtained with the nominal set and those obtained with the systematic shifts. In the case of conjugated uncertainties (labelled as (a,b) above) the averages of the squares of the two uncertainties were taken. For the BEKW(mod) fit, the statistical and systematic uncertainties of the measured values of the diffractive structure function were added in quadrature.

⁵ For four (M_X, W, Q^2) bins - all of which have $M_X = 1.2$ GeV and $W = 180$ or 220 GeV, the fraction of events in the data without a vertex is above 35%. The fraction of events predicted by the MC for these bins is the same to within 7%.

7 Proton structure function F_2 and the total γ^*p cross section

A prime goal of this analysis is the study of the W and Q^2 dependences of the diffractive cross section as a function of M_X , and the comparison with the *total* cross section. As a first step, the total cross section was determined for the same bins in W and Q^2 as for the diffractive cross section and using an identical analysis procedure. This minimises systematic uncertainties and allows the most direct comparison of the two cross sections.

The differential cross section for inclusive ep scattering mediated by virtual photon exchange is given in terms of the structure functions F_i of the proton by

$$\frac{d^2\sigma^{e^-p}}{dxdQ^2} = \frac{2\pi\alpha^2}{xQ^4} [YF_2(x, Q^2) - y^2F_L(x, Q^2)](1 + \delta_r(x, Q^2)), \quad (4)$$

where $Y = 1 + (1 - y)^2$, F_2 is the main component of the cross section which in the DIS factorisation scheme corresponds to the sum of the momentum densities of the quarks and antiquarks weighted by the squares of their charges, F_L is the longitudinal structure function and δ_r is a term accounting for radiative corrections. In the Q^2 range considered in this analysis, $Q^2 < 80$ GeV 2 , the contributions from Z^0 exchange and $Z^0 - \gamma$ interference are well below 1% and were ignored. The contribution of F_L to the cross section relative to that from F_2 is given by $(y^2/Y) \cdot (F_L/F_2)$. For the determination of F_2 , the F_L contribution was taken from the QCD fits to the structure function data obtained by ZEUS [2] and H1 [46], which may be approximated by $F_L = 0.2F_2$. The contribution of F_L to the cross section in the highest y (= lowest x) bin of this analysis was 3.8%, decreasing to 1.5% for the next highest y -bin. For the other bins, the F_L contribution is below 1%. The uncertainties of the F_L corrections were estimated to be below 20%; the resulting uncertainties on F_2 are below 1%.

The measured F_2 values are listed in Table 2 and shown in Fig. 11. The data are compared to the predictions of the ZEUS QCD fit [2] obtained from the previous ZEUS F_2 measurements [20]. The fit describes the data well. The proton structure function, F_2 , rises rapidly as $x \rightarrow 0$ for all values of Q^2 , the slope increasing as Q^2 increases.

The form:

$$F_2 = c \cdot x^{-\lambda}, \quad (5)$$

was fitted for every Q^2 bin to the F_2 data. Here λ is related to the intercept of the Pomeron trajectory, $\lambda = \alpha_{IP}(0) - 1$. For later comparison with the diffractive results, these α_{IP} values will be referred to as α_{IP}^{tot} . The resulting values for c and $\alpha_{IP}^{\text{tot}}(0)$ are listed in Table 3. Within errors, c is independent of Q^2 . Figure 12 shows that $\alpha_{IP}^{\text{tot}}(0)$ lies above the ‘soft

Pomeron' value of $1.096^{+0.012}_{-0.009}$ deduced from hadron-hadron scattering data [47, 48] ; it rises approximately linearly with $\ln Q^2$ from $\alpha_{IP}^{\text{tot}}(0) = 1.155 \pm 0.011(\text{stat.})^{+0.007}_{-0.011}(\text{syst.})$ at $Q^2 = 2.7 \text{ GeV}^2$, to $1.307 \pm 0.019(\text{stat.})^{+0.027}_{-0.037}(\text{syst.})$ at $Q^2 = 55 \text{ GeV}^2$, in agreement with previous observations [49, 50]. A Pomeron intercept which changes with Q^2 violates the assumption of single Pomeron exchange plus Regge factorisation of the vertex functions.

The total cross section for virtual photon-proton scattering, $\sigma_{\gamma^*p}^{\text{tot}} \equiv \sigma_T(x, Q^2) + \sigma_L(x, Q^2)$, was extracted from the measurement of F_2 using the relation

$$\sigma_{\gamma^*p}^{\text{tot}} = \frac{4\pi^2\alpha}{Q^2(1-x)} F_2(x, Q^2), \quad (6)$$

which is valid for $4m_p^2x^2 \ll Q^2$ [51–53]. The total cross section values are listed in Table 4 for fixed Q^2 as a function of W . The total cross section multiplied by Q^2 , shown in Fig. 13, exhibits a strong rise with W , becoming steeper as Q^2 increases. This behaviour of $\sigma_{\gamma^*p}^{\text{tot}}$ reflects the x dependence of F_2 as $x \rightarrow 0$, viz. $\sigma_{\gamma^*p}^{\text{tot}} \propto W^{2(\alpha_{IP}^{\text{tot}}(0)-1)}$.

8 Diffractive cross section

The cross section for diffractive scattering via $ep \rightarrow eXN$ can be expressed in terms of the transverse (T) and longitudinal (L) cross sections, σ_T^{diff} and σ_L^{diff} , for $\gamma^*p \rightarrow XN$ as

$$\frac{d\sigma_{\gamma^*p \rightarrow XN}^{\text{diff}}(M_X, W, Q^2)}{dM_X} \equiv \frac{d(\sigma_T^{\text{diff}} + \sigma_L^{\text{diff}})}{dM_X} \approx \frac{2\pi}{\alpha} \frac{Q^2}{(1-y)^2 + 1} \frac{d\sigma_{ep \rightarrow eXN}^{\text{diff}}(M_X, W, Q^2)}{dM_X d\ln W^2 dQ^2}. \quad (7)$$

Here, a term $(1-y^2/[1+(1-y)^2])\sigma_L^{\text{diff}}/(\sigma_T^{\text{diff}} + \sigma_L^{\text{diff}})$ multiplying $(\sigma_T^{\text{diff}} + \sigma_L^{\text{diff}})$ has been neglected [51–53]. Since $y \approx W^2/s$, this approximation reduces the cross section by less than 4% for $W < 200 \text{ GeV}$, and by less than 8% in the highest W bin, 200 - 245 GeV, if $\sigma_L^{\text{diff}} \leq \sigma_T^{\text{diff}}$ ⁶.

⁶ The relative contribution to diffractive production by longitudinal photons is expected to be small [11, 45] except for the production of vector mesons, $\gamma^*p \rightarrow VN$. The processes $\gamma^*p \rightarrow VN$, $V = \rho^0, \omega, \phi$, contribute about 40 - 60% of the diffractive cross section measured in the lowest M_X bin ($0.28 < M_X < 2 \text{ GeV}$) and are dominated by longitudinal photons. Assuming that these were the only contributions from longitudinal photons, extrapolation of the cross sections for $\gamma^*p \rightarrow Vp$ measured at $W < 150 \text{ GeV}$ [36, 37, 54] to higher W gives an effect of the order of 3% at $7 < Q^2 < 27 \text{ GeV}^2$ and $W = 180 \text{ GeV}$. This estimate assumed the same fraction of nucleon dissociation for $\gamma^*p \rightarrow VN$ as for inclusive diffraction. The measured data on J/Ψ production indicate that this process contributes less than 10% of the diffractive cross section in the bin $M_X = 2 - 4 \text{ GeV}$ and therefore even smaller corrections are expected for this M_X bin.

The diffractive cross section $d\sigma^{\text{diff}}/dM_X$ for $\gamma^*p \rightarrow XN$, where $M_N < 2.3$ GeV, is presented in Tables 5 - 10 and Fig. 14, after transporting the measured cross sections to the reference values (M_X, W, Q^2) using the BEKW(mod) fit (see Section 9.3).

These diffractive cross sections do not include contributions from deeply virtual Compton scattering, $\gamma^*p \rightarrow \gamma p$ (DVCS). The DVCS cross sections in the region $5 < Q^2 < 30$ GeV 2 , $40 < W < 140$ GeV have been measured by the ZEUS collaboration [55] and are between 2 and 4% of $\sigma_{\gamma^*p \rightarrow XN}^{\text{diff}}(0.28 < M_X < 2$ GeV).

8.1 W dependence of the diffractive cross section

As seen in Fig. 14, for the bin $M_X = 1.2$ GeV, the diffractive cross section, $d\sigma^{\text{diff}}/dM_X$, shows only a modest increase with W . For higher M_X values, a rise with W is observed for $Q^2 \geq 4$ GeV 2 . The W dependence was quantified by fitting the form

$$\frac{d\sigma_{\gamma^*p \rightarrow XN}^{\text{diff}}}{dM_X} = h \cdot (W/W_0)^{a^{\text{diff}}}, \quad (8)$$

to the data for each (M_X, Q^2) bin with $M_X < 15$ GeV; here $W_0 = 1$ GeV and h, a^{diff} are free parameters. Under the assumption that the diffractive cross section can be described by the exchange of a single Pomeron, the parameter a^{diff} is related to the Pomeron trajectory averaged over t : $\overline{\alpha_{IP}} = 1 + a^{\text{diff}}/4$. In the framework of Regge phenomenology, the cross section for diffractive scattering can be written as [56],

$$d\sigma/dt = f(t) \cdot e^{2(\alpha_{IP}(t)-1) \cdot \ln(s/s_0)}, \quad (9)$$

where t is the four-momentum-transfer squared from γ^* to X , $f(t)$ characterises the t -dependences of the $(\gamma^*IP\gamma^*)$ and $(pIPN)$ vertices, and $s_0 = 1$ GeV 2 . In the present measurement, the diffractive cross section is integrated over t , providing t -averaged values $\overline{\alpha_{IP}}$. Assuming $d\sigma/dt \propto e^{A \cdot t}$ and $\alpha_{IP}(t) = \alpha_{IP}(0) + \alpha'_{IP} \cdot t$, leads to $\alpha_{IP}(0) = \overline{\alpha_{IP}} + \alpha'_{IP}/A$. Taking $A = 7.9 \pm 0.5(\text{stat.})^{+0.9}_{-0.5}(\text{syst.})$ GeV $^{-2}$, as measured by this experiment with the leading proton spectrometer [7]⁷, and $\alpha'_{IP} = 0.25$ GeV $^{-2}$ [47], gives $\alpha_{IP}(0) \approx \overline{\alpha_{IP}} + 0.03 = 1.03 + a^{\text{diff}}/4$. The $\alpha_{IP}(0)$ values deduced from diffractive cross sections are denoted as $\alpha_{IP}^{\text{diff}}(0)$.

The resulting $\alpha_{IP}^{\text{diff}}(0)$ values are listed in Table 11 and shown in Fig. 15 as a function of Q^2 for different M_X intervals. For M_X below 2 GeV, $\alpha_{IP}^{\text{diff}}(0)$ is compatible with the soft Pomeron. For larger M_X , $\alpha_{IP}^{\text{diff}}(0)$ lies above the soft-Pomeron result, the difference increasing with Q^2 .

⁷ This value of A has been determined for $x_{IP} < 0.01$, where diffraction is dominant in the ZEUS LPS data. It is assumed that A for the diffractive contribution remains the same in the region $0.01 < x_{IP} < 0.022$.

Figure 12 compares the Q^2 dependence of $\alpha_{IP}^{\text{tot}}(0)$ with $\alpha_{IP}^{\text{diff}}(0)$ deduced from the diffractive cross section for $2 < M_X < 15$ GeV. Both sets of results lie above the soft-Pomeron result and show a rise with Q^2 . The $\alpha_{IP}^{\text{diff}}(0)$ values lie, however, consistently below those obtained from $\sigma_{\gamma^*p}^{\text{tot}}$, or equivalently F_2 , with $[\alpha_{IP}^{\text{diff}}(0) - 1]/[\alpha_{IP}^{\text{tot}}(0) - 1] \approx 0.5 - 0.7$. Thus, the W dependences of the total and diffractive cross sections yield different Pomeron trajectories.

8.2 Combined W and Q^2 dependence of the diffractive cross section

The assumption of Regge factorisation requires that the Pomeron trajectory be independent of Q^2 if diffractive scattering is to be described by the exchange of a single Pomeron. As a consequence, the W dependence of the diffractive cross section should also be independent of Q^2 . In order to test this hypothesis with the full body of data, the form

$$\frac{d\sigma_{\gamma^*p}^{\text{diff}}}{dM_X} = c(M_X, Q^2) \cdot \left(\frac{W}{W_0}\right)^{4(\overline{\alpha}_{IP}(Q^2) - 1)}, \quad (10)$$

was fitted to the diffractive cross section; here $W_0 = 1$ GeV. The values $\overline{\alpha}_{IP}(Q^2)$ and the constants $c(M_X, Q^2)$ were determined from the fit. In this way, the Q^2 dependence of the W dependence of the diffractive cross section was tested independently of its (M_X, Q^2) dependence. Since the diffractive cross section for $M_X < 2$ GeV receives a substantial contribution from the process $\gamma^*p \rightarrow \rho^0p$, which is dominated by longitudinal photons, and since the W range covered for $M_X > 15$ GeV is rather limited, the fitting was done for the data with $2 < M_X < 15$ GeV. In total, 126 diffractive cross section measurements were included. There are 25 free parameters: four $\overline{\alpha}_{IP}$ values for four bins of Q^2 , and 21 constants $c(M_X, Q^2)$ for three M_X bins (2 - 4, 4 - 8, 8 - 15 GeV) and the corresponding seven Q^2 bins.

The results obtained are presented in Table 12 and shown in Fig. 16. Within errors, $\alpha_{IP}^{\text{diff}}(0)$ is constant for Q^2 between 2.7 and 20 GeV 2 ($\langle Q^2 \rangle = 7.8$ GeV 2) but has a substantially larger value for Q^2 between 20 and 80 GeV 2 ($\langle Q^2 \rangle = 34.6$ GeV 2).

The statistical significance of the rise of $\alpha_{IP}^{\text{diff}}(0)$ with Q^2 was determined by a fit with the following free parameters: the normalisation constants for the four bins in Q^2 , a single value of $\overline{\alpha}_{IP}^{\text{diff}}(0)$ averaged over $2.7 < Q^2 < 20$ GeV 2 and the difference $\Delta\alpha_{IP} \equiv \alpha_{IP}^{\text{diff}}(0, \langle Q^2 \rangle = 34.6 \text{ GeV}^2) - \alpha_{IP}^{\text{diff}}(0, \langle Q^2 \rangle = 7.8 \text{ GeV}^2)$. Considering all systematic uncertainties and their correlations, the fit yielded:

$$\alpha_{IP}^{\text{diff}}(0, \langle Q^2 \rangle = 7.8 \text{ GeV}^2) = 1.1220 \pm 0.0046(\text{stat.})^{+0.0132}_{-0.0114}(\text{syst.}) \quad (11)$$

and

$$\Delta\alpha_{IP}^{\text{diff}} = 0.0714 \pm 0.0140(\text{stat.})^{+0.0047}_{-0.0100}(\text{syst.}). \quad (12)$$

The addition of the statistical and systematic uncertainties in quadrature gives

$$\Delta\alpha_{IP}^{\text{diff}} = 0.0714_{-0.0172}^{+0.0147}. \quad (13)$$

The result establishes the rise of $\alpha_{IP}^{\text{diff}}(0)$ with Q^2 , with a significance of 4.2 standard deviations. Assuming single Pomeron exchange, this observation contradicts Regge factorisation.

This experiment, using the LPS [7], obtained for the kinematic region $x_{IP} < 0.01$, $0.03 < Q^2 < 39$ GeV 2 , the value $\alpha_{IP}^{\text{diff}}(0) = 1.16 \pm 0.02(\text{stat.}) \pm 0.02(\text{syst.})$. Restricting the data in the present analysis to $x_{IP} < 0.01$ gives $\alpha_{IP}^{\text{diff}}(0, \langle Q^2 \rangle = 7.8 \text{ GeV}^2) = 1.1209 \pm 0.0051(\text{stat.})_{-0.0122}^{+0.0136}(\text{syst.})$ and $\Delta\alpha_{IP}^{\text{diff}} = 0.0578 \pm 0.0178(\text{stat.})_{-0.0118}^{+0.0081}(\text{syst.})$ (see Table 13 and Fig. 16). The results are consistent with the fit to the full data set and also in agreement with the LPS result.

8.3 M_X and Q^2 dependences of the diffractive cross section at fixed W

The M_X and Q^2 dependences of the diffractive cross section for $W = 220$ GeV are shown in Fig. 17. The highest- W region is used since it covers the largest range in M_X . The cross section has been multiplied by a factor of Q^2 , since a leading-twist behaviour would give approximate Q^2 independence. For low and medium Q^2 , the M_X spectrum is dominated by the production of states with $M_X < 3$ GeV (Fig. 17a). The cross section for these states decreases rapidly for higher Q^2 , consistent with a predominantly higher-twist behaviour. Above $M_X = 11$ GeV, little dependence on Q^2 is observed (Fig. 17b), corresponding to a leading twist behaviour.

8.4 Diffractive contribution to the total cross section

The relationship between the total and diffractive cross sections can be derived under certain assumptions. For instance, the imaginary part of the amplitude for elastic scattering, $A_{\gamma^*p \rightarrow \gamma^*p}(t, W, Q^2)$, at $t = 0$ can be assumed to be linked to the total cross section by a generalisation of the optical theorem to virtual photon scattering. Assuming that $\sigma_{\gamma^*p}^{\text{tot}} \propto W^{2\lambda}$ and that the elastic and inclusive diffractive amplitudes at $t = 0$ are purely imaginary and have the same W and Q^2 dependences, then $A_{\gamma^*p \rightarrow \gamma^*p}(t = 0, W, Q^2)$ is proportional to $W^{2\lambda}$. Neglecting the real part of the scattering amplitudes, the rise of the diffractive cross section with W should then be proportional to $W^{4\lambda}$, so that the ratio of the diffractive cross section to the total γ^*p cross section,

$$r_{\text{tot}}^{\text{diff}} \equiv \frac{\sigma^{\text{diff}}}{\sigma^{\text{tot}}} = \frac{\int_{M_a}^{M_b} dM_X d\sigma_{\gamma^*p \rightarrow XN, M_N < 2.3 \text{ GeV}}^{\text{diff}} / dM_X}{\sigma_{\gamma^*p}^{\text{tot}}} \quad (14)$$

should behave as $r_{\text{tot}}^{\text{diff}} \propto W^{2\lambda}$.

The ratio $r_{\text{tot}}^{\text{diff}}$ was determined for all $M_a < M_X < M_b$ bins, with the $\sigma_{\gamma^* p}^{\text{tot}}$ values taken from this analysis. The ratio $r_{\text{tot}}^{\text{diff}}$ is shown in Tables 14 - 19 and in Fig. 18. The observed near constancy with W is explained by the dipole saturation model [12, 57].

For $M_X < 2$ GeV, $r_{\text{tot}}^{\text{diff}}$ decreases with increasing Q^2 , while, for $M_X > 4$ GeV, this decrease becomes weaker, and almost no Q^2 dependence is observed for $M_X > 8$ GeV. Here, the diffractive cross section has approximately the same W and Q^2 dependences as the total cross section, in agreement with the conclusion drawn from Fig. 12.

The ratio $\sigma^{\text{diff}}(0.28 < M_X < 35 \text{ GeV}, M_N < 2.3 \text{ GeV})/\sigma^{\text{tot}}$ was evaluated as a function of Q^2 for the highest W bin ($200 < W < 245$ GeV) which provides the best coverage in M_X . The ratio is given in Table 20. At $Q^2 = 4 \text{ GeV}^2$, $\sigma^{\text{diff}}/\sigma^{\text{tot}}$ reaches $15.8_{-1.0}^{+1.2} \%$. It decreases slowly with Q^2 , reaching $9.6_{-0.7}^{+0.7} \%$ at $Q^2 = 27 \text{ GeV}^2$. Diffractive processes thus account for a substantial part of the total deep inelastic cross section.

9 Diffractive structure function of the proton

The diffractive structure function of the proton, $F_2^{D(3)}(\beta, x_{\text{p}}, Q^2)$, is related to the diffractive cross section for $W^2 \gg Q^2$ as follows:

$$\frac{1}{2M_X} \frac{d\sigma_{\gamma^* p \rightarrow XN}^{\text{diff}}(M_X, W, Q^2)}{dM_X} = \frac{4\pi^2\alpha}{Q^2(Q^2 + M_X^2)} x_{\text{p}} F_2^{D(3)}(\beta, x_{\text{p}}, Q^2). \quad (15)$$

If $F_2^{D(3)}$ is interpreted in terms of quark densities, it specifies the probability to find, in a proton undergoing a diffractive reaction, a quark carrying a fraction $x = \beta x_{\text{p}}$ of the proton momentum.

The measurements of $x_{\text{p}} F_2^{D(3)}$ are given in Tables 21 - 24 as a function of β, x_{p} and Q^2 . Figure 19 shows $x_{\text{p}} F_2^{D(3)}$ as a function of x_{p} for different values of β and Q^2 .

9.1 Comparison with other measurements

The measurements of $x_{\text{p}} F_2^{D(3)}$ obtained from this analysis for $M_N < 2.3$ GeV are consistent with those determined previously by this experiment with the M_X method for $M_N < 5.5$ GeV [5].

The measurements of $x_{\text{p}} F_2^{D(3)}$ from this analysis (FPC) have been compared with those from this experiment determined with the leading proton spectrometer (LPS) [7] and from the H1 experiment [4]. Since the three analyses quote the values of $x_{\text{p}} F_2^{D(3)}$ at different (β, Q^2) points, the values of this analysis (FPC) were transported to the (β, Q^2) points

of the other measurements using the BEKW(mod) fit, provided that the (β, Q^2) values of the corresponding FPC measurement satisfied the conditions $0.8 < Q_{FPC}^2/Q^2 < 1.2$, $|\beta_{FPC} - \beta|/\beta < 0.5$. The LPS analysis measures the reaction $\gamma^* p \rightarrow Xp$ while the FPC analysis includes the contribution from proton dissociation, $\gamma^* p \rightarrow XN$, $1.08 < M_N < 2.3$ GeV. The LPS data for $x_{IP} < 0.005$ - where Reggeon contributions to the LPS data are negligible - were used to estimate the fractional contribution $f_{pdissoc}$ from proton dissociation to the FPC results, assuming $f_{pdissoc}$ to be independent of β, x_{IP} and Q^2 . The relative normalisation of the two data sets was determined using the result of the BEKW(mod) fit to the FPC data. This yielded $1 - f_{pdissoc} = 0.70 \pm 0.03$, which shows that about 30% of the diffractive cross section in the FPC analysis comes from nucleon dissociation with masses M_N between 1.08 and 2.3 GeV. Figure 20 shows the LPS data together with the FPC data multiplied by a factor of 0.70. The LPS data for $x_{IP} < 0.01$ agree well with those of the current analysis.

Figure 21 shows a comparison of the measurements of this analysis with that of the H1 collaboration [4] which includes the contribution from nucleon dissociation for $M_N < 1.6$ GeV. No correction was applied to the FPC data to account for the possible difference in $x_{IP} F_2^{D(3)}$ for $M_N < 2.3$ GeV (this analysis) and $M_N < 1.6$ GeV (H1 analysis). Qualitative agreement between the present data and the H1 measurements is observed, with the possible exception of the region of $x_{IP} > 0.01$, where the H1 data include contributions from Reggeon exchange.

9.2 Discussion of the $x_{IP} F_2^{D(3)}$ results from this analysis

The diffractive structure function presented in Fig. 19 is a function of x_{IP} for fixed M_X (or, equivalently fixed β) and Q^2 . For the lowest M_X region - which corresponds to large β values - little dependence on x_{IP} is observed. This is in contrast to the regions with smaller β where $x_{IP} F_2^{D(3)}$ rises strongly as $x_{IP} \rightarrow 0$, reflecting the rapid increase of the diffractive cross section $d\sigma^{\text{diff}}/dM_X$ with W for $M_X > 2$ GeV.

For the following study of $x_{IP} F_2^{D(3)}$ as a function of x_{IP} and β for fixed values of (x_{IP}, Q^2) and (β, Q^2) , respectively, bin centering was done by using the BEKW(mod) fit (Section 9.3).

The Q^2 dependence of $x_{IP} F_2^{D(3)}$ is displayed in Fig. 22 for different values of β and x_{IP} . Different regions in the $\beta - x_{IP}$ space show markedly different behaviours with Q^2 . For $\beta = 0.9$, the region dominated by diffractive production of states with $M_X < 2$ GeV, $x_{IP} F_2^{D(3)}$ is constant or slowly decreasing with Q^2 . For $\beta \leq 0.7$, $x_{IP} F_2^{D(3)}$ increases with increasing Q^2 provided $\beta x_{IP} < 2 \cdot 10^{-3}$. This Q^2 dependence is similar to the scaling violations of the proton structure function F_2 . By noting that $\beta x_{IP} = x$, it can be seen from Fig. 22 that the behaviour of the scaling violations with Q^2 depends primarily on

x rather than on β and x_{P} separately. Disregarding the region $\beta = 0.9$, positive scaling violations dominate at low $x < 0.002$. The fact that the Q^2 dependence of $x_{\text{P}}F_2^{D(3)}$ for fixed β changes with x_{P} shows again that the data are inconsistent with the Regge-factorisation hypothesis, a concept which implies that, for given β and Q^2 , the same Pomeron structure is probed, independently of x_{P} .

Figure 23 shows $x_{\text{P}}F_2^{D(3)}$ as a function of β for fixed (x_{P}, Q^2) . For those (x_{P}, Q^2) values where the measurements cover a wide range in β , $x_{\text{P}}F_2^{D(3)}$ is observed to have a broad maximum around $\beta = 0.5$, a dip near $\beta = 0.1$ and a rise as $\beta \rightarrow 0$.

The data of Fig. 23 can be better visualized by plotting them for fixed x_{P} . Figure 24 shows the results obtained by using the $x_{\text{P}}F_2^{D(3)}$ measurements with $0.5x_0 < x_{\text{P}} < 1.5x_0$, where $x_0 = 0.01$. For each measurement, the $x_{\text{P}}F_2^{D(3)}$ value measured at $x_{\text{P,meas}}$ was transported to $x_{\text{P}} = x_0$ using the BEKW(mod) fit. On average, the difference between measured and transported $x_0F_2^{D(3)}(\beta, x_0, Q^2)$ value was of the order of 5%. Finally, for every (β, Q^2) point, the weighted average of the selected measurements was made.

In a model where diffraction proceeds by the exchange of a Pomeron, the diffractive structure function factorises into the flux of Pomerons and the structure function of the Pomeron, $x_{\text{P}}F_2^{D(3)}(\beta, x_{\text{P}}, Q^2) = \Phi(x_{\text{P}}) \cdot F_2^P(\beta, Q^2)$. Up to a normalisation constant, $x_0F_2^{D(3)}(\beta, x_0, Q^2)$, would represent the structure function of the Pomeron, $F_2^P(\beta, Q^2) = x_0F_2^{D(3)}(\beta, x_0, Q^2)$. In such a model, however, the flux is independent of Q^2 , which is at variance with the data from this analysis, as shown in Fig. 22.

The resulting measurements of $x_0F_2^{D(3)}(\beta, x_0, Q^2)$ are presented in Table 25 and Fig. 24. Several aspects are noteworthy. Firstly, $x_0F_2^{D(3)}(\beta, x_0, Q^2)$ has a maximum near $\beta = 0.5$, consistent with a $\beta(1 - \beta)$ variation. Secondly, in the region of high β , $x_0F_2^{D(3)}(\beta, x_0, Q^2)$ tends to decrease as Q^2 increases from 14 to 27 GeV 2 . Finally, for $\beta < 0.1$, $x_0F_2^{D(3)}$ rises as $\beta \rightarrow 0$, the rise increasing with increasing Q^2 .

The $\beta(1 - \beta)$ dependence is explained in dipole models of diffraction by $\gamma^* \rightarrow q\bar{q}$ splitting [10–13] and two gluon exchange. The rise of $x_0F_2^{D(3)}(\beta, x_0, Q^2)$ as $\beta \rightarrow 0$ and its increase as Q^2 increases is reminiscent of the logarithmic scaling violations of the proton structure function F_2 at low x , which are ascribed to the contribution from the sea.

The data are consistent with the idea that diffractive DIS probes the diffractive PDFs of the proton; their dependence on β and Q^2 is similar to the different Q^2 dependence of the proton inclusive PDFs at different values of x [58]. The positive scaling violations observed for $x = \beta x_{\text{P}} < 2 \times 10^{-3}$ suggest substantial perturbative effects such as gluon emission.

9.3 Comparison with the BEKW model

The BEKW model [45] provides a general parametrisation for inclusive diffraction in DIS and allows the identification of certain subprocesses by their characteristic behaviour in β and Q^2 . In the model, the incoming virtual photon fluctuates into a $q\bar{q}$ or $q\bar{q}g$ dipole which interacts with the target proton via two-gluon exchange. The β spectrum and the scaling behaviour in Q^2 are derived from the wave functions of the incoming transverse (T) or longitudinal (L) photon on the light cone in the non-perturbative limit. The x_{IP} dependence of the cross section is not predicted by the model but is to be determined by experiment. Specifically

$$x_{\text{IP}} F_2^{D(3)}(\beta, x_{\text{IP}}, Q^2) = c_T \cdot F_{q\bar{q}}^T + c_L \cdot F_{q\bar{q}}^L + c_g \cdot F_{q\bar{q}g}^T, \quad (16)$$

where

$$F_{q\bar{q}}^T = \left(\frac{x_0}{x_{\text{IP}}}\right)^{n_T(Q^2)} \cdot \beta(1 - \beta), \quad (17)$$

$$F_{q\bar{q}}^L = \left(\frac{x_0}{x_{\text{IP}}}\right)^{n_L(Q^2)} \cdot \frac{Q_0^2}{Q^2 + Q_0^2} \cdot [\ln(\frac{7}{4} + \frac{Q^2}{4\beta Q_0^2})]^2 \cdot \beta^3 (1 - 2\beta)^2, \quad (18)$$

$$F_{q\bar{q}g}^T = \left(\frac{x_0}{x_{\text{IP}}}\right)^{n_g(Q^2)} \cdot \ln(1 + \frac{Q^2}{Q_0^2}) \cdot (1 - \beta)^\gamma. \quad (19)$$

The contribution from longitudinal photons coupling to $q\bar{q}$ is limited to β values close to unity. The $q\bar{q}$ contribution from transverse photons is expected to have a broad maximum around $\beta = 0.5$, while the $q\bar{q}g$ contribution becomes important at small β , provided γ is large. The original BEKW model also includes a higher-twist term for $q\bar{q}$ produced by transverse photons. The present data are insensitive to this term, and therefore it has been neglected.

For $F_{q\bar{q}}^L$, the term $(\frac{Q_0^2}{Q^2})$ provided by BEKW was replaced by the factor $(\frac{Q_0^2}{Q^2 + Q_0^2})$ to avoid problems as $Q^2 \rightarrow 0$. The powers $n_{T,L,g}(Q^2)$ were assumed by BEKW to be of the form $n(Q^2) = n_0 + n_1 \cdot \ln[1 + \ln(\frac{Q^2}{Q_0^2})]$. The rise of $\alpha_{\text{IP}}(0)$ with $\ln Q^2$ observed in the present data suggested using the form $n(Q^2) = n_0 + n_1 \ln(1 + \frac{Q^2}{Q_0^2})$. The modified BEKW form will be referred to as BEKW(mod). Taking $x_0 = 0.01$ and $Q_0^2 = 0.4 \text{ GeV}^2$, the BEKW(mod) form gives a good description of the data, viz. $\chi^2 = 112$ for 188 dof. According to the fit, all the coefficients n_0 and n_1 for the longitudinal component can be set to zero, and the powers n_T, n_g are the same, within errors, for the $q\bar{q}$ and $q\bar{q}g$ components produced by transverse photons. This leads to: $c_T = 0.112 \pm 0.003$, $c_L = 0.154 \pm 0.012$, $c_g = 0.0091 \pm 0.0003$, $n_1^{T,g} = 0.067 \pm 0.004$ and $\gamma = 8.62 \pm 0.55$ with $\chi^2 = 114$ for 193 dof. The value of the power γ is considerably larger than the value of about three expected by BEKW. Results from a similar analysis of the LPS data can be found elsewhere [7].

Figures 22, 23 and 25 compare the measurement of $x_{IP}F_2^{D(3)}(\beta, x_{IP}, Q^2)$ as a function of x_{IP} , β and Q^2 with the BEKW(mod) fit. The fit describes the data well. The weak rise of $x_{IP}F_2^{D(3)}$ as $x_{IP} \rightarrow 0$ observed for $M_X = 1.2$ GeV, and the strong rise for $M_X \geq 3$ GeV, are explained by the BEKW fit as follows: the high β region ($\beta > 0.9$) receives substantial contributions from longitudinal photons with a weak dependence on x_{IP} , while transverse photons dominate at lower β and lead to a strong rise as $x_{IP} \rightarrow 0$. The observed increase of the rise of $x_{IP}F_2^{D(3)}$ as $x_{IP} \rightarrow 0$ with increasing Q^2 is accommodated in the model by assuming that the power $n_T(Q^2)$ increases with Q^2 . In the BEKW model⁸, the broad maximum seen in the β distribution around $\beta = 0.5$ is a result of the dominance of the $q\bar{q}$ configuration at medium β , and the rise towards small β is a result of the $(q\bar{q}g)$ configuration. The good agreement of the BEKW fit with the data for $M_X > 2$ GeV lends strong support to the dipole picture.

10 Conclusions

A simultaneous measurement of the proton structure function F_2 , the diffractive γ^*p cross section and the diffractive structure function has been made. The kinematic range of the measurement was $2.2 < Q^2 < 80$ GeV², $37 < W < 245$ GeV and $0.28 < M_X < 35$ GeV. The forward plug calorimeter (FPC) was used to extend the range of M_X compared to previous measurements. The M_X method was used to extract the diffractive cross section; the method is shown to exclude non-peripheral as well as Reggeon contributions to the cross section.

The results for the proton structure function $F_2(x, Q^2)$ are in good agreement with previous measurements of the ZEUS collaboration. The F_2 data were analysed in the framework of Regge phenomenology. The intercept of the Pomeron trajectory of these data is significantly higher than that measured in hadron-hadron collisions ('soft Pomeron', $\alpha_{IP}(0) = 1.096^{+0.012}_{-0.009}$) and is a strong function of Q^2 : $\alpha_{IP}^{\text{tot}}(0) = 1.155 \pm 0.011(\text{stat.})^{+0.007}_{-0.011}(\text{syst.})$ at $Q^2 = 2.7$ GeV² and $\alpha_{IP}^{\text{tot}}(0) = 1.307 \pm 0.019(\text{stat.})^{+0.027}_{-0.037}(\text{syst.})$ at $Q^2 = 55$ GeV². The Q^2 dependence of the Pomeron intercept corresponds to the rise of F_2 towards low x , which increases with Q^2 and which has been observed previously at HERA. In a Regge approach, this shows that F_2 , and the total γ^*p cross section, cannot be interpreted in terms of the exchange of a single Pomeron combined with the assumption of Regge factorisation.

⁸ Although the BEKW(mod) fit gives an excellent description of the data from this analysis, its prediction for the contribution from longitudinal photons at low M_X and low Q^2 is at variance with existing data on vector meson production. For $M_X < 2$ GeV, the contribution from longitudinal photons accounts for at least $\approx 20\%$ of $x_{IP}F_2^{D(3)}$. The BEKW(mod) fit curves for the longitudinal photon contribution at $M_X < 2$ GeV (dotted lines in Fig. 25) are in broad agreement with the data for $Q^2 \geq 6$ GeV², but are too low at lower Q^2 .

The measured diffractive DIS cross section is in good agreement with previous ZEUS measurements when proton dissociation is taken into account. The diffractive cross section for $0.28 < M_X < 2$ GeV shows a weak dependence on W but a much stronger decrease than $1/Q^2$, characteristic of a higher twist behaviour. For $M_X > 8$ GeV, the cross section decreases as $1/Q^2$, indicating a leading twist behaviour. The diffractive cross section was also analysed in terms of Regge phenomenology. The excess of the intercept of the Pomeron trajectory above unity is about half of that extracted from the F_2 data, but still significantly higher than that of the soft Pomeron. The Pomeron intercept rises by $\Delta\alpha_{IP}^{\text{diff}} = 0.0714 \pm 0.0140(\text{stat.})^{+0.0047}_{-0.0100}(\text{syst.})$ between Q^2 of 7.8 and 27 GeV 2 . This establishes a Q^2 dependence of the Pomeron intercept and shows that the diffractive DIS as well as the inclusive DIS cross sections cannot be interpreted as resulting from single Pomeron exchange combined with the assumption of Regge factorisation.

The ratio of the diffractive to the total γ^*p cross section was studied. For fixed M_X and Q^2 , the ratio is flat as a function of W in the kinematic range of these measurements. For $0.28 < M_X < 35$ GeV, $W = 220$ GeV, the ratio is $15.8^{+1.2}_{-1.0}\%$ at $Q^2 = 4$ GeV 2 and $9.6^{+0.7}_{-0.7}\%$ at $Q^2 = 27$ GeV 2 .

The diffractive cross section was also analysed in terms of the diffractive structure function of the proton $F_2^{D(3)}(\beta, x_{IP}, Q^2)$. The β and Q^2 dependences of $x_{IP}F_2^{D(3)}$ are a function of x_{IP} ; this is expected in view of the Regge factorisation breaking observed for the diffractive cross section. The pattern of scaling violations depends primarily on the proton variables x and Q^2 ; for $\beta < 0.9$, positive scaling violations are observed when $x < 0.002$. The analysis of $x_{IP}F_2^{D(3)}(\beta, x_{IP}, Q^2)$ for $x_{IP} = x_0 = 0.01$ exhibits several remarkable properties: $x_0F_2^{D(3)}(\beta, x_0, Q^2)$ shows a broad maximum near $\beta = 0.5$ consistent with a $\beta(1 - \beta)$ variation as expected by dipole models for $\gamma^* \rightarrow q\bar{q}$ splitting; for $\beta < 0.1$, $x_0F_2^{D(3)}$ rises as $\beta \rightarrow 0$, the rise increasing with increasing Q^2 . The positive scaling violations observed for $\beta < 0.1$ suggest that diffraction in DIS receives substantial contributions from perturbative effects.

The results of this paper show that Regge phenomenology cannot give a good description of the diffractive and total DIS cross section without extensive modifications that would undermine the simplicity of the Regge approach. The large fraction of the DIS cross section that is diffractive even at high Q^2 , and the leading twist nature of the diffractive cross section at higher M_X may mean that some assumptions [58] inherent in the DGLAP analysis of the structure function F_2 need to be reexamined.

Acknowledgements

We thank the DESY directorate for their strong support and encouragement. The effort of the HERA machine group is gratefully acknowledged. We thank the DESY computing

and network services for their support. The construction, testing and installation of the ZEUS detector have been possible by the effort of many people not listed as authors. We would like to thank, in particular, J. Hauschildt and K. Löffler (DESY), R. Feller, E. Möller and H. Prause (I. Inst. for Exp. Phys., Univ. Hamburg), A. Maniatis (II. Inst. for Exp. Phys., Univ. Hamburg), N. Wilfert and the members of the mechanical workshop of the Faculty of Physics from the Freiburg University for their work on the FPC. We would like to thank also L. Lindemann for his contributions at the start of this analysis.

Appendix

A Reconstruction of W with the weighting method

The value of W is reconstructed using the weighted average of the values determined from the electron and the hadron measurements (the ‘weighting method’) denoted by W_W . The electron kinematics yields W_e :

$$\begin{aligned} W_e^2 &= (P + k - k')^2 \\ &= 2P(k - k') + P^2 + (k - k')^2 \\ &= 2E_p[2E_e - E'_e(1 - \cos \theta_e)] + m_p^2 - Q^2, \end{aligned}$$

where m_p is the mass of the proton. The measurement accuracy of W_e , ΔW_e , depends on the uncertainties with which E'_e and θ_e are measured,

$$\Delta W_e^2 = -[2E_p(1 - \cos \theta_e) + 2E_e(1 + \cos \theta_e)]\Delta E'_e + 2(E_p E'_e - E_e E'_e)\Delta \cos \theta_e.$$

Monte Carlo (MC) studies yielded for the resolutions $\Delta E'_e \approx 5/E'_e \oplus 0.08$ and $\Delta \theta_e \approx 0.007$, where the energies are given in units of GeV and $\Delta \theta_e$ in radians. The dominant contribution to ΔW_e comes from the uncertainty in the measurement of the electron energy. This can be serious for low values of W ($W < 60$ GeV) where E'_e is close to E_e : for instance, at low Q^2 and when the measured $E'_e > E_e$, W_e^2 becomes negative.

The energies E_h and production angles θ_h of the EFOs provide the hadronic measurement of W :

$$W_h^2 \approx 2E_p \sum_h E_h(1 - \cos \theta_h),$$

with an uncertainty of

$$\Delta W_h^2 = 2E_p \sum_h (1 - \cos \theta_h)\Delta E_h + 2E_p \sum_h E_h \sin \theta_h \Delta \theta_h.$$

The summation is performed over all hadronic EFOs. For the hadronic measurement, the MC simulation yields $\Delta E_h \approx 0.8\sqrt{E_h} \oplus 0.04E_h$ and $\Delta \theta_h \approx 0.07$. The uncertainty results largely from fluctuations of the energy loss in the material ahead of CAL, and from neutrinos and muons produced in the final state.

Using the MC to estimate the errors shows that at low W , where W_e provides a poor measurement of W , the value of W_h is rather precise, while the opposite is true for high

values of W . The weighting method combines the two measurements for W by weighting them with the inverse of the squares of their estimated errors, $g_e = \frac{W^2}{\Delta W_e^2}$ and $g_h = \frac{W^2}{\Delta W_h^2}$:

$$W_W^2 = \frac{g_e^2 W_e^2 + g_h^2 W_h^2}{g_e^2 + g_h^2}.$$

In order to arrive at reliable estimates for g_e, g_h , it is essential to have an estimate for W . This is achieved with the double-angle (DA) measurement [59] which relies only on the measurement of the angles of the scattered electron and of the hadronic system.

B Extraction of the diffractive contribution with the M_X method

In non-peripheral DIS, the incident proton is broken up and the remnant is a coloured object. This gives rise to a substantial amount of initial- and final-state radiation, populating the region between the incident proton and the current jet. The scaling of the position of the maximum and the exponential fall-off of the $\ln M_X^2$ distribution follow from the assumption of uniform, uncorrelated particle emission in rapidity ($\mathcal{Y} = \frac{1}{2} \ln \frac{E+P_L}{E-P_L}$, where E, P_L are the energy and longitudinal momentum of the particle) along the beam axis in the γ^*p system [40, 41]. For an (idealized) uniform \mathcal{Y} distribution between maximum and minimum rapidities of \mathcal{Y}_{\max} and \mathcal{Y}_{\min} , respectively, the total c.m. energy W is given by

$$W^2 \approx c_0 \cdot \exp(\mathcal{Y}_{\max} - \mathcal{Y}_{\min}),$$

assuming $(\mathcal{Y}_{\max} - \mathcal{Y}_{\min}) \gg 1$. Here, c_0 is a constant. The mass M_X of the particle system that can be observed in the detector is reduced by the loss of particles (mainly) through the forward beam hole:

$$M_X^2 \approx c_0 \cdot \exp(\mathcal{Y}_{\text{limit}}^{\text{det}} - \mathcal{Y}_{\min}) \approx W^2 \cdot \exp(\mathcal{Y}_{\text{limit}}^{\text{det}} - \mathcal{Y}_{\max}), \quad (20)$$

where $\mathcal{Y}_{\text{limit}}^{\text{det}}$ denotes the limit of the calorimetric acceptance in the forward direction. Equation (20) predicts scaling of the $\ln M_X^2$ distribution when plotted as function of $\ln(M_X^2/W^2)$, in agreement with the behaviour of the data.

The value of M_X will fluctuate due to a finite probability $P(\Delta\mathcal{Y})$ that no particles are emitted between $\mathcal{Y}_{\text{limit}}^{\text{det}}$ and $\mathcal{Y}_{\text{limit}}^{\text{det}} - \Delta\mathcal{Y}$. This generates a gap of size $\Delta\mathcal{Y}$. The assumption of uncorrelated particle emission leads to a Poissonian rapidity gap distribution, $P(\Delta\mathcal{Y}) = \exp(-\lambda\Delta\mathcal{Y})$, resulting in an exponential fall-off of the $\ln M_X^2$ distribution,

$$\frac{d\mathcal{N}^{\text{non-diff}}}{d \ln M_X^2} = c \cdot \exp(b \cdot \ln M_X^2), \quad (21)$$

where the slope b and the parameter c can be determined from the data. The exponential fall-off of the $\ln M_X^2$ distribution towards small values of $\ln M_X^2$ is indeed found for models which include QCD leading-order matrix elements, parton showers and fragmentation, such as DJANGOH (see shaded area in Fig. 4). The exponential fall-off holds for $\ln M_X^2 \leq \ln W^2 - \eta_0$ over two units of rapidity, where $\eta_0 \approx 2$.

In the M_X method, the diffractive contribution is identified as the excess of events towards small M_X above the exponential fall-off of the non-diffractive contribution. In a Triple Regge model [60–62], the diffractive cross section is approximately of the form

$$\frac{d\sigma_{\gamma^* p \rightarrow XN}^{\text{diff}}}{d \ln M_X^2} \propto \exp[(1 + \alpha_k(0) - 2\bar{\alpha}_j) \cdot \ln M_X^2].$$

Here, $\bar{\alpha}_j$ is the trajectory exchanged in the t channel between the incoming proton and the outgoing system N , averaged over the t distribution, as seen in Fig. 5. The parameter $\alpha_k(0)$ is the intercept of the trajectory describing the production of the system X by the scattering of γ^* on a Regge-pole with t averaged intercept $\bar{\alpha}_j$. For large M_X , $\alpha_k(0)$ is expected to be 1. Pomeron exchange in the t -channel with $\bar{\alpha}_j \approx 1$ leads then to $1 + \alpha_k(0) - 2\bar{\alpha}_j = 0$ and to a constant $\ln M_X^2$ spectrum:

$$\frac{d\sigma_{\gamma^* p \rightarrow XN}^{\text{diff}}}{d \ln M_X^2} = \text{constant}.$$

If, instead of the Pomeron, the highest-lying Reggeon trajectory ($\bar{\alpha}_j \approx 0.5$) is exchanged in the t -channel, then the $\ln M_X^2$ spectrum for this contribution rises exponentially towards large $\ln M_X^2$:

$$\frac{d\sigma_{\gamma^* p \rightarrow XN}^{\text{diff}}}{d \ln M_X^2} \propto \exp(b_{IR} \cdot \ln M_X^2),$$

with $b_{IR} = 1$. Hence, Reggeon exchange in the t channel leads to an exponential rise of the $\ln M_X^2$ distribution. Note also that lower-lying Regge trajectories produce an even larger exponential slope b_{IR} . Therefore, identifying the diffractive contribution as the excess of events above the exponential fall-off of the $\ln M_X^2$ -distribution suppresses not only the non-diffractive contribution arising from colour exchange but also the contributions from Reggeon exchange.

C Reggeon contribution to the $\ln M_X^2$ spectrum

The recent ZEUS measurement of diffraction in DIS with the LPS [7] allows the Reggeon exchange contribution to the reaction $\gamma^* p \rightarrow Xp$ to be estimated. In the LPS analysis,

the diffractive structure function of the proton, $x_{IP}F_2^{D(3)}(\beta, x_{IP}, Q^2)$, shows a rise towards small x_{IP} , and a rise towards large x_{IP} , with a minimum near $x_{IP} = 0.01 - 0.02$. The rise towards large x_{IP} is indicative of a Reggeon contribution. The LPS data were used to estimate the size of the Reggeon contribution by fitting them to a sum of Pomeron and Reggeon contributions, assuming Regge factorisation:

$$x_{IP}F_2^{D(3)}(\beta, x_{IP}, Q^2) = c_{IP} \cdot x_{IP}F_2^{D(3)IP}(\beta, x_{IP}, Q^2) + c_{IR} \cdot x_{IP}F_2^{D(3)IR}(\beta, x_{IP}, Q^2). \quad (22)$$

The Pomeron contribution (*IP*) was taken to equal the result of the BEKW(mod) fit to the FPC data multiplied by the factor c_{IP} which accounts for the fact that the LPS data do not include proton dissociation. The LPS data for $x_{IP} < 0.005$ yielded $c_{IP} = 0.70 \pm 0.03$. For the Reggeon contribution (*IR*), the following ansatz was made :

$$x_{IP}F_2^{D(3)IR}(\beta, x_{IP}, Q^2, t) = \frac{x_{IP} \cdot e^{B_{IR}t}}{x_{IP}^{2\alpha_{IR}(t)-1}} F_2^{D(2)IR}(\beta, Q^2).$$

Defining

$$g_{IR}(x_{IP}) = \int_{t_{\max}}^{t_{\min}} dt \frac{e^{B_{IR}t}}{x_{IP}^{2\alpha_{IR}(t)-2}},$$

taking $t_{\min} = 0$, $t_{\max} = 1 \text{ GeV}^2$ and $\alpha_{IR}(t) = \alpha_{IR}(0) + \alpha'_{IR} \cdot t$ leads to

$$g_{IR}(x_{IP}) = \frac{1}{(B_{IR} - 2\alpha'_{IR} \cdot \ln x_{IP}) \cdot x_{IP}^{(2\alpha_{IR}(0)-2)}}.$$

and to

$$x_{IP}F_2^{D(3)IR}(\beta, x_{IP}, Q^2) = g_{IR}(x_{IP}) \cdot F_2^{D(2)IR}(\beta, Q^2).$$

Following H1 [4], the Reggeon parameters were assumed to be: $\alpha_{IR}(0) = 0.55$, $\alpha'_{IR} = 0.9 \text{ GeV}^{-2}$ and $B_{IR} = 2 \text{ GeV}^{-2}$. While the LPS data are the most precise information on the Reggeon contribution available, the data are still too sparse to effectively constrain the parameter c_R in a fit to Eq. 22. In order to obtain a rough estimation needed for this study, the assumption $x_{IP}F_2^{D(3)IR}(\text{at } x_{IP} = 0.06) \approx x_{IP}F_2^{D(3)IP}(\text{at } x_{IP} = 0.002)$ independent of β and Q^2 was made (see Fig. 20). This allowed the determination, $c_R = 0.39$; the χ^2/dof of the resulting description of Eq. 22 to the LPS data was 89/78.

The Reggeon contribution extracted from the LPS data was multiplied by a factor of $1/c_{IP} = 1.43$. This factor accounts for the extra contribution from proton dissociation in the present analysis. The contribution from charged isovector Reggeons, which cannot contribute to the LPS data, was assumed to be negligible [63].

The relation between $F_2^{D(3)IR}$ and the $\ln M_X^2$ spectrum from the present analysis is given by,

$$\frac{d\sigma_{\gamma^* p \rightarrow X N}^{IR}}{d \ln M_X^2} = 4\pi^2 \alpha \frac{M_X^2}{Q^2(Q^2 + M_X^2)} \cdot c_{IR}/c_{IP} \cdot x_{IP} F^{D(3)IR}(\beta, x_{IP}, Q^2).$$

Figure 6 compares the distribution of $\ln M_X^2$ for the lowest and highest W bins at low and high Q^2 for the data together with the expectations from Reggeon exchange which lies below the total non-diffractive contribution predicted by the fit to the $\ln M_X^2$ distributions.

References

- [1] V.N. Gribov and L.N. Lipatov, Sov. J. Nucl. Phys. **15**, 438 (1972);
L.N. Lipatov, Sov. J. Nucl. Phys. **20**, 94 (1975);
Yu.L. Dokshitzer, Sov. Phys. JETP **46**, 641 (1977);
G. Altarelli and G. Parisi, Nucl. Phys. **B 126**, 298 (1977).
- [2] ZEUS Coll., S. Chekanov et al., Phys. Rev. **D 67**, 12007 (2003).
- [3] ZEUS Coll., M. Derrick et al., Phys. Lett. **B 315**, 481 (1993).
- [4] H1 Coll., C. Adloff et al., Z. Phys. **C 76**, 613 (1997).
- [5] ZEUS Coll., J. Breitweg et al., Eur. Phys. J. **C 6**, 43 (1999).
- [6] ZEUS Coll., S. Chekanov et al., Eur. Phys. J. **C 25**, 169 (2002).
- [7] ZEUS Coll., S. Chekanov et al., Preprint DESY-04-131, 2004. Submitted to Eur. Phys. J.
- [8] L. Trentadue and G. Veneziano, Phys. Lett. **B 323**, 201 (1994).
- [9] J.C. Collins, Phys. Rev. **D 57**, 3051 (1998);
Erratum, ibid. **D 61**, 019902 (2000).
- [10] J.D. Bjorken, *Proc. Int. Symp. Electron and Photon Interactions at High Energies*, N. Mistry (ed.), p. 282. Cornell University, Cornell, USA (1971);
J.D. Bjorken, J. Kogut and D. Soper, Phys. Rev. **D 3**, 1382 (1971);
J.D. Bjorken and J. Kogut, Phys. Rev. **D 8**, 1341 (1973).
- [11] N.N. Nikolaev and B.G. Zakharov, Z. Phys. **C 53**, 331 (1992);
M. Genovese, N.N. Nikolaev and B.G. Zakharov, Sov. Phys. JETP **81**, 625 (1995);
M. Bertini et al., Phys. Lett. **B 422**, 238 (1998).
- [12] K. Golec-Biernat and M. Wüsthoff, Phys. Rev. **D 59**, 014017 (1999);
K. Golec-Biernat and M. Wüsthoff, Phys. Rev. **D 60**, 114023 (1999).
- [13] A.H. Mueller, Nucl. Phys. **B 335**, 115 (1990).
- [14] G. Alberi and G. Goggi, Phys. Rep. **74**, 1 (1981);
K. Goulianos, Phys. Rep. **101**, 169 (1983).
- [15] G. Ingelman and P.E. Schlein, Phys. Lett. **B 152**, 256 (1985).
- [16] ZEUS Coll., U. Holm (ed.), *The ZEUS Detector*, Status Report (unpublished), DESY (1993), available on <http://www-zeus.desy.de/bluebook/bluebook.html>.
- [17] ZEUS Coll., M. Derrick et al., Phys. Lett. **B 293**, 465 (1992).

- [18] N. Harnew et al., Nucl. Inst. Meth. **A 279**, 290 (1989);
 B. Foster et al., Nucl. Phys. Proc. Suppl. **B 32**, 181 (1993);
 B. Foster et al., Nucl. Inst. Meth. **A 338**, 254 (1994).
- [19] M. Derrick et al., Nucl. Inst. Meth. **A 309**, 77 (1991);
 A. Andresen et al., Nucl. Inst. Meth. **A 309**, 101 (1991);
 A. Caldwell et al., Nucl. Inst. Meth. **A 321**, 356 (1992);
 A. Bernstein et al., Nucl. Inst. Meth. **A 336**, 23 (1993).
- [20] ZEUS Coll., S. Chekanov et al., Eur. Phys. J. **C 21**, 443 (2001).
- [21] A. Bamberger et al., Nucl. Inst. Meth. **A 401**, 63 (1997).
- [22] A. Dwurazny et al., Nucl. Inst. Meth. **A 277**, 176 (1989).
- [23] A. Bamberger et al., Nucl. Inst. Meth. **A 450**, 235 (2000).
- [24] F. Goebel, Ph.D. Thesis, Hamburg University, Hamburg (Germany), DESY-THESIS-2001-049 (2001).
- [25] H. Abramowicz, A. Caldwell and R. Sinkus, Nucl. Inst. Meth. **A 365**, 508 (1995).
- [26] G. Briskin, Ph.D. Thesis, Tel Aviv University, Tel Aviv (Israel), DESY-THESIS-1998-036 (1998).
- [27] A. Kwiatkowski, H. Spiesberger and H.-J. Möhring, Comp. Phys. Comm. **69**, 155 (1992). Also in *Proc. Workshop Physics at HERA*, Ed. W. Buchmüller and G. Ingelman, (DESY, Hamburg, 1991).
- [28] K. Charchula, G.A. Schuler and H. Spiesberger, Comp. Phys. Comm. **81**, 381 (1994).
- [29] H.L. Lai et al., Phys. Rev. **D 55**, 1280 (1997).
- [30] D. Haidt, 2002. private communication.
- [31] L. Lönnblad, Comp. Phys. Comm. **71**, 15 (1992).
- [32] T. Sjöstrand, Comp. Phys. Comm. **82**, 74 (1994).
- [33] H. Jung, Comp. Phys. Comm. **86**, 147 (1995).
- [34] G. Ingelman, A. Edin and J. Rathsman, Comp. Phys. Comm. **101**, 108 (1997).
- [35] K. Muchorowski, Ph.D. Thesis, Warsaw University, Warsaw (Poland), (1996).
- [36] ZEUS Coll., J. Breitweg et al., Eur. Phys. J. **C 6**, 603 (1999).
- [37] ZEUS Coll., J. Breitweg et al., Eur. Phys. J. **C 12**, 393 (2000).
- [38] H. Lim, Ph.D. Thesis, The Graduate School, Kyungpook National University, Taegu (Republic of Korea), (2002).
- [39] R. Brun et al., GEANT3, Technical Report CERN-DD/EE/84-1, CERN, 1987.

- [40] ZEUS Coll., M. Derrick et al., *Z. Phys. C* **70**, 391 (1996).
- [41] R.P. Feynman, *Photon-Hadron Interactions*. Benjamin, New York, 1972.
- [42] V. Barone and E. Predazzi, *High-Energy Particle Diffraction*, Springer Verlag, Heidelberg, 2002, and references therein.
- [43] A. Donnachie and P.V. Landshoff, *Phys. Lett. B* **191**, 309 (1987).
- [44] A. Donnachie and P.V. Landshoff, *Nucl. Phys. B* **303**, 634 (1988).
- [45] J. Bartels et al., *Eur. Phys. J. C* **7**, 443 (1999).
- [46] H1 Coll., C. Adloff et al., *Eur. Phys. J. C* **21**, 33 (2001).
- [47] A. Donnachie and P.V. Landshoff, *Nucl. Phys. B* **244**, 322 (1984);
A. Donnachie and P.V. Landshoff, *Phys. Lett. B* **296**, 227 (1992).
- [48] J.R. Cudell, K. Kang and S.K. Kim, *Phys. Lett. B* **395**, 311 (1997).
- [49] ZEUS Coll., J. Breitweg et al., *Eur. Phys. J. C* **7**, 609 (1999).
- [50] H1 Coll., C. Adloff et al., *Phys. Lett. B* **520**, 183 (2001).
- [51] L.N. Hand, *Phys. Rev. 129*, 1834 (1963).
- [52] S.D. Drell and J.D. Walecka, *Ann. Phys. 28*, 18 (1964).
- [53] F.J. Gilman, *Phys. Rev. 167*, 1365 (1968).
- [54] ZEUS Coll., J. Breitweg et al., *Phys. Lett. B* **487**, 273 (2000).
- [55] ZEUS Coll., S. Chekanov et al., *Phys. Lett. B* **573**, 46 (2003).
- [56] See e.g. P.D.B. Collins, *An Introduction to Regge Theory and High Energy Physics*. Cambridge University Press, 1977.
- [57] K. Golec-Biernat, *J. Phys. G* **28**, 1057 (2002).
- [58] A.D. Martin, M.G. Ryskin and G. Watt, Preprint hep-ph/0406225, 2004.
- [59] S. Bentvelsen, J. Engelen and P. Kooijman, *Proc. Workshop on Physics at HERA*, W. Buchmüller and G. Ingelman (eds.), Vol. 1, p. 23. Hamburg, Germany, DESY (1992);
K.C. Höger, *ibid. Vol. 1*, p. 43 (1992).
- [60] A.H. Mueller, *Phys. Rev. D* **2**, 2963 (1970).
- [61] A.H. Mueller, *Phys. Rev. D* **4**, 150 (1971).
- [62] R. D. Field and G. C. Fox, *Nucl. Phys. B* **80**, 367 (1974).
- [63] K. Golec-Biernat, J. Kwieciński and A. Szczurek, *Phys. Rev. D* **56**, 3955 (1997).

Q^2 (GeV 2)	2.2 - 3	3 - 5	5 - 7	7 - 10	10 - 20	20 - 40	40 - 80
Q_{ref}^2 (GeV 2)	2.7	4	6	8	14	27	55
W (GeV)	37 - 55	55 - 74	74 - 99	99 - 134	134 - 164	164 - 200	200 - 245
W_{ref} (GeV)	45	65	85	115	150	180	220
M_X (GeV)	0.28 - 2	2 - 4	4 - 8	8 - 15	15 - 25	25 - 35	
$M_{X\text{ref}}$ (GeV)	1.2	3	6	11	20	30	

Table 1: Binning and reference values for M_X , W and Q^2 .

Q^2 (GeV 2)	x	$F_2 \pm \text{stat.} \pm \text{syst.}$	Q^2 (GeV 2)	x	$F_2 \pm \text{stat.} \pm \text{syst.}$
2.7	0.001332	$0.574 \pm 0.017^{+0.044}_{-0.041}$	14.0	0.006869	$0.656 \pm 0.008^{+0.015}_{-0.017}$
2.7	0.000639	$0.668 \pm 0.022^{+0.046}_{-0.040}$	14.0	0.003303	$0.802 \pm 0.011^{+0.027}_{-0.031}$
2.7	0.000374	$0.706 \pm 0.021^{+0.038}_{-0.038}$	14.0	0.001934	$0.887 \pm 0.011^{+0.075}_{-0.065}$
2.7	0.000204	$0.747 \pm 0.019^{+0.047}_{-0.039}$	14.0	0.001058	$1.026 \pm 0.013^{+0.028}_{-0.034}$
2.7	0.000120	$0.827 \pm 0.023^{+0.045}_{-0.040}$	14.0	0.000622	$1.151 \pm 0.017^{+0.012}_{-0.015}$
2.7	0.000083	$0.888 \pm 0.024^{+0.041}_{-0.048}$	14.0	0.000432	$1.257 \pm 0.019^{+0.018}_{-0.023}$
2.7	0.000056	$0.965 \pm 0.028^{+0.042}_{-0.035}$	14.0	0.000289	$1.398 \pm 0.023^{+0.020}_{-0.033}$
4.0	0.001972	$0.624 \pm 0.009^{+0.036}_{-0.039}$	27.0	0.013160	$0.597 \pm 0.011^{+0.019}_{-0.024}$
4.0	0.000946	$0.700 \pm 0.012^{+0.042}_{-0.045}$	27.0	0.006351	$0.781 \pm 0.016^{+0.030}_{-0.029}$
4.0	0.000553	$0.775 \pm 0.012^{+0.070}_{-0.059}$	27.0	0.003724	$0.888 \pm 0.017^{+0.080}_{-0.072}$
4.0	0.000302	$0.843 \pm 0.013^{+0.043}_{-0.048}$	27.0	0.002038	$1.060 \pm 0.020^{+0.046}_{-0.046}$
4.0	0.000178	$0.913 \pm 0.016^{+0.047}_{-0.045}$	27.0	0.001199	$1.190 \pm 0.026^{+0.012}_{-0.023}$
4.0	0.000123	$1.018 \pm 0.017^{+0.042}_{-0.039}$	27.0	0.000833	$1.293 \pm 0.028^{+0.015}_{-0.005}$
4.0	0.000083	$1.091 \pm 0.018^{+0.041}_{-0.025}$	27.0	0.000557	$1.460 \pm 0.033^{+0.017}_{-0.026}$
6.0	0.002956	$0.633 \pm 0.011^{+0.030}_{-0.029}$	55.0	0.026450	$0.609 \pm 0.017^{+0.014}_{-0.011}$
6.0	0.001418	$0.743 \pm 0.014^{+0.044}_{-0.036}$	55.0	0.012850	$0.720 \pm 0.021^{+0.024}_{-0.027}$
6.0	0.000830	$0.820 \pm 0.014^{+0.053}_{-0.054}$	55.0	0.007556	$0.826 \pm 0.022^{+0.061}_{-0.048}$
6.0	0.000453	$0.910 \pm 0.015^{+0.033}_{-0.036}$	55.0	0.004142	$0.927 \pm 0.023^{+0.056}_{-0.048}$
6.0	0.000267	$1.021 \pm 0.019^{+0.029}_{-0.026}$	55.0	0.002439	$1.083 \pm 0.033^{+0.019}_{-0.017}$
6.0	0.000185	$1.100 \pm 0.019^{+0.024}_{-0.025}$	55.0	0.001695	$1.274 \pm 0.036^{+0.017}_{-0.020}$
6.0	0.000124	$1.231 \pm 0.023^{+0.025}_{-0.028}$	55.0	0.001135	$1.462 \pm 0.043^{+0.025}_{-0.024}$
8.0	0.003937	$0.665 \pm 0.011^{+0.010}_{-0.014}$			
8.0	0.001890	$0.771 \pm 0.013^{+0.024}_{-0.025}$			
8.0	0.001106	$0.868 \pm 0.014^{+0.070}_{-0.056}$			
8.0	0.000605	$0.959 \pm 0.015^{+0.017}_{-0.029}$			
8.0	0.000355	$1.085 \pm 0.020^{+0.016}_{-0.019}$			
8.0	0.000247	$1.196 \pm 0.020^{+0.025}_{-0.023}$			
8.0	0.000165	$1.305 \pm 0.025^{+0.025}_{-0.023}$			

Table 2: *Proton structure function F_2 .*

Q^2 (GeV 2)	$c \pm \text{stat.} \pm \text{syst.}$	$\alpha_{IP}^{\text{tot}}(0) \pm \text{stat.} \pm \text{syst.}$
2.7	$0.206 \pm 0.019^{+0.025}_{-0.017}$	$1.155 \pm 0.011^{+0.007}_{-0.011}$
4.0	$0.209 \pm 0.010^{+0.027}_{-0.028}$	$1.174 \pm 0.006^{+0.014}_{-0.012}$
6.0	$0.195 \pm 0.009^{+0.022}_{-0.019}$	$1.202 \pm 0.006^{+0.010}_{-0.011}$
8.0	$0.206 \pm 0.009^{+0.016}_{-0.015}$	$1.211 \pm 0.006^{+0.009}_{-0.009}$
14.0	$0.207 \pm 0.007^{+0.019}_{-0.017}$	$1.233 \pm 0.005^{+0.010}_{-0.011}$
27.0	$0.215 \pm 0.014^{+0.037}_{-0.029}$	$1.255 \pm 0.010^{+0.020}_{-0.021}$
55.0	$0.178 \pm 0.020^{+0.049}_{-0.028}$	$1.307 \pm 0.019^{+0.027}_{-0.037}$

Table 3: The results of the fits of F_2 data for $x < 0.01$ in bins of Q^2 to $F_2(x, Q^2) = c \cdot x^{-\lambda}$, where $\alpha_{IP}^{\text{tot}}(0) = 1 + \lambda$.

Q^2 (GeV 2)	W (GeV)	$\sigma_{\gamma^* p}^{\text{tot}} \pm \text{stat.} \pm \text{syst.}$ (μb)	Q^2 (GeV 2)	W (GeV)	$\sigma_{\gamma^* p}^{\text{tot}} \pm \text{stat.} \pm \text{syst.}$ (μb)
2.7	45.0	$23.88 \pm 0.70^{+1.82}_{-1.73}$	14.0	45.0	$5.29 \pm 0.07^{+0.12}_{-0.13}$
2.7	65.0	$27.75 \pm 0.93^{+1.92}_{-1.67}$	14.0	65.0	$6.45 \pm 0.09^{+0.22}_{-0.25}$
2.7	85.0	$29.33 \pm 0.89^{+1.58}_{-1.56}$	14.0	85.0	$7.12 \pm 0.09^{+0.60}_{-0.53}$
2.7	115.0	$31.03 \pm 0.80^{+1.95}_{-1.64}$	14.0	115.0	$8.23 \pm 0.10^{+0.22}_{-0.27}$
2.7	150.0	$34.38 \pm 0.97^{+1.86}_{-1.67}$	14.0	150.0	$9.23 \pm 0.14^{+0.09}_{-0.12}$
2.7	180.0	$36.91 \pm 1.01^{+1.69}_{-1.98}$	14.0	180.0	$10.08 \pm 0.15^{+0.14}_{-0.18}$
2.7	220.0	$40.09 \pm 1.18^{+1.73}_{-1.46}$	14.0	220.0	$11.20 \pm 0.18^{+0.16}_{-0.26}$
4.0	45.0	$17.53 \pm 0.26^{+1.01}_{-1.11}$	27.0	45.0	$2.51 \pm 0.05^{+0.08}_{-0.10}$
4.0	65.0	$19.66 \pm 0.33^{+1.18}_{-1.27}$	27.0	65.0	$3.26 \pm 0.07^{+0.13}_{-0.12}$
4.0	85.0	$21.73 \pm 0.35^{+1.97}_{-1.65}$	27.0	85.0	$3.70 \pm 0.07^{+0.33}_{-0.30}$
4.0	115.0	$23.64 \pm 0.36^{+1.20}_{-1.34}$	27.0	115.0	$4.41 \pm 0.08^{+0.19}_{-0.19}$
4.0	150.0	$25.61 \pm 0.44^{+1.32}_{-1.27}$	27.0	150.0	$4.95 \pm 0.11^{+0.05}_{-0.10}$
4.0	180.0	$28.55 \pm 0.46^{+1.17}_{-1.10}$	27.0	180.0	$5.38 \pm 0.12^{+0.06}_{-0.02}$
4.0	220.0	$30.60 \pm 0.52^{+1.14}_{-0.71}$	27.0	220.0	$6.07 \pm 0.14^{+0.07}_{-0.11}$
6.0	45.0	$11.88 \pm 0.20^{+0.56}_{-0.55}$	55.0	45.0	$1.28 \pm 0.04^{+0.03}_{-0.02}$
6.0	65.0	$13.91 \pm 0.26^{+0.82}_{-0.68}$	55.0	65.0	$1.49 \pm 0.04^{+0.05}_{-0.06}$
6.0	85.0	$15.34 \pm 0.27^{+0.99}_{-1.01}$	55.0	85.0	$1.70 \pm 0.05^{+0.13}_{-0.10}$
6.0	115.0	$17.02 \pm 0.28^{+0.62}_{-0.67}$	55.0	115.0	$1.90 \pm 0.05^{+0.11}_{-0.10}$
6.0	150.0	$19.09 \pm 0.35^{+0.54}_{-0.49}$	55.0	150.0	$2.21 \pm 0.07^{+0.04}_{-0.03}$
6.0	180.0	$20.57 \pm 0.36^{+0.45}_{-0.47}$	55.0	180.0	$2.60 \pm 0.07^{+0.03}_{-0.04}$
6.0	220.0	$23.02 \pm 0.44^{+0.47}_{-0.52}$	55.0	220.0	$2.99 \pm 0.09^{+0.05}_{-0.05}$
8.0	45.0	$9.36 \pm 0.15^{+0.15}_{-0.20}$			
8.0	65.0	$10.84 \pm 0.19^{+0.33}_{-0.36}$			
8.0	85.0	$12.19 \pm 0.20^{+0.98}_{-0.79}$			
8.0	115.0	$13.45 \pm 0.21^{+0.24}_{-0.41}$			
8.0	150.0	$15.22 \pm 0.28^{+0.22}_{-0.26}$			
8.0	180.0	$16.77 \pm 0.29^{+0.35}_{-0.32}$			
8.0	220.0	$18.30 \pm 0.35^{+0.35}_{-0.32}$			

Table 4: Total $\gamma^* p$ cross section $\sigma_{\gamma^* p}^{\text{tot}}$.

M_X (GeV)	Q^2 (GeV 2)	W (GeV)	$\frac{d\sigma_{\gamma^* p \rightarrow XN}^{\text{diff}}}{dM_X}$	\pm stat. \pm syst.	M_X (GeV)	Q^2 (GeV 2)	W (GeV)	$\frac{d\sigma_{\gamma^* p \rightarrow XN}^{\text{diff}}}{dM_X}$	\pm stat. \pm syst.
			(nb/GeV)					(nb/GeV)	
1.2	2.7	45.0	$773.8 \pm 76.0^{+109.5}_{-79.8}$		1.2	14.0	45.0	$31.6 \pm 2.3^{+4.3}_{-3.6}$	
1.2	2.7	65.0	$908.4 \pm 89.8^{+141.2}_{-112.6}$		1.2	14.0	65.0	$30.4 \pm 2.4^{+3.9}_{-4.5}$	
1.2	2.7	85.0	$952.8 \pm 89.0^{+85.3}_{-79.8}$		1.2	14.0	85.0	$40.3 \pm 2.7^{+5.6}_{-6.9}$	
1.2	2.7	115.0	$958.2 \pm 73.7^{+99.7}_{-86.0}$		1.2	14.0	115.0	$39.0 \pm 2.8^{+4.1}_{-3.4}$	
1.2	2.7	150.0	$1010.0 \pm 86.6^{+113.0}_{-115.7}$		1.2	14.0	150.0	$41.9 \pm 3.5^{+3.3}_{-4.7}$	
1.2	2.7	180.0	$872.3 \pm 85.1^{+145.2}_{-87.9}$		1.2	14.0	180.0	$30.8 \pm 3.0^{+3.6}_{-3.4}$	
					1.2	14.0	220.0	$52.9 \pm 5.0^{+6.0}_{-5.5}$	
1.2	4.0	45.0	$388.4 \pm 22.7^{+39.9}_{-54.2}$		1.2	27.0	45.0	$6.3 \pm 1.0^{+0.5}_{-1.2}$	
1.2	4.0	65.0	$423.0 \pm 27.4^{+56.6}_{-63.0}$		1.2	27.0	65.0	$5.4 \pm 1.1^{+1.0}_{-0.6}$	
1.2	4.0	85.0	$485.4 \pm 31.0^{+69.4}_{-64.8}$		1.2	27.0	85.0	$8.8 \pm 1.3^{+1.4}_{-1.6}$	
1.2	4.0	115.0	$564.2 \pm 32.1^{+60.3}_{-56.1}$		1.2	27.0	115.0	$4.7 \pm 1.1^{+0.9}_{-0.9}$	
1.2	4.0	150.0	$481.7 \pm 33.9^{+64.4}_{-48.5}$		1.2	27.0	150.0	$12.0 \pm 2.2^{+0.9}_{-3.8}$	
1.2	4.0	180.0	$603.7 \pm 40.4^{+53.4}_{-63.2}$		1.2	27.0	180.0	$7.9 \pm 1.8^{+1.4}_{-1.6}$	
1.2	4.0	220.0	$471.1 \pm 48.9^{+141.3}_{-72.5}$		1.2	27.0	220.0	$9.6 \pm 2.0^{+2.0}_{-1.0}$	
1.2	6.0	45.0	$164.0 \pm 14.0^{+17.4}_{-20.9}$		1.2	55.0	45.0	$1.1 \pm 0.4^{+0.3}_{-0.4}$	
1.2	6.0	65.0	$192.5 \pm 17.7^{+43.4}_{-19.7}$		1.2	55.0	65.0	$1.3 \pm 0.6^{+0.2}_{-0.2}$	
1.2	6.0	85.0	$193.6 \pm 17.7^{+21.8}_{-22.5}$		1.2	55.0	85.0	$0.5 \pm 0.3^{+0.5}_{-0.1}$	
1.2	6.0	115.0	$211.2 \pm 17.4^{+20.2}_{-28.8}$		1.2	55.0	115.0	$1.2 \pm 0.4^{+0.1}_{-0.2}$	
1.2	6.0	150.0	$256.2 \pm 22.6^{+27.6}_{-24.8}$		1.2	55.0	150.0	$1.5 \pm 0.9^{+1.0}_{-0.3}$	
1.2	6.0	180.0	$223.6 \pm 20.7^{+31.2}_{-19.5}$		1.2	55.0	220.0	$1.4 \pm 0.7^{+0.2}_{-0.9}$	
1.2	6.0	220.0	$254.3 \pm 27.7^{+46.8}_{-47.6}$						
1.2	8.0	45.0	$106.0 \pm 8.2^{+11.1}_{-12.2}$						
1.2	8.0	65.0	$120.5 \pm 8.7^{+16.8}_{-15.4}$						
1.2	8.0	85.0	$125.7 \pm 9.3^{+19.6}_{-15.3}$						
1.2	8.0	115.0	$142.7 \pm 10.3^{+15.2}_{-14.2}$						
1.2	8.0	150.0	$151.7 \pm 12.6^{+12.9}_{-13.1}$						
1.2	8.0	180.0	$174.2 \pm 13.4^{+12.6}_{-24.0}$						
1.2	8.0	220.0	$141.2 \pm 14.2^{+27.2}_{-15.5}$						

Table 5: Cross section for diffractive scattering, $\gamma^* p \rightarrow XN$, $M_N < 2.3$ GeV, for $M_X = 1.2$ GeV in bins of W and Q^2 .

M_X	Q^2	W	$\frac{d\sigma_{\gamma^* p \rightarrow X N}^{\text{diff}}}{dM_X}$	M_X	Q^2	W	$\frac{d\sigma_{\gamma^* p \rightarrow X N}^{\text{diff}}}{dM_X}$
			\pm stat. \pm syst.				\pm stat. \pm syst.
(GeV)	(GeV 2)	(GeV)	(nb/GeV)	(GeV)	(GeV 2)	(GeV)	(nb/GeV)
3.0	2.7	45.0	$502.7 \pm 50.8^{+52.8}_{-50.1}$	3.0	14.0	45.0	$61.0 \pm 3.5^{+2.8}_{-4.2}$
3.0	2.7	65.0	$476.5 \pm 57.8^{+30.7}_{-38.4}$	3.0	14.0	65.0	$67.3 \pm 3.8^{+7.4}_{-5.0}$
3.0	2.7	85.0	$501.7 \pm 58.9^{+63.1}_{-38.2}$	3.0	14.0	85.0	$80.2 \pm 4.2^{+13.2}_{-9.1}$
3.0	2.7	115.0	$555.6 \pm 58.0^{+45.3}_{-44.8}$	3.0	14.0	115.0	$88.0 \pm 4.5^{+2.3}_{-5.7}$
3.0	2.7	150.0	$772.0 \pm 72.4^{+40.4}_{-59.4}$	3.0	14.0	150.0	$88.8 \pm 5.6^{+7.3}_{-3.6}$
3.0	2.7	180.0	$802.8 \pm 68.8^{+81.8}_{-76.6}$	3.0	14.0	180.0	$103.6 \pm 6.2^{+11.3}_{-9.4}$
				3.0	14.0	220.0	$114.1 \pm 7.4^{+9.9}_{-7.9}$
3.0	4.0	45.0	$332.2 \pm 20.5^{+29.0}_{-16.3}$	3.0	27.0	45.0	$10.4 \pm 1.4^{+1.6}_{-1.2}$
3.0	4.0	65.0	$363.4 \pm 24.8^{+35.8}_{-39.2}$	3.0	27.0	65.0	$16.4 \pm 1.9^{+4.2}_{-2.2}$
3.0	4.0	85.0	$372.9 \pm 26.1^{+30.8}_{-37.7}$	3.0	27.0	85.0	$19.8 \pm 2.0^{+3.3}_{-3.8}$
3.0	4.0	115.0	$411.0 \pm 27.8^{+24.5}_{-28.5}$	3.0	27.0	115.0	$23.4 \pm 2.2^{+2.3}_{-2.1}$
3.0	4.0	150.0	$502.6 \pm 34.6^{+50.4}_{-30.3}$	3.0	27.0	150.0	$28.0 \pm 3.1^{+2.5}_{-3.4}$
3.0	4.0	180.0	$619.8 \pm 37.2^{+37.3}_{-39.5}$	3.0	27.0	180.0	$28.5 \pm 3.3^{+4.5}_{-2.1}$
3.0	4.0	220.0	$574.4 \pm 37.8^{+47.3}_{-47.3}$	3.0	27.0	220.0	$34.4 \pm 3.4^{+3.8}_{-4.0}$
3.0	6.0	45.0	$228.1 \pm 16.5^{+19.6}_{-25.9}$				
3.0	6.0	65.0	$249.4 \pm 20.4^{+24.9}_{-10.6}$	3.0	55.0	65.0	$2.5 \pm 0.7^{+0.5}_{-0.1}$
3.0	6.0	85.0	$297.6 \pm 24.0^{+22.7}_{-22.6}$	3.0	55.0	85.0	$4.0 \pm 0.8^{+0.3}_{-0.5}$
3.0	6.0	115.0	$276.5 \pm 20.0^{+12.0}_{-11.4}$	3.0	55.0	115.0	$4.0 \pm 0.9^{+0.9}_{-0.4}$
3.0	6.0	150.0	$389.4 \pm 29.5^{+10.1}_{-20.5}$	3.0	55.0	150.0	$4.1 \pm 1.1^{+1.5}_{-0.8}$
3.0	6.0	180.0	$423.0 \pm 30.5^{+21.0}_{-26.0}$	3.0	55.0	180.0	$6.0 \pm 1.2^{+0.6}_{-1.5}$
3.0	6.0	220.0	$389.1 \pm 30.7^{+18.0}_{-26.5}$	3.0	55.0	220.0	$6.6 \pm 1.4^{+1.5}_{-1.0}$
3.0	8.0	45.0	$160.4 \pm 9.8^{+3.4}_{-5.2}$				
3.0	8.0	65.0	$180.1 \pm 11.5^{+12.1}_{-22.2}$				
3.0	8.0	85.0	$205.8 \pm 12.5^{+25.1}_{-13.1}$				
3.0	8.0	115.0	$205.0 \pm 12.1^{+6.3}_{-8.2}$				
3.0	8.0	150.0	$246.4 \pm 16.0^{+17.6}_{-17.2}$				
3.0	8.0	180.0	$228.0 \pm 15.0^{+19.4}_{-6.4}$				
3.0	8.0	220.0	$265.3 \pm 17.5^{+19.2}_{-16.1}$				

Table 6: Cross section for diffractive scattering, $\gamma^* p \rightarrow X N$, $M_N < 2.3$ GeV, for $M_X = 3.0$ GeV in bins of W and Q^2 .

M_X	Q^2	W	$\frac{d\sigma_{\gamma^* p \rightarrow X N}^{\text{diff}}}{dM_X}$	M_X	Q^2	W	$\frac{d\sigma_{\gamma^* p \rightarrow X N}^{\text{diff}}}{dM_X}$
(GeV)	(GeV 2)	(GeV)	(nb/GeV)	(GeV)	(GeV 2)	(GeV)	(nb/GeV)
6.0	2.7	65.0	$221.5 \pm 26.2^{+11.1}_{-11.5}$	6.0	14.0	65.0	$45.6 \pm 3.3^{+4.8}_{-4.8}$
6.0	2.7	85.0	$262.7 \pm 28.4^{+17.5}_{-13.3}$	6.0	14.0	85.0	$55.9 \pm 2.8^{+7.1}_{-5.5}$
6.0	2.7	115.0	$278.8 \pm 27.8^{+35.3}_{-26.6}$	6.0	14.0	115.0	$57.3 \pm 2.8^{+0.9}_{-5.4}$
6.0	2.7	150.0	$270.8 \pm 30.3^{+23.5}_{-30.4}$	6.0	14.0	150.0	$64.9 \pm 3.6^{+2.9}_{-1.8}$
6.0	2.7	180.0	$313.3 \pm 30.1^{+24.0}_{-29.9}$	6.0	14.0	180.0	$73.8 \pm 3.9^{+2.3}_{-2.0}$
				6.0	14.0	220.0	$73.9 \pm 4.2^{+4.5}_{-3.0}$
6.0	4.0	45.0	$151.5 \pm 24.6^{+16.8}_{-11.3}$				
6.0	4.0	65.0	$155.3 \pm 13.0^{+16.5}_{-13.4}$	6.0	27.0	65.0	$19.1 \pm 2.1^{+1.4}_{-2.1}$
6.0	4.0	85.0	$182.8 \pm 13.6^{+28.1}_{-18.1}$	6.0	27.0	85.0	$24.2 \pm 1.8^{+2.8}_{-3.3}$
6.0	4.0	115.0	$182.1 \pm 13.3^{+9.6}_{-16.5}$	6.0	27.0	115.0	$27.3 \pm 2.1^{+1.6}_{-3.3}$
6.0	4.0	150.0	$217.5 \pm 16.7^{+10.4}_{-18.1}$	6.0	27.0	150.0	$28.7 \pm 2.5^{+0.8}_{-1.0}$
6.0	4.0	180.0	$239.1 \pm 16.4^{+17.6}_{-12.0}$	6.0	27.0	180.0	$34.8 \pm 2.9^{+0.5}_{-2.2}$
6.0	4.0	220.0	$265.0 \pm 17.0^{+11.9}_{-23.8}$	6.0	27.0	220.0	$40.8 \pm 3.0^{+1.2}_{-2.7}$
6.0	6.0	45.0	$93.1 \pm 17.4^{+13.4}_{-12.2}$				
6.0	6.0	65.0	$124.3 \pm 11.7^{+9.3}_{-10.5}$	6.0	55.0	65.0	$4.2 \pm 1.0^{+0.7}_{-0.5}$
6.0	6.0	85.0	$129.5 \pm 10.9^{+3.4}_{-12.3}$	6.0	55.0	85.0	$5.9 \pm 0.9^{+1.7}_{-0.9}$
6.0	6.0	115.0	$125.5 \pm 10.0^{+6.3}_{-2.9}$	6.0	55.0	115.0	$8.0 \pm 0.9^{+0.4}_{-1.1}$
6.0	6.0	150.0	$166.2 \pm 13.4^{+10.8}_{-11.4}$	6.0	55.0	150.0	$6.7 \pm 1.1^{+1.8}_{-0.8}$
6.0	6.0	180.0	$160.5 \pm 12.0^{+8.1}_{-10.5}$	6.0	55.0	180.0	$12.4 \pm 1.4^{+0.4}_{-1.4}$
6.0	6.0	220.0	$190.2 \pm 13.5^{+10.7}_{-4.7}$	6.0	55.0	220.0	$10.4 \pm 1.4^{+0.7}_{-0.9}$
6.0	8.0	45.0	$78.0 \pm 14.4^{+7.4}_{-5.5}$				
6.0	8.0	65.0	$85.8 \pm 6.9^{+6.3}_{-5.8}$				
6.0	8.0	85.0	$98.9 \pm 6.2^{+12.1}_{-7.6}$				
6.0	8.0	115.0	$108.3 \pm 6.4^{+2.3}_{-4.8}$				
6.0	8.0	150.0	$106.5 \pm 7.3^{+5.5}_{-6.2}$				
6.0	8.0	180.0	$128.0 \pm 7.9^{+8.9}_{-7.1}$				
6.0	8.0	220.0	$141.2 \pm 8.8^{+4.5}_{-7.7}$				

Table 7: Cross section for diffractive scattering, $\gamma^* p \rightarrow X N$, $M_N < 2.3$ GeV, for $M_X = 6.0$ GeV in bins of W and Q^2 .

M_X (GeV)	Q^2 (GeV 2)	W (GeV)	$\frac{d\sigma_{\gamma^* p \rightarrow XN}^{\text{diff}}}{dM_X}$		M_X (GeV)	Q^2 (GeV 2)	W (GeV)	$\frac{d\sigma_{\gamma^* p \rightarrow XN}^{\text{diff}}}{dM_X}$	
			\pm stat.	\pm syst.				\pm stat.	\pm syst.
11.0	2.7	85.0	126.3	$\pm 27.1^{+24.3}_{-8.3}$	11.0	14.0	85.0	30.5	$\pm 5.7^{+5.5}_{-4.9}$
11.0	2.7	115.0	141.3	$\pm 17.1^{+14.0}_{-12.3}$	11.0	14.0	115.0	32.0	$\pm 2.8^{+1.2}_{-2.5}$
11.0	2.7	150.0	124.7	$\pm 16.5^{+15.3}_{-8.3}$	11.0	14.0	150.0	34.2	$\pm 2.4^{+0.6}_{-1.4}$
11.0	2.7	180.0	148.7	$\pm 15.4^{+4.5}_{-17.9}$	11.0	14.0	180.0	37.7	$\pm 2.3^{+2.0}_{-1.6}$
11.0	2.7	220.0	151.4	$\pm 16.4^{+19.4}_{-3.4}$	11.0	14.0	220.0	43.1	$\pm 2.7^{+1.5}_{-1.0}$
11.0	4.0	85.0	70.7	$\pm 16.8^{+11.1}_{-11.4}$	11.0	27.0	85.0	11.9	$\pm 3.2^{+3.1}_{-1.5}$
11.0	4.0	115.0	92.5	$\pm 10.4^{+8.2}_{-6.0}$	11.0	27.0	115.0	12.6	$\pm 1.8^{+1.8}_{-0.4}$
11.0	4.0	150.0	104.1	$\pm 9.1^{+5.0}_{-10.8}$	11.0	27.0	150.0	14.0	$\pm 1.6^{+0.9}_{-0.9}$
11.0	4.0	180.0	98.3	$\pm 7.7^{+7.5}_{-4.0}$	11.0	27.0	180.0	15.6	$\pm 1.6^{+1.7}_{-0.8}$
11.0	4.0	220.0	106.9	$\pm 8.1^{+4.1}_{-7.4}$	11.0	27.0	220.0	22.4	$\pm 1.7^{+0.6}_{-1.8}$
11.0	6.0	85.0	51.9	$\pm 12.8^{+12.9}_{-6.0}$					
11.0	6.0	115.0	72.2	$\pm 7.4^{+1.2}_{-8.1}$	11.0	55.0	115.0	7.2	$\pm 1.0^{+0.4}_{-0.7}$
11.0	6.0	150.0	68.0	$\pm 6.8^{+4.4}_{-3.7}$	11.0	55.0	150.0	7.1	$\pm 1.0^{+0.8}_{-0.6}$
11.0	6.0	180.0	79.1	$\pm 6.8^{+3.0}_{-4.3}$	11.0	55.0	180.0	8.8	$\pm 1.0^{+0.8}_{-0.1}$
11.0	6.0	220.0	97.9	$\pm 7.8^{+2.9}_{-3.9}$	11.0	55.0	220.0	10.1	$\pm 1.2^{+0.4}_{-0.6}$
11.0	8.0	85.0	49.2	$\pm 9.9^{+4.5}_{-8.8}$					
11.0	8.0	115.0	60.9	$\pm 5.4^{+3.4}_{-1.2}$					
11.0	8.0	150.0	58.2	$\pm 4.7^{+2.6}_{-0.3}$					
11.0	8.0	180.0	61.7	$\pm 4.6^{+1.1}_{-3.2}$					
11.0	8.0	220.0	69.6	$\pm 5.0^{+5.3}_{-1.1}$					

Table 8: Cross section for diffractive scattering, $\gamma^* p \rightarrow XN$, $M_N < 2.3$ GeV, for $M_X = 11.0$ GeV in bins of W and Q^2 .

M_X	Q^2	W	$\frac{d\sigma^{\text{diff}}}{dM_X} \gamma^* p \rightarrow XN$	M_X	Q^2	W	$\frac{d\sigma^{\text{diff}}}{dM_X} \gamma^* p \rightarrow XN$
(GeV)	(GeV 2)	(GeV)	(nb/GeV)	(GeV)	(GeV 2)	(GeV)	(nb/GeV)
20.0	2.7	150.0	$81.8 \pm 24.0^{+8.6}_{-4.4}$	20.0	14.0	150.0	$17.8 \pm 4.9^{+2.3}_{-1.9}$
20.0	2.7	180.0	$68.1 \pm 13.3^{+8.3}_{-3.1}$	20.0	14.0	180.0	$21.1 \pm 3.1^{+0.8}_{-1.2}$
20.0	2.7	220.0	$107.1 \pm 13.4^{+8.8}_{-6.7}$	20.0	14.0	220.0	$23.9 \pm 2.3^{+1.0}_{-0.9}$
20.0	4.0	150.0	$48.0 \pm 15.2^{+3.7}_{-4.7}$				
20.0	4.0	180.0	$57.1 \pm 9.3^{+4.8}_{-3.5}$	20.0	27.0	180.0	$10.2 \pm 1.9^{+0.5}_{-0.7}$
20.0	4.0	220.0	$66.9 \pm 6.9^{+3.8}_{-2.6}$	20.0	27.0	220.0	$10.7 \pm 1.4^{+1.0}_{-0.4}$
20.0	6.0	150.0	$40.9 \pm 11.1^{+5.2}_{-4.0}$	20.0	55.0	150.0	$4.2 \pm 1.4^{+0.9}_{-1.0}$
20.0	6.0	180.0	$42.5 \pm 7.0^{+0.7}_{-6.0}$	20.0	55.0	180.0	$3.7 \pm 1.0^{+0.4}_{-0.5}$
20.0	6.0	220.0	$48.0 \pm 5.2^{+3.2}_{-4.2}$	20.0	55.0	220.0	$4.7 \pm 0.9^{+1.1}_{-0.3}$
20.0	8.0	150.0	$31.3 \pm 8.2^{+2.6}_{-2.5}$				
20.0	8.0	180.0	$41.1 \pm 5.5^{+0.9}_{-4.3}$				
20.0	8.0	220.0	$39.6 \pm 4.2^{+1.4}_{-4.7}$				

Table 9: Cross section for diffractive scattering, $\gamma^* p \rightarrow XN$, $M_N < 2.3$ GeV, for $M_X = 20.0$ GeV in bins of W and Q^2 .

M_X	Q^2	W	$\frac{d\sigma^{\text{diff}}}{dM_X} \gamma^* p \rightarrow XN$	M_X	Q^2	W	$\frac{d\sigma^{\text{diff}}}{dM_X} \gamma^* p \rightarrow XN$
(GeV)	(GeV 2)	(GeV)	(nb/GeV)	(GeV)	(GeV 2)	(GeV)	(nb/GeV)
30.0	2.7	220.0	$63.3 \pm 18.6^{+9.2}_{-6.1}$	30.0	14.0	220.0	$16.9 \pm 4.5^{+1.7}_{-1.1}$
30.0	4.0	220.0	$41.3 \pm 11.8^{+1.5}_{-5.0}$	30.0	27.0	220.0	$6.8 \pm 2.4^{+0.7}_{-0.8}$
30.0	6.0	220.0	$29.3 \pm 8.8^{+4.5}_{-3.4}$				
30.0	8.0	220.0	$23.2 \pm 7.4^{+4.6}_{-1.1}$				

Table 10: Cross section for diffractive scattering, $\gamma^* p \rightarrow XN$, $M_N < 2.3$ GeV, for $M_X = 30.0$ GeV in bins of W and Q^2 .

M_X (GeV)	Q^2 (GeV 2)	$\alpha_{\overline{I}P}^{\text{diff}}(0) \pm \text{stat.} \pm \text{syst.}$
1.2	2.7	$1.058 \pm 0.019^{+0.017}_{-0.018}$
	4.0	$1.085 \pm 0.012^{+0.024}_{-0.014}$
	6.0	$1.095 \pm 0.016^{+0.015}_{-0.012}$
	8.0	$1.095 \pm 0.014^{+0.015}_{-0.013}$
	14.0	$1.074 \pm 0.015^{+0.016}_{-0.011}$
	27.0	$1.095 \pm 0.038^{+0.024}_{-0.014}$
	55.0	$1.087 \pm 0.113^{+0.042}_{-0.080}$
3.0	2.7	$1.130 \pm 0.024^{+0.021}_{-0.010}$
	4.0	$1.130 \pm 0.012^{+0.015}_{-0.016}$
	6.0	$1.128 \pm 0.014^{+0.013}_{-0.015}$
	8.0	$1.103 \pm 0.011^{+0.012}_{-0.005}$
	14.0	$1.125 \pm 0.011^{+0.015}_{-0.013}$
	27.0	$1.201 \pm 0.019^{+0.017}_{-0.018}$
	55.0	$1.202 \pm 0.057^{+0.013}_{-0.030}$
6.0	2.7	$1.099 \pm 0.032^{+0.008}_{-0.021}$
	4.0	$1.131 \pm 0.017^{+0.015}_{-0.020}$
	6.0	$1.126 \pm 0.019^{+0.017}_{-0.010}$
	8.0	$1.121 \pm 0.016^{+0.015}_{-0.015}$
	14.0	$1.125 \pm 0.014^{+0.026}_{-0.021}$
	27.0	$1.170 \pm 0.021^{+0.020}_{-0.019}$
	55.0	$1.208 \pm 0.038^{+0.022}_{-0.024}$
11.0	2.7	$1.074 \pm 0.049^{+0.019}_{-0.033}$
	4.0	$1.098 \pm 0.041^{+0.019}_{-0.023}$
	6.0	$1.170 \pm 0.046^{+0.022}_{-0.023}$
	8.0	$1.097 \pm 0.038^{+0.026}_{-0.020}$
	14.0	$1.138 \pm 0.036^{+0.030}_{-0.012}$
	27.0	$1.248 \pm 0.058^{+0.023}_{-0.066}$
	55.0	$1.181 \pm 0.070^{+0.021}_{-0.022}$

Table 11: The value of $\alpha_{\overline{I}P}^{\text{diff}}(0)$ for M_X and Q^2 bins.

Q^2 range (GeV 2)	$<Q^2>$ (GeV 2)	$\alpha_{IP}^{\text{diff}}(0) \pm \text{stat.} \pm \text{syst.}$
2.2 - 5	3.6	$1.125 \pm 0.009^{+0.013}_{-0.013}$
5 - 10	7.2	$1.117 \pm 0.007^{+0.013}_{-0.010}$
10 - 20	14.0	$1.126 \pm 0.009^{+0.016}_{-0.013}$
2.2 - 20	8.3	$1.122 \pm 0.005^{+0.013}_{-0.011}$
20 - 80	34.4	$1.193 \pm 0.013^{+0.016}_{-0.019}$

Table 12: The values of $\alpha_{IP}^{\text{diff}}(0)$ for $2 < M_X < 15$ GeV.

Q^2 range (GeV 2)	$<Q^2>$ (GeV 2)	$\alpha_{IP}^{\text{diff}}(0) \pm \text{stat.} \pm \text{syst.}$
2.2 - 5	3.6	$1.127 \pm 0.009^{+0.013}_{-0.013}$
5 - 10	7.2	$1.115 \pm 0.008^{+0.013}_{-0.010}$
10 - 20	14.0	$1.124 \pm 0.012^{+0.020}_{-0.019}$
2.2 - 20	8.3	$1.121 \pm 0.005^{+0.014}_{-0.012}$
20 - 80	33.9	$1.179 \pm 0.017^{+0.020}_{-0.022}$

Table 13: The values of $\alpha_{IP}^{\text{diff}}(0)$ for $2 < M_X < 15$ GeV and $x_{IP} < 0.01$.

Q^2	W	$\frac{\int_{M_a}^{M_b} dM_X d\sigma_{\gamma^* p \rightarrow XN}^{\text{diff}}}{\sigma^{\text{tot}}} / dM_X$	Q^2	W	$\frac{\int_{M_a}^{M_b} dM_X d\sigma_{\gamma^* p \rightarrow XN}^{\text{diff}}}{\sigma^{\text{tot}}} / dM_X$
(GeV 2)	(GeV)	$\pm \text{stat.} \pm \text{syst.}$	(GeV 2)	(GeV)	$\pm \text{stat.} \pm \text{syst.}$
2.7	45	$0.0557 \pm 0.0057^{+0.0079}_{-0.0057}$	14.0	45	$0.0103 \pm 0.0008^{+0.0014}_{-0.0012}$
2.7	65	$0.0563 \pm 0.0059^{+0.0088}_{-0.0070}$	14.0	65	$0.0081 \pm 0.0006^{+0.0010}_{-0.0012}$
2.7	85	$0.0559 \pm 0.0055^{+0.0050}_{-0.0047}$	14.0	85	$0.0097 \pm 0.0007^{+0.0014}_{-0.0017}$
2.7	115	$0.0531 \pm 0.0043^{+0.0055}_{-0.0048}$	14.0	115	$0.0081 \pm 0.0006^{+0.0009}_{-0.0007}$
2.7	150	$0.0505 \pm 0.0046^{+0.0057}_{-0.0058}$	14.0	150	$0.0078 \pm 0.0007^{+0.0006}_{-0.0009}$
2.7	180	$0.0406 \pm 0.0041^{+0.0068}_{-0.0041}$	14.0	180	$0.0053 \pm 0.0005^{+0.0006}_{-0.0006}$
			14.0	220	$0.0081 \pm 0.0008^{+0.0009}_{-0.0008}$
4.0	45	$0.0381 \pm 0.0023^{+0.0039}_{-0.0053}$	27.0	45	$0.0043 \pm 0.0007^{+0.0004}_{-0.0008}$
4.0	65	$0.0370 \pm 0.0025^{+0.0050}_{-0.0055}$	27.0	65	$0.0028 \pm 0.0006^{+0.0005}_{-0.0003}$
4.0	85	$0.0384 \pm 0.0025^{+0.0055}_{-0.0051}$	27.0	85	$0.0041 \pm 0.0006^{+0.0006}_{-0.0007}$
4.0	115	$0.0410 \pm 0.0024^{+0.0044}_{-0.0041}$	27.0	115	$0.0018 \pm 0.0004^{+0.0004}_{-0.0003}$
4.0	150	$0.0323 \pm 0.0023^{+0.0043}_{-0.0033}$	27.0	150	$0.0042 \pm 0.0008^{+0.0003}_{-0.0013}$
4.0	180	$0.0364 \pm 0.0025^{+0.0032}_{-0.0038}$	27.0	180	$0.0025 \pm 0.0006^{+0.0005}_{-0.0005}$
4.0	220	$0.0265 \pm 0.0028^{+0.0079}_{-0.0041}$	27.0	220	$0.0027 \pm 0.0006^{+0.0006}_{-0.0003}$
6.0	45	$0.0238 \pm 0.0021^{+0.0025}_{-0.0030}$	55.0	45	$0.0014 \pm 0.0005^{+0.0005}_{-0.0005}$
6.0	65	$0.0238 \pm 0.0022^{+0.0054}_{-0.0024}$	55.0	65	$0.0015 \pm 0.0007^{+0.0003}_{-0.0003}$
6.0	85	$0.0217 \pm 0.0020^{+0.0024}_{-0.0025}$	55.0	85	$0.0005 \pm 0.0003^{+0.0005}_{-0.0001}$
6.0	115	$0.0213 \pm 0.0018^{+0.0020}_{-0.0029}$	55.0	115	$0.0011 \pm 0.0004^{+0.0001}_{-0.0002}$
6.0	150	$0.0231 \pm 0.0021^{+0.0025}_{-0.0022}$	55.0	150	$0.0012 \pm 0.0007^{+0.0008}_{-0.0002}$
6.0	180	$0.0187 \pm 0.0018^{+0.0026}_{-0.0016}$			
6.0	220	$0.0190 \pm 0.0021^{+0.0035}_{-0.0036}$	55.0	220	$0.0008 \pm 0.0004^{+0.0001}_{-0.0005}$
8.0	45	$0.0195 \pm 0.0015^{+0.0020}_{-0.0022}$			
8.0	65	$0.0191 \pm 0.0014^{+0.0027}_{-0.0025}$			
8.0	85	$0.0177 \pm 0.0013^{+0.0028}_{-0.0022}$			
8.0	115	$0.0183 \pm 0.0013^{+0.0019}_{-0.0018}$			
8.0	150	$0.0171 \pm 0.0015^{+0.0015}_{-0.0015}$			
8.0	180	$0.0179 \pm 0.0014^{+0.0013}_{-0.0025}$			
8.0	220	$0.0133 \pm 0.0014^{+0.0026}_{-0.0015}$			

Table 14: Ratio of the cross section for diffractive scattering, $\gamma^* p \rightarrow XN$, $M_N < 2.3$ GeV, integrated over $M_X = 0.28 - 2$ GeV, to the total cross section.

Q^2	W	$\frac{\int_{M_a}^{M_b} dM_X d\sigma_{\gamma^* p \rightarrow X N}^{\text{diff}} / dM_X}{\sigma^{\text{tot}}}$	Q^2	W	$\frac{\int_{M_a}^{M_b} dM_X d\sigma_{\gamma^* p \rightarrow X N}^{\text{diff}} / dM_X}{\sigma^{\text{tot}}}$
(GeV 2)	(GeV)	$\pm \text{stat.} \pm \text{syst.}$	(GeV 2)	(GeV)	$\pm \text{stat.} \pm \text{syst.}$
2.7	45	$0.0421 \pm 0.0044^{+0.0044}_{-0.0042}$	14.0	45	$0.0230 \pm 0.0014^{+0.0011}_{-0.0016}$
2.7	65	$0.0343 \pm 0.0043^{+0.0022}_{-0.0028}$	14.0	65	$0.0209 \pm 0.0012^{+0.0023}_{-0.0015}$
2.7	85	$0.0342 \pm 0.0042^{+0.0043}_{-0.0026}$	14.0	85	$0.0225 \pm 0.0012^{+0.0037}_{-0.0026}$
2.7	115	$0.0358 \pm 0.0039^{+0.0029}_{-0.0029}$	14.0	115	$0.0214 \pm 0.0011^{+0.0006}_{-0.0014}$
2.7	150	$0.0449 \pm 0.0044^{+0.0023}_{-0.0035}$	14.0	150	$0.0192 \pm 0.0012^{+0.0016}_{-0.0008}$
2.7	180	$0.0435 \pm 0.0039^{+0.0044}_{-0.0042}$	14.0	180	$0.0205 \pm 0.0013^{+0.0022}_{-0.0019}$
			14.0	220	$0.0204 \pm 0.0014^{+0.0018}_{-0.0014}$
4.0	45	$0.0379 \pm 0.0024^{+0.0033}_{-0.0019}$	27.0	45	$0.0083 \pm 0.0011^{+0.0013}_{-0.0010}$
4.0	65	$0.0370 \pm 0.0026^{+0.0036}_{-0.0040}$	27.0	65	$0.0100 \pm 0.0012^{+0.0026}_{-0.0014}$
4.0	85	$0.0343 \pm 0.0025^{+0.0028}_{-0.0035}$	27.0	85	$0.0107 \pm 0.0011^{+0.0018}_{-0.0021}$
4.0	115	$0.0348 \pm 0.0024^{+0.0021}_{-0.0024}$	27.0	115	$0.0106 \pm 0.0010^{+0.0010}_{-0.0010}$
4.0	150	$0.0393 \pm 0.0028^{+0.0039}_{-0.0024}$	27.0	150	$0.0113 \pm 0.0013^{+0.0010}_{-0.0014}$
4.0	180	$0.0434 \pm 0.0027^{+0.0026}_{-0.0028}$	27.0	180	$0.0106 \pm 0.0013^{+0.0017}_{-0.0008}$
4.0	220	$0.0375 \pm 0.0026^{+0.0031}_{-0.0031}$	27.0	220	$0.0114 \pm 0.0012^{+0.0012}_{-0.0013}$
6.0	45	$0.0384 \pm 0.0029^{+0.0033}_{-0.0044}$			
6.0	65	$0.0358 \pm 0.0030^{+0.0036}_{-0.0015}$	55.0	65	$0.0034 \pm 0.0010^{+0.0007}_{-0.0002}$
6.0	85	$0.0388 \pm 0.0032^{+0.0030}_{-0.0029}$	55.0	85	$0.0047 \pm 0.0010^{+0.0004}_{-0.0005}$
6.0	115	$0.0325 \pm 0.0024^{+0.0014}_{-0.0013}$	55.0	115	$0.0042 \pm 0.0009^{+0.0010}_{-0.0004}$
6.0	150	$0.0408 \pm 0.0032^{+0.0011}_{-0.0021}$	55.0	150	$0.0037 \pm 0.0010^{+0.0014}_{-0.0007}$
6.0	180	$0.0411 \pm 0.0030^{+0.0020}_{-0.0025}$	55.0	180	$0.0046 \pm 0.0009^{+0.0005}_{-0.0012}$
6.0	220	$0.0338 \pm 0.0027^{+0.0016}_{-0.0023}$	55.0	220	$0.0044 \pm 0.0010^{+0.0010}_{-0.0007}$
8.0	45	$0.0343 \pm 0.0022^{+0.0007}_{-0.0011}$			
8.0	65	$0.0332 \pm 0.0022^{+0.0022}_{-0.0041}$			
8.0	85	$0.0338 \pm 0.0021^{+0.0041}_{-0.0022}$			
8.0	115	$0.0305 \pm 0.0019^{+0.0009}_{-0.0012}$			
8.0	150	$0.0324 \pm 0.0022^{+0.0023}_{-0.0023}$			
8.0	180	$0.0272 \pm 0.0018^{+0.0023}_{-0.0008}$			
8.0	220	$0.0290 \pm 0.0020^{+0.0021}_{-0.0018}$			

Table 15: Ratio of the cross section for diffractive scattering, $\gamma^* p \rightarrow X N$, $M_N < 2.3$ GeV, integrated over $M_X = 2 - 4$ GeV, to the total cross section.

Q^2	W	$\frac{\int_{M_a}^{M_b} dM_X d\sigma_{\gamma^* p \rightarrow XN}^{\text{diff}} / dM_X}{\sigma^{\text{tot}}}$	Q^2	W	$\frac{\int_{M_a}^{M_b} dM_X d\sigma_{\gamma^* p \rightarrow XN}^{\text{diff}} / dM_X}{\sigma^{\text{tot}}}$
(GeV ²)	(GeV)	$\pm \text{stat.} \pm \text{syst.}$	(GeV ²)	(GeV)	$\pm \text{stat.} \pm \text{syst.}$
2.7	65	$0.0319 \pm 0.0039^{+0.0016}_{-0.0017}$	14.0	65	$0.0283 \pm 0.0021^{+0.0030}_{-0.0030}$
2.7	85	$0.0358 \pm 0.0040^{+0.0024}_{-0.0018}$	14.0	85	$0.0314 \pm 0.0016^{+0.0040}_{-0.0031}$
2.7	115	$0.0359 \pm 0.0037^{+0.0046}_{-0.0034}$	14.0	115	$0.0279 \pm 0.0014^{+0.0004}_{-0.0026}$
2.7	150	$0.0315 \pm 0.0036^{+0.0027}_{-0.0035}$	14.0	150	$0.0281 \pm 0.0016^{+0.0013}_{-0.0008}$
2.7	180	$0.0340 \pm 0.0034^{+0.0026}_{-0.0032}$	14.0	180	$0.0293 \pm 0.0016^{+0.0009}_{-0.0008}$
			14.0	220	$0.0264 \pm 0.0016^{+0.0016}_{-0.0011}$
4.0	45	$0.0346 \pm 0.0056^{+0.0038}_{-0.0026}$	27.0	65	$0.0234 \pm 0.0026^{+0.0017}_{-0.0026}$
4.0	65	$0.0316 \pm 0.0027^{+0.0034}_{-0.0027}$	27.0	85	$0.0261 \pm 0.0021^{+0.0030}_{-0.0036}$
4.0	85	$0.0336 \pm 0.0026^{+0.0052}_{-0.0033}$	27.0	115	$0.0248 \pm 0.0019^{+0.0015}_{-0.0030}$
4.0	115	$0.0308 \pm 0.0023^{+0.0016}_{-0.0028}$	27.0	150	$0.0232 \pm 0.0020^{+0.0007}_{-0.0008}$
4.0	150	$0.0340 \pm 0.0027^{+0.0016}_{-0.0028}$	27.0	180	$0.0259 \pm 0.0022^{+0.0004}_{-0.0016}$
4.0	180	$0.0335 \pm 0.0024^{+0.0025}_{-0.0017}$	27.0	220	$0.0269 \pm 0.0021^{+0.0008}_{-0.0018}$
4.0	220	$0.0346 \pm 0.0023^{+0.0016}_{-0.0031}$			
6.0	45	$0.0314 \pm 0.0059^{+0.0045}_{-0.0041}$	55.0	65	$0.0112 \pm 0.0027^{+0.0018}_{-0.0014}$
6.0	65	$0.0357 \pm 0.0034^{+0.0027}_{-0.0030}$	55.0	85	$0.0138 \pm 0.0022^{+0.0041}_{-0.0021}$
6.0	85	$0.0338 \pm 0.0029^{+0.0009}_{-0.0032}$	55.0	115	$0.0168 \pm 0.0020^{+0.0008}_{-0.0023}$
6.0	115	$0.0295 \pm 0.0024^{+0.0015}_{-0.0007}$	55.0	150	$0.0120 \pm 0.0020^{+0.0032}_{-0.0014}$
6.0	150	$0.0348 \pm 0.0029^{+0.0023}_{-0.0024}$	55.0	180	$0.0190 \pm 0.0023^{+0.0006}_{-0.0022}$
6.0	180	$0.0312 \pm 0.0024^{+0.0016}_{-0.0020}$	55.0	220	$0.0140 \pm 0.0019^{+0.0009}_{-0.0013}$
6.0	220	$0.0331 \pm 0.0024^{+0.0019}_{-0.0008}$			
8.0	45	$0.0334 \pm 0.0062^{+0.0032}_{-0.0023}$			
8.0	65	$0.0317 \pm 0.0026^{+0.0023}_{-0.0021}$			
8.0	85	$0.0325 \pm 0.0021^{+0.0040}_{-0.0025}$			
8.0	115	$0.0322 \pm 0.0020^{+0.0007}_{-0.0014}$			
8.0	150	$0.0280 \pm 0.0020^{+0.0014}_{-0.0016}$			
8.0	180	$0.0305 \pm 0.0020^{+0.0021}_{-0.0017}$			
8.0	220	$0.0309 \pm 0.0020^{+0.0010}_{-0.0017}$			

Table 16: Ratio of the cross section for diffractive scattering, $\gamma^* p \rightarrow XN$, $M_N < 2.3$ GeV, integrated over $M_X = 4 - 8$ GeV, to the total cross section.

Q^2	W	$\frac{\int_{M_a}^{M_b} dM_X d\sigma_{\gamma^* p \rightarrow X N}^{\text{diff}} / dM_X}{\sigma^{\text{tot}}}$	Q^2	W	$\frac{\int_{M_a}^{M_b} dM_X d\sigma_{\gamma^* p \rightarrow X N}^{\text{diff}} / dM_X}{\sigma^{\text{tot}}}$
(GeV ²)	(GeV)	$\pm \text{stat.} \pm \text{syst.}$	(GeV ²)	(GeV)	$\pm \text{stat.} \pm \text{syst.}$
2.7	85	$0.0302 \pm 0.0065^{+0.0058}_{-0.0020}$	14.0	85	$0.0300 \pm 0.0056^{+0.0054}_{-0.0048}$
2.7	115	$0.0319 \pm 0.0039^{+0.0032}_{-0.0028}$	14.0	115	$0.0272 \pm 0.0024^{+0.0010}_{-0.0021}$
2.7	150	$0.0254 \pm 0.0034^{+0.0031}_{-0.0017}$	14.0	150	$0.0260 \pm 0.0019^{+0.0004}_{-0.0011}$
2.7	180	$0.0282 \pm 0.0030^{+0.0009}_{-0.0034}$	14.0	180	$0.0262 \pm 0.0017^{+0.0014}_{-0.0011}$
2.7	220	$0.0264 \pm 0.0030^{+0.0034}_{-0.0006}$	14.0	220	$0.0269 \pm 0.0018^{+0.0009}_{-0.0006}$
4.0	85	$0.0228 \pm 0.0054^{+0.0036}_{-0.0037}$	27.0	85	$0.0226 \pm 0.0060^{+0.0058}_{-0.0029}$
4.0	115	$0.0274 \pm 0.0031^{+0.0024}_{-0.0018}$	27.0	115	$0.0200 \pm 0.0030^{+0.0029}_{-0.0006}$
4.0	150	$0.0285 \pm 0.0025^{+0.0014}_{-0.0029}$	27.0	150	$0.0198 \pm 0.0023^{+0.0013}_{-0.0012}$
4.0	180	$0.0241 \pm 0.0019^{+0.0018}_{-0.0010}$	27.0	180	$0.0203 \pm 0.0021^{+0.0022}_{-0.0011}$
4.0	220	$0.0244 \pm 0.0019^{+0.0009}_{-0.0017}$	27.0	220	$0.0258 \pm 0.0021^{+0.0007}_{-0.0021}$
6.0	85	$0.0237 \pm 0.0059^{+0.0059}_{-0.0028}$			
6.0	115	$0.0297 \pm 0.0031^{+0.0005}_{-0.0033}$	55.0	115	$0.0264 \pm 0.0037^{+0.0014}_{-0.0025}$
6.0	150	$0.0249 \pm 0.0025^{+0.0016}_{-0.0013}$	55.0	150	$0.0225 \pm 0.0031^{+0.0026}_{-0.0018}$
6.0	180	$0.0269 \pm 0.0024^{+0.0010}_{-0.0015}$	55.0	180	$0.0237 \pm 0.0028^{+0.0021}_{-0.0004}$
6.0	220	$0.0298 \pm 0.0024^{+0.0009}_{-0.0012}$	55.0	220	$0.0238 \pm 0.0028^{+0.0009}_{-0.0015}$
8.0	85	$0.0283 \pm 0.0057^{+0.0026}_{-0.0051}$			
8.0	115	$0.0317 \pm 0.0029^{+0.0018}_{-0.0006}$			
8.0	150	$0.0268 \pm 0.0022^{+0.0012}_{-0.0001}$			
8.0	180	$0.0257 \pm 0.0020^{+0.0005}_{-0.0013}$			
8.0	220	$0.0266 \pm 0.0020^{+0.0020}_{-0.0004}$			

Table 17: Ratio of the cross section for diffractive scattering, $\gamma^* p \rightarrow X N$, $M_N < 2.3$ GeV, integrated over $M_X = 8 - 15$ GeV, to the total cross section.

Q^2	W	$\frac{\int_{M_a}^{M_b} dM_X d\sigma_{\gamma^* p \rightarrow XN}^{\text{diff}} / dM_X}{\sigma^{\text{tot}}}$	Q^2	W	$\frac{\int_{M_a}^{M_b} dM_X d\sigma_{\gamma^* p \rightarrow XN}^{\text{diff}} / dM_X}{\sigma^{\text{tot}}}$
(GeV ²)	(GeV)	$\pm \text{stat.} \pm \text{syst.}$	(GeV ²)	(GeV)	$\pm \text{stat.} \pm \text{syst.}$
2.7	150	$0.0238 \pm 0.0070^{+0.0025}_{-0.0013}$	14.0	150	$0.0193 \pm 0.0054^{+0.0025}_{-0.0020}$
2.7	180	$0.0184 \pm 0.0036^{+0.0023}_{-0.0008}$	14.0	180	$0.0210 \pm 0.0031^{+0.0008}_{-0.0011}$
2.7	220	$0.0267 \pm 0.0034^{+0.0022}_{-0.0017}$	14.0	220	$0.0213 \pm 0.0021^{+0.0009}_{-0.0008}$
4.0	150	$0.0187 \pm 0.0059^{+0.0015}_{-0.0018}$			
4.0	180	$0.0200 \pm 0.0033^{+0.0017}_{-0.0012}$	27.0	180	$0.0190 \pm 0.0036^{+0.0010}_{-0.0014}$
4.0	220	$0.0218 \pm 0.0023^{+0.0012}_{-0.0008}$	27.0	220	$0.0176 \pm 0.0024^{+0.0016}_{-0.0007}$
6.0	150	$0.0214 \pm 0.0058^{+0.0027}_{-0.0021}$	55.0	150	$0.0188 \pm 0.0065^{+0.0039}_{-0.0047}$
6.0	180	$0.0206 \pm 0.0034^{+0.0004}_{-0.0029}$	55.0	180	$0.0142 \pm 0.0038^{+0.0016}_{-0.0019}$
6.0	220	$0.0208 \pm 0.0023^{+0.0014}_{-0.0018}$	55.0	220	$0.0157 \pm 0.0029^{+0.0036}_{-0.0011}$
8.0	150	$0.0205 \pm 0.0054^{+0.0017}_{-0.0016}$			
8.0	180	$0.0245 \pm 0.0033^{+0.0005}_{-0.0026}$			
8.0	220	$0.0216 \pm 0.0023^{+0.0007}_{-0.0026}$			

Table 18: Ratio of the cross section for diffractive scattering, $\gamma^* p \rightarrow XN$, $M_N < 2.3$ GeV, integrated over $M_X = 15 - 25$ GeV, to the total cross section.

Q^2	W	$\frac{\int_{M_a}^{M_b} dM_X d\sigma_{\gamma^* p \rightarrow XN}^{\text{diff}} / dM_X}{\sigma^{\text{tot}}}$	Q^2	W	$\frac{\int_{M_a}^{M_b} dM_X d\sigma_{\gamma^* p \rightarrow XN}^{\text{diff}} / dM_X}{\sigma^{\text{tot}}}$
(GeV ²)	(GeV)	$\pm \text{stat.} \pm \text{syst.}$	(GeV ²)	(GeV)	$\pm \text{stat.} \pm \text{syst.}$
2.7	220	$0.0158 \pm 0.0047^{+0.0023}_{-0.0015}$	14.0	220	$0.0151 \pm 0.0040^{+0.0015}_{-0.0010}$
4.0	220	$0.0135 \pm 0.0039^{+0.0005}_{-0.0016}$	27.0	220	$0.0111 \pm 0.0039^{+0.0012}_{-0.0014}$
6.0	220	$0.0127 \pm 0.0038^{+0.0020}_{-0.0015}$			
8.0	220	$0.0126 \pm 0.0040^{+0.0025}_{-0.0006}$			

Table 19: Ratio of the cross section for diffractive scattering, $\gamma^* p \rightarrow XN$, $M_N < 2.3$ GeV, integrated over $M_X = 25 - 35$ GeV, to the total cross section.

Q^2 (GeV 2)	$\sigma^{\text{diff}}/\sigma^{\text{tot}}$ \pm stat. \pm syst.
4.0	$0.158 \pm 0.007^{+0.009}_{-0.007}$
6.0	$0.149 \pm 0.007^{+0.005}_{-0.005}$
8.0	$0.134 \pm 0.006^{+0.005}_{-0.004}$
14.0	$0.118 \pm 0.005^{+0.003}_{-0.002}$
27.0	$0.096 \pm 0.006^{+0.003}_{-0.004}$

Table 20: *Ratio of the total diffractive cross section observed to the total cross section, $\sigma^{\text{diff}}(0.28 < M_X < 35\text{GeV}, M_N < 2.3\text{GeV})/\sigma^{\text{tot}}$, for $200 < W < 245$ GeV, at different values of Q^2 .*

β	x_{IP}	Q^2	$x_{IP}F_2^{D(3)}$ ± stat. ± syst. (GeV 2)	β	x_{IP}	Q^2	$x_{IP}F_2^{D(3)}$ ± stat. ± syst. (GeV 2)
0.6522	0.00204	2.7	$0.0321 \pm 0.0032^{+0.0045}_{-0.0033}$	0.7353	0.00268	4.0	$0.0314 \pm 0.0018^{+0.0032}_{-0.0044}$
0.6522	0.00098	2.7	$0.0377 \pm 0.0037^{+0.0059}_{-0.0047}$	0.7353	0.00129	4.0	$0.0342 \pm 0.0022^{+0.0046}_{-0.0051}$
0.6522	0.00057	2.7	$0.0396 \pm 0.0037^{+0.0035}_{-0.0033}$	0.7353	0.00075	4.0	$0.0392 \pm 0.0025^{+0.0056}_{-0.0052}$
0.6522	0.00031	2.7	$0.0398 \pm 0.0031^{+0.0041}_{-0.0036}$	0.7353	0.00041	4.0	$0.0456 \pm 0.0026^{+0.0049}_{-0.0045}$
0.6522	0.00018	2.7	$0.0419 \pm 0.0036^{+0.0047}_{-0.0048}$	0.7353	0.00024	4.0	$0.0389 \pm 0.0027^{+0.0052}_{-0.0039}$
0.6522	0.00013	2.7	$0.0362 \pm 0.0035^{+0.0060}_{-0.0037}$	0.7353	0.00017	4.0	$0.0488 \pm 0.0033^{+0.0043}_{-0.0051}$
				0.7353	0.00011	4.0	$0.0381 \pm 0.0039^{+0.0114}_{-0.0059}$
0.2308	0.00577	2.7	$0.0236 \pm 0.0024^{+0.0025}_{-0.0024}$	0.3077	0.00641	4.0	$0.0257 \pm 0.0016^{+0.0022}_{-0.0013}$
0.2308	0.00277	2.7	$0.0224 \pm 0.0027^{+0.0014}_{-0.0018}$	0.3077	0.00307	4.0	$0.0281 \pm 0.0019^{+0.0028}_{-0.0030}$
0.2308	0.00162	2.7	$0.0236 \pm 0.0028^{+0.0030}_{-0.0018}$	0.3077	0.00180	4.0	$0.0288 \pm 0.0020^{+0.0024}_{-0.0029}$
0.2308	0.00088	2.7	$0.0261 \pm 0.0027^{+0.0021}_{-0.0021}$	0.3077	0.00098	4.0	$0.0318 \pm 0.0021^{+0.0019}_{-0.0022}$
0.2308	0.00052	2.7	$0.0362 \pm 0.0034^{+0.0019}_{-0.0028}$	0.3077	0.00058	4.0	$0.0388 \pm 0.0027^{+0.0039}_{-0.0023}$
0.2308	0.00036	2.7	$0.0377 \pm 0.0032^{+0.0038}_{-0.0036}$	0.3077	0.00040	4.0	$0.0479 \pm 0.0029^{+0.0029}_{-0.0030}$
				0.3077	0.00027	4.0	$0.0444 \pm 0.0029^{+0.0037}_{-0.0037}$
0.0698	0.00915	2.7	$0.0172 \pm 0.0020^{+0.0009}_{-0.0009}$	0.1000	0.01971	4.0	$0.0180 \pm 0.0029^{+0.0020}_{-0.0013}$
0.0698	0.00535	2.7	$0.0204 \pm 0.0022^{+0.0014}_{-0.0010}$	0.1000	0.00946	4.0	$0.0185 \pm 0.0015^{+0.0020}_{-0.0016}$
0.0698	0.00293	2.7	$0.0216 \pm 0.0022^{+0.0027}_{-0.0021}$	0.1000	0.00553	4.0	$0.0217 \pm 0.0016^{+0.0033}_{-0.0022}$
0.0698	0.00172	2.7	$0.0210 \pm 0.0024^{+0.0018}_{-0.0024}$	0.1000	0.00302	4.0	$0.0216 \pm 0.0016^{+0.0011}_{-0.0020}$
0.0698	0.00119	2.7	$0.0243 \pm 0.0023^{+0.0019}_{-0.0023}$	0.1000	0.00178	4.0	$0.0258 \pm 0.0020^{+0.0012}_{-0.0022}$
				0.1000	0.00123	4.0	$0.0284 \pm 0.0019^{+0.0021}_{-0.0014}$
				0.1000	0.00083	4.0	$0.0315 \pm 0.0020^{+0.0014}_{-0.0028}$
0.0218	0.01711	2.7	$0.0171 \pm 0.0037^{+0.0033}_{-0.0011}$	0.0320	0.01729	4.0	$0.0143 \pm 0.0034^{+0.0022}_{-0.0023}$
0.0218	0.00935	2.7	$0.0191 \pm 0.0023^{+0.0019}_{-0.0017}$	0.0320	0.00945	4.0	$0.0188 \pm 0.0021^{+0.0017}_{-0.0012}$
0.0218	0.00550	2.7	$0.0169 \pm 0.0022^{+0.0021}_{-0.0011}$	0.0320	0.00556	4.0	$0.0211 \pm 0.0019^{+0.0010}_{-0.0022}$
0.0218	0.00382	2.7	$0.0201 \pm 0.0021^{+0.0006}_{-0.0024}$	0.0320	0.00386	4.0	$0.0199 \pm 0.0016^{+0.0015}_{-0.0008}$
0.0218	0.00256	2.7	$0.0205 \pm 0.0022^{+0.0026}_{-0.0005}$	0.0320	0.00258	4.0	$0.0217 \pm 0.0016^{+0.0008}_{-0.0015}$
0.0067	0.01790	2.7	$0.0198 \pm 0.0058^{+0.0021}_{-0.0011}$	0.0099	0.01795	4.0	$0.0173 \pm 0.0055^{+0.0013}_{-0.0017}$
0.0067	0.01243	2.7	$0.0165 \pm 0.0032^{+0.0020}_{-0.0008}$	0.0099	0.01247	4.0	$0.0206 \pm 0.0033^{+0.0017}_{-0.0012}$
0.0067	0.00832	2.7	$0.0260 \pm 0.0032^{+0.0021}_{-0.0016}$	0.0099	0.00835	4.0	$0.0241 \pm 0.0025^{+0.0014}_{-0.0009}$
0.0030	0.01865	2.7	$0.0229 \pm 0.0067^{+0.0033}_{-0.0022}$	0.0044	0.01868	4.0	$0.0222 \pm 0.0063^{+0.0008}_{-0.0027}$

Table 21: The diffractive structure function multiplied by x_{IP} , $x_{IP}F_2^{D(3)}(\beta, x_{IP}, Q^2)$ for diffractive scattering, $\gamma^*p \rightarrow XN$, $M_N < 2.3$ GeV, for $Q^2 = 2.7$ and 4.0 GeV 2 , in bins of β and x_{IP} .

β	x_{IP}	Q^2	$x_{IP}F_2^{D(3)}$ ± stat. ± syst.	β	x_{IP}	Q^2	$x_{IP}F_2^{D(3)}$ ± stat. ± syst.
(GeV 2)				(GeV 2)			
0.8065	0.00366	6.0	$0.0272 \pm 0.0023^{+0.0029}_{-0.0035}$	0.8475	0.00464	8.0	$0.0297 \pm 0.0023^{+0.0031}_{-0.0034}$
0.8065	0.00176	6.0	$0.0319 \pm 0.0029^{+0.0072}_{-0.0033}$	0.8475	0.00223	8.0	$0.0338 \pm 0.0025^{+0.0047}_{-0.0043}$
0.8065	0.00103	6.0	$0.0321 \pm 0.0029^{+0.0036}_{-0.0037}$	0.8475	0.00131	8.0	$0.0353 \pm 0.0026^{+0.0055}_{-0.0043}$
0.8065	0.00056	6.0	$0.0350 \pm 0.0029^{+0.0034}_{-0.0048}$	0.8475	0.00071	8.0	$0.0400 \pm 0.0029^{+0.0043}_{-0.0040}$
0.8065	0.00033	6.0	$0.0425 \pm 0.0037^{+0.0046}_{-0.0041}$	0.8475	0.00042	8.0	$0.0426 \pm 0.0035^{+0.0036}_{-0.0037}$
0.8065	0.00023	6.0	$0.0371 \pm 0.0034^{+0.0052}_{-0.0032}$	0.8475	0.00029	8.0	$0.0489 \pm 0.0037^{+0.0035}_{-0.0067}$
0.8065	0.00015	6.0	$0.0422 \pm 0.0046^{+0.0078}_{-0.0079}$	0.8475	0.00020	8.0	$0.0396 \pm 0.0040^{+0.0076}_{-0.0044}$
0.4000	0.00739	6.0	$0.0305 \pm 0.0022^{+0.0026}_{-0.0035}$	0.4706	0.00836	8.0	$0.0324 \pm 0.0020^{+0.0007}_{-0.0010}$
0.4000	0.00354	6.0	$0.0333 \pm 0.0027^{+0.0033}_{-0.0014}$	0.4706	0.00402	8.0	$0.0364 \pm 0.0023^{+0.0024}_{-0.0045}$
0.4000	0.00207	6.0	$0.0398 \pm 0.0032^{+0.0030}_{-0.0030}$	0.4706	0.00235	8.0	$0.0416 \pm 0.0025^{+0.0051}_{-0.0026}$
0.4000	0.00113	6.0	$0.0370 \pm 0.0027^{+0.0016}_{-0.0015}$	0.4706	0.00129	8.0	$0.0414 \pm 0.0025^{+0.0013}_{-0.0017}$
0.4000	0.00067	6.0	$0.0521 \pm 0.0039^{+0.0013}_{-0.0027}$	0.4706	0.00076	8.0	$0.0498 \pm 0.0032^{+0.0036}_{-0.0035}$
0.4000	0.00046	6.0	$0.0566 \pm 0.0041^{+0.0028}_{-0.0035}$	0.4706	0.00052	8.0	$0.0461 \pm 0.0030^{+0.0039}_{-0.0013}$
0.4000	0.00031	6.0	$0.0520 \pm 0.0041^{+0.0024}_{-0.0035}$	0.4706	0.00035	8.0	$0.0536 \pm 0.0035^{+0.0039}_{-0.0033}$
0.1429	0.02068	6.0	$0.0174 \pm 0.0032^{+0.0025}_{-0.0023}$	0.1818	0.02164	8.0	$0.0204 \pm 0.0038^{+0.0019}_{-0.0014}$
0.1429	0.00993	6.0	$0.0233 \pm 0.0022^{+0.0017}_{-0.0020}$	0.1818	0.01039	8.0	$0.0225 \pm 0.0018^{+0.0017}_{-0.0015}$
0.1429	0.00581	6.0	$0.0242 \pm 0.0020^{+0.0006}_{-0.0023}$	0.1818	0.00608	8.0	$0.0259 \pm 0.0016^{+0.0032}_{-0.0020}$
0.1429	0.00317	6.0	$0.0235 \pm 0.0019^{+0.0012}_{-0.0005}$	0.1818	0.00332	8.0	$0.0283 \pm 0.0017^{+0.0006}_{-0.0013}$
0.1429	0.00187	6.0	$0.0311 \pm 0.0025^{+0.0020}_{-0.0021}$	0.1818	0.00195	8.0	$0.0279 \pm 0.0019^{+0.0014}_{-0.0016}$
0.1429	0.00130	6.0	$0.0301 \pm 0.0022^{+0.0015}_{-0.0020}$	0.1818	0.00136	8.0	$0.0335 \pm 0.0021^{+0.0023}_{-0.0019}$
0.1429	0.00087	6.0	$0.0356 \pm 0.0025^{+0.0020}_{-0.0009}$	0.1818	0.00091	8.0	$0.0369 \pm 0.0023^{+0.0012}_{-0.0020}$
0.0472	0.01756	6.0	$0.0160 \pm 0.0040^{+0.0040}_{-0.0019}$	0.0620	0.01783	8.0	$0.0206 \pm 0.0042^{+0.0019}_{-0.0037}$
0.0472	0.00960	6.0	$0.0223 \pm 0.0023^{+0.0004}_{-0.0025}$	0.0620	0.00975	8.0	$0.0255 \pm 0.0023^{+0.0014}_{-0.0005}$
0.0472	0.00564	6.0	$0.0210 \pm 0.0021^{+0.0014}_{-0.0011}$	0.0620	0.00573	8.0	$0.0243 \pm 0.0019^{+0.0011}_{-0.0001}$
0.0472	0.00392	6.0	$0.0244 \pm 0.0021^{+0.0009}_{-0.0013}$	0.0620	0.00398	8.0	$0.0258 \pm 0.0019^{+0.0005}_{-0.0013}$
0.0472	0.00262	6.0	$0.0302 \pm 0.0024^{+0.0009}_{-0.0012}$	0.0620	0.00267	8.0	$0.0291 \pm 0.0021^{+0.0022}_{-0.0005}$
0.0148	0.01804	6.0	$0.0222 \pm 0.0060^{+0.0028}_{-0.0022}$	0.0196	0.01813	8.0	$0.0227 \pm 0.0059^{+0.0019}_{-0.0018}$
0.0148	0.01253	6.0	$0.0231 \pm 0.0038^{+0.0004}_{-0.0033}$	0.0196	0.01259	8.0	$0.0299 \pm 0.0040^{+0.0007}_{-0.0031}$
0.0148	0.00839	6.0	$0.0260 \pm 0.0028^{+0.0017}_{-0.0023}$	0.0196	0.00843	8.0	$0.0288 \pm 0.0030^{+0.0010}_{-0.0034}$
0.0066	0.01872	6.0	$0.0237 \pm 0.0071^{+0.0036}_{-0.0027}$	0.0088	0.01876	8.0	$0.0250 \pm 0.0080^{+0.0050}_{-0.0012}$

Table 22: The diffractive structure function multiplied by x_{IP} , $x_{IP}F_2^{D(3)}(\beta, x_{IP}, Q^2)$ for diffractive scattering, $\gamma^*p \rightarrow XN$, $M_N < 2.3$ GeV, for $Q^2 = 6.0$ and 8.0 GeV 2 , in bins of β and x_{IP} .

β	x_{IP}	Q^2	$x_{IP} F_2^{D(3)}$		β	x_{IP}	Q^2	$x_{IP} F_2^{D(3)}$	
			\pm stat.	\pm syst.				\pm stat.	\pm syst.
(GeV 2)					(GeV 2)				
0.9067	0.00757	14.0	0.0253	$\pm 0.0018^{+0.0034}_{-0.0029}$	0.9494	0.01386	27.0	0.0181	$\pm 0.0029^{+0.0016}_{-0.0035}$
0.9067	0.00364	14.0	0.0244	$\pm 0.0019^{+0.0031}_{-0.0036}$	0.9494	0.00669	27.0	0.0154	$\pm 0.0031^{+0.0029}_{-0.0017}$
0.9067	0.00213	14.0	0.0324	$\pm 0.0022^{+0.0045}_{-0.0055}$	0.9494	0.00392	27.0	0.0251	$\pm 0.0037^{+0.0039}_{-0.0045}$
0.9067	0.00117	14.0	0.0313	$\pm 0.0022^{+0.0033}_{-0.0027}$	0.9494	0.00215	27.0	0.0133	$\pm 0.0032^{+0.0026}_{-0.0024}$
0.9067	0.00069	14.0	0.0336	$\pm 0.0028^{+0.0026}_{-0.0038}$	0.9494	0.00126	27.0	0.0343	$\pm 0.0062^{+0.0025}_{-0.0107}$
0.9067	0.00048	14.0	0.0248	$\pm 0.0024^{+0.0029}_{-0.0027}$	0.9494	0.00088	27.0	0.0227	$\pm 0.0052^{+0.0041}_{-0.0046}$
0.9067	0.00032	14.0	0.0425	$\pm 0.0040^{+0.0048}_{-0.0044}$	0.9494	0.00059	27.0	0.0274	$\pm 0.0056^{+0.0058}_{-0.0029}$
0.6087	0.01128	14.0	0.0292	$\pm 0.0017^{+0.0013}_{-0.0020}$	0.7500	0.01754	27.0	0.0151	$\pm 0.0020^{+0.0023}_{-0.0017}$
0.6087	0.00543	14.0	0.0322	$\pm 0.0018^{+0.0035}_{-0.0024}$	0.7500	0.00847	27.0	0.0237	$\pm 0.0027^{+0.0061}_{-0.0032}$
0.6087	0.00318	14.0	0.0384	$\pm 0.0020^{+0.0063}_{-0.0043}$	0.7500	0.00496	27.0	0.0286	$\pm 0.0029^{+0.0048}_{-0.0055}$
0.6087	0.00174	14.0	0.0421	$\pm 0.0021^{+0.0011}_{-0.0027}$	0.7500	0.00272	27.0	0.0338	$\pm 0.0032^{+0.0033}_{-0.0031}$
0.6087	0.00102	14.0	0.0425	$\pm 0.0027^{+0.0035}_{-0.0017}$	0.7500	0.00160	27.0	0.0404	$\pm 0.0045^{+0.0037}_{-0.0049}$
0.6087	0.00071	14.0	0.0495	$\pm 0.0030^{+0.0054}_{-0.0045}$	0.7500	0.00111	27.0	0.0411	$\pm 0.0048^{+0.0065}_{-0.0030}$
0.6087	0.00048	14.0	0.0546	$\pm 0.0036^{+0.0047}_{-0.0038}$	0.7500	0.00074	27.0	0.0497	$\pm 0.0050^{+0.0054}_{-0.0057}$
0.2800	0.01180	14.0	0.0237	$\pm 0.0017^{+0.0025}_{-0.0025}$	0.4286	0.01482	27.0	0.0242	$\pm 0.0027^{+0.0017}_{-0.0027}$
0.2800	0.00691	14.0	0.0291	$\pm 0.0014^{+0.0037}_{-0.0028}$	0.4286	0.00869	27.0	0.0306	$\pm 0.0023^{+0.0035}_{-0.0042}$
0.2800	0.00378	14.0	0.0298	$\pm 0.0015^{+0.0005}_{-0.0028}$	0.4286	0.00475	27.0	0.0345	$\pm 0.0026^{+0.0020}_{-0.0042}$
0.2800	0.00222	14.0	0.0337	$\pm 0.0019^{+0.0015}_{-0.0010}$	0.4286	0.00280	27.0	0.0362	$\pm 0.0031^{+0.0010}_{-0.0013}$
0.2800	0.00154	14.0	0.0384	$\pm 0.0020^{+0.0012}_{-0.0010}$	0.4286	0.00194	27.0	0.0440	$\pm 0.0036^{+0.0006}_{-0.0027}$
0.2800	0.00103	14.0	0.0384	$\pm 0.0022^{+0.0023}_{-0.0016}$	0.4286	0.00130	27.0	0.0515	$\pm 0.0038^{+0.0016}_{-0.0035}$
0.1037	0.01865	14.0	0.0234	$\pm 0.0043^{+0.0042}_{-0.0038}$	0.1824	0.02041	27.0	0.0193	$\pm 0.0052^{+0.0050}_{-0.0025}$
0.1037	0.01020	14.0	0.0245	$\pm 0.0021^{+0.0009}_{-0.0019}$	0.1824	0.01117	27.0	0.0203	$\pm 0.0030^{+0.0029}_{-0.0006}$
0.1037	0.00600	14.0	0.0262	$\pm 0.0019^{+0.0004}_{-0.0011}$	0.1824	0.00657	27.0	0.0227	$\pm 0.0025^{+0.0014}_{-0.0014}$
0.1037	0.00416	14.0	0.0289	$\pm 0.0018^{+0.0015}_{-0.0012}$	0.1824	0.00456	27.0	0.0253	$\pm 0.0025^{+0.0027}_{-0.0014}$
0.1037	0.00279	14.0	0.0330	$\pm 0.0021^{+0.0011}_{-0.0008}$	0.1824	0.00306	27.0	0.0363	$\pm 0.0028^{+0.0009}_{-0.0030}$
0.0338	0.01839	14.0	0.0230	$\pm 0.0064^{+0.0030}_{-0.0024}$					
0.0338	0.01277	14.0	0.0273	$\pm 0.0040^{+0.0011}_{-0.0015}$	0.0632	0.01317	27.0	0.0262	$\pm 0.0049^{+0.0014}_{-0.0019}$
0.0338	0.00855	14.0	0.0308	$\pm 0.0029^{+0.0012}_{-0.0012}$	0.0632	0.00882	27.0	0.0275	$\pm 0.0036^{+0.0025}_{-0.0011}$
0.0153	0.01888	14.0	0.0321	$\pm 0.0085^{+0.0032}_{-0.0021}$	0.0291	0.01914	27.0	0.0252	$\pm 0.0088^{+0.0027}_{-0.0031}$

Table 23: The diffractive structure function multiplied by x_{IP} , $x_{IP} F_2^{D(3)}(\beta, x_{IP}, Q^2)$ for diffractive scattering, $\gamma^* p \rightarrow XN$, $M_N < 2.3$ GeV, for $Q^2 = 14.0$ and 27.0 GeV 2 , in bins of β and x_{IP} .

β	x_{IP}	Q^2	$x_{\text{IP}}F_2^{D(3)}$ ± stat. ± syst.
(GeV 2)			
0.9745	0.02713	55.0	$0.0121 \pm 0.0045^{+0.0040}_{-0.0046}$
0.9745	0.01319	55.0	$0.0148 \pm 0.0067^{+0.0026}_{-0.0027}$
0.9745	0.00775	55.0	$0.0062 \pm 0.0035^{+0.0058}_{-0.0016}$
0.9745	0.00425	55.0	$0.0136 \pm 0.0047^{+0.0016}_{-0.0027}$
0.9745	0.00250	55.0	$0.0171 \pm 0.0108^{+0.0111}_{-0.0032}$
0.9745	0.00117	55.0	$0.0163 \pm 0.0086^{+0.0024}_{-0.0099}$
0.8594	0.01495	55.0	$0.0131 \pm 0.0037^{+0.0026}_{-0.0007}$
0.8594	0.00879	55.0	$0.0208 \pm 0.0042^{+0.0018}_{-0.0024}$
0.8594	0.00482	55.0	$0.0211 \pm 0.0045^{+0.0050}_{-0.0019}$
0.8594	0.00284	55.0	$0.0212 \pm 0.0060^{+0.0080}_{-0.0040}$
0.8594	0.00197	55.0	$0.0313 \pm 0.0063^{+0.0031}_{-0.0080}$
0.8594	0.00132	55.0	$0.0345 \pm 0.0075^{+0.0076}_{-0.0053}$
0.6044	0.02126	55.0	$0.0155 \pm 0.0037^{+0.0025}_{-0.0019}$
0.6044	0.01250	55.0	$0.0218 \pm 0.0034^{+0.0064}_{-0.0033}$
0.6044	0.00685	55.0	$0.0296 \pm 0.0034^{+0.0015}_{-0.0040}$
0.6044	0.00404	55.0	$0.0248 \pm 0.0041^{+0.0066}_{-0.0030}$
0.6044	0.00280	55.0	$0.0459 \pm 0.0053^{+0.0016}_{-0.0054}$
0.6044	0.00188	55.0	$0.0388 \pm 0.0051^{+0.0026}_{-0.0035}$
0.3125	0.01325	55.0	$0.0281 \pm 0.0039^{+0.0015}_{-0.0027}$
0.3125	0.00780	55.0	$0.0279 \pm 0.0038^{+0.0033}_{-0.0023}$
0.3125	0.00542	55.0	$0.0345 \pm 0.0039^{+0.0031}_{-0.0005}$
0.3125	0.00363	55.0	$0.0398 \pm 0.0045^{+0.0016}_{-0.0025}$
0.1209	0.02017	55.0	$0.0232 \pm 0.0080^{+0.0049}_{-0.0058}$
0.1209	0.01402	55.0	$0.0205 \pm 0.0054^{+0.0023}_{-0.0027}$
0.1209	0.00939	55.0	$0.0261 \pm 0.0049^{+0.0060}_{-0.0018}$

Table 24: The diffractive structure function multiplied by x_{IP} , $x_{\text{IP}}F_2^{D(3)}(\beta, x_{\text{IP}}, Q^2)$ for diffractive scattering, $\gamma^*p \rightarrow XN$, $M_N < 2.3$ GeV, for $Q^2 = 55.0$ GeV 2 , in bins of β and x_{IP} .

Q^2 (GeV 2)	β	$x_0 F_2^{D(3)}$ \pm stat. \pm syst.
2.7	0.2308	$0.0219 \pm 0.0022^{+0.0023}_{-0.0022}$
	0.0698	$0.0178 \pm 0.0014^{+0.0010}_{-0.0009}$
	0.0218	$0.0171 \pm 0.0015^{+0.0019}_{-0.0013}$
	0.0067	$0.0214 \pm 0.0023^{+0.0021}_{-0.0012}$
	0.3077	$0.0239 \pm 0.0015^{+0.0021}_{-0.0012}$
	0.1000	$0.0190 \pm 0.0011^{+0.0025}_{-0.0018}$
	0.0320	$0.0189 \pm 0.0013^{+0.0012}_{-0.0017}$
	0.0099	$0.0227 \pm 0.0020^{+0.0015}_{-0.0010}$
6.0	0.4000	$0.0288 \pm 0.0021^{+0.0025}_{-0.0033}$
	0.1429	$0.0225 \pm 0.0014^{+0.0011}_{-0.0020}$
	0.0472	$0.0202 \pm 0.0015^{+0.0009}_{-0.0016}$
	0.0148	$0.0248 \pm 0.0023^{+0.0013}_{-0.0026}$
	0.4706	$0.0312 \pm 0.0019^{+0.0007}_{-0.0010}$
	0.1818	$0.0231 \pm 0.0011^{+0.0024}_{-0.0017}$
	0.0620	$0.0231 \pm 0.0014^{+0.0011}_{-0.0002}$
	0.0196	$0.0290 \pm 0.0024^{+0.0009}_{-0.0033}$
14.0	0.9067	$0.0246 \pm 0.0018^{+0.0033}_{-0.0028}$
	0.6087	$0.0288 \pm 0.0012^{+0.0023}_{-0.0021}$
	0.2800	$0.0259 \pm 0.0011^{+0.0031}_{-0.0026}$
	0.1037	$0.0237 \pm 0.0013^{+0.0006}_{-0.0013}$
	0.0338	$0.0295 \pm 0.0024^{+0.0012}_{-0.0013}$
27.0	0.9494	$0.0167 \pm 0.0021^{+0.0022}_{-0.0026}$
	0.7500	$0.0227 \pm 0.0026^{+0.0058}_{-0.0031}$
	0.4286	$0.0285 \pm 0.0018^{+0.0029}_{-0.0037}$
	0.1824	$0.0205 \pm 0.0018^{+0.0019}_{-0.0011}$
	0.0632	$0.0270 \pm 0.0029^{+0.0021}_{-0.0014}$
55.0	0.9745	$0.0080 \pm 0.0031^{+0.0051}_{-0.0018}$
	0.8594	$0.0173 \pm 0.0029^{+0.0023}_{-0.0015}$
	0.6044	$0.0250 \pm 0.0023^{+0.0036}_{-0.0036}$
	0.3125	$0.0279 \pm 0.0021^{+0.0025}_{-0.0016}$
	0.1209	$0.0246 \pm 0.0037^{+0.0046}_{-0.0022}$

Table 25: The diffractive structure function of the proton multiplied by x_{p} at the point $x_{\text{p}} \equiv x_0 = 0.01$, $x_0 F_2^{D(3)}(\beta, x_0, Q^2)$, in bins of Q^2 and β .

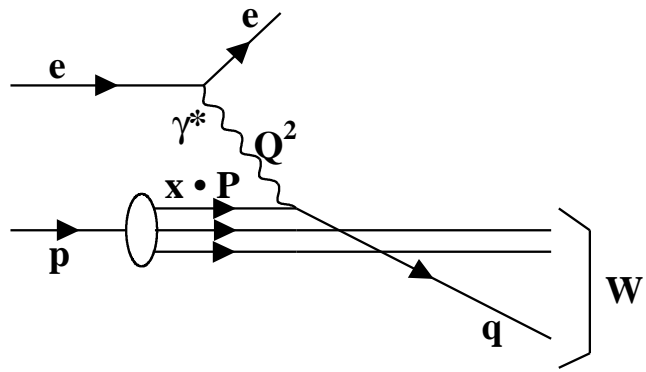


Figure 1: Non-peripheral deep inelastic scattering.

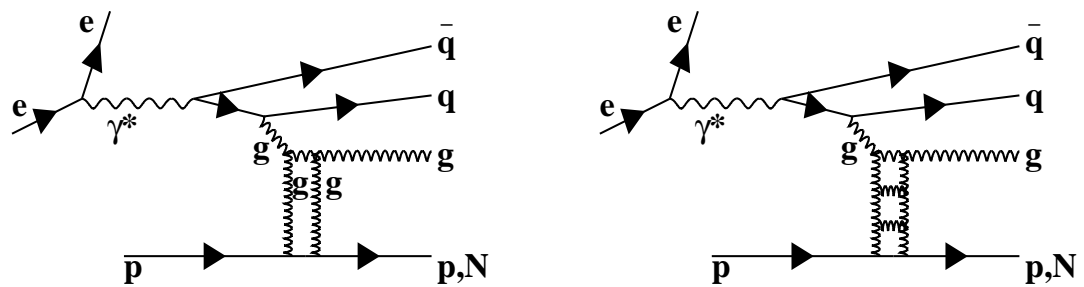
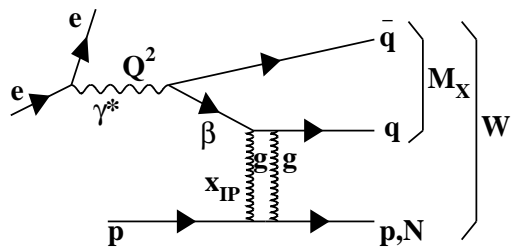


Figure 2: Diffractive deep inelastic scattering, $ep \rightarrow eXN$.

ZEUS

• SATRAP+ZEUSVM+SANG($M_N < 2.3$ GeV)

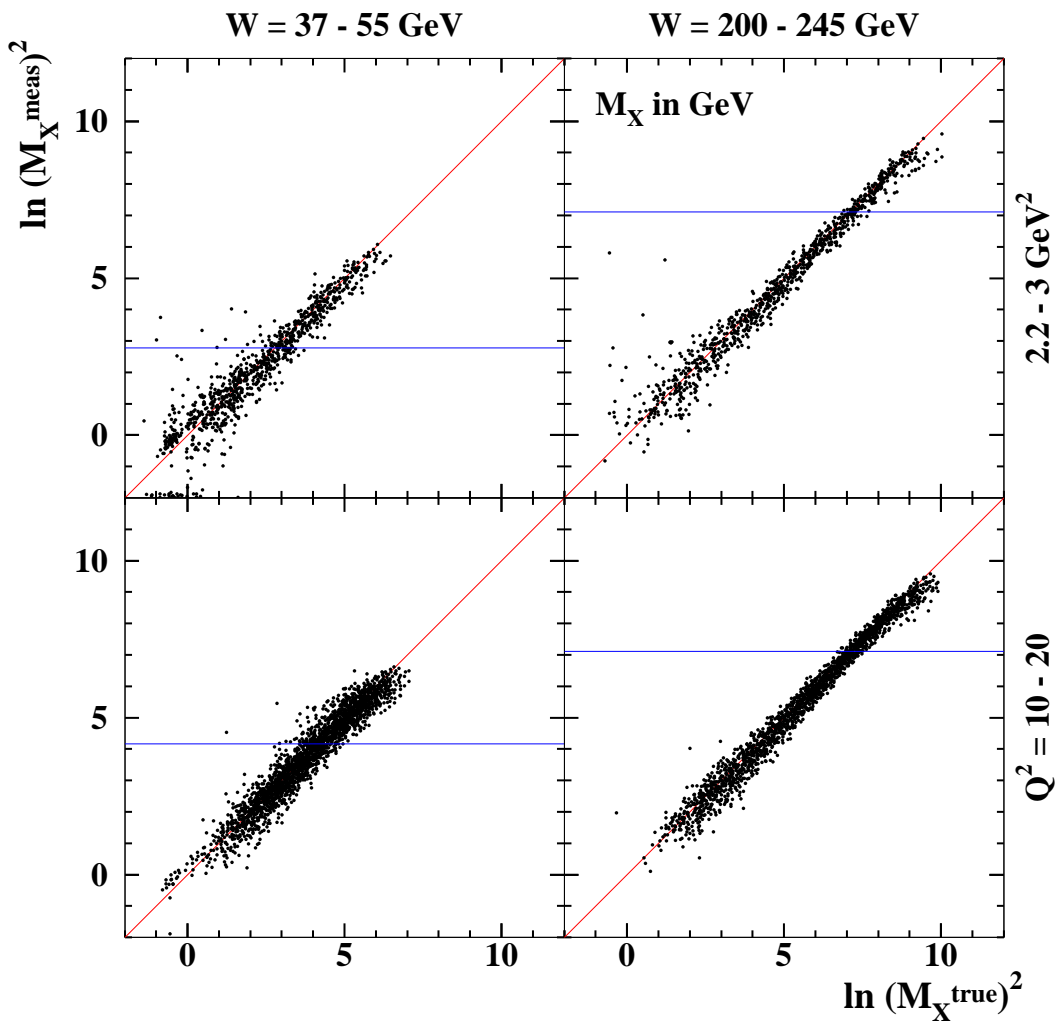


Figure 3: The measured versus the generated $\ln M_X^2$ values for the lowest and highest W bins at low and high Q^2 as determined by Monte Carlo simulation. The horizontal lines give the maximum values of $\ln M_X^2$ for which the diffractive contribution was determined. Lines are drawn at $\ln(M_X^{\text{meas}})^2 = \ln(M_X^{\text{true}})^2$ to guide the eye.

ZEUS

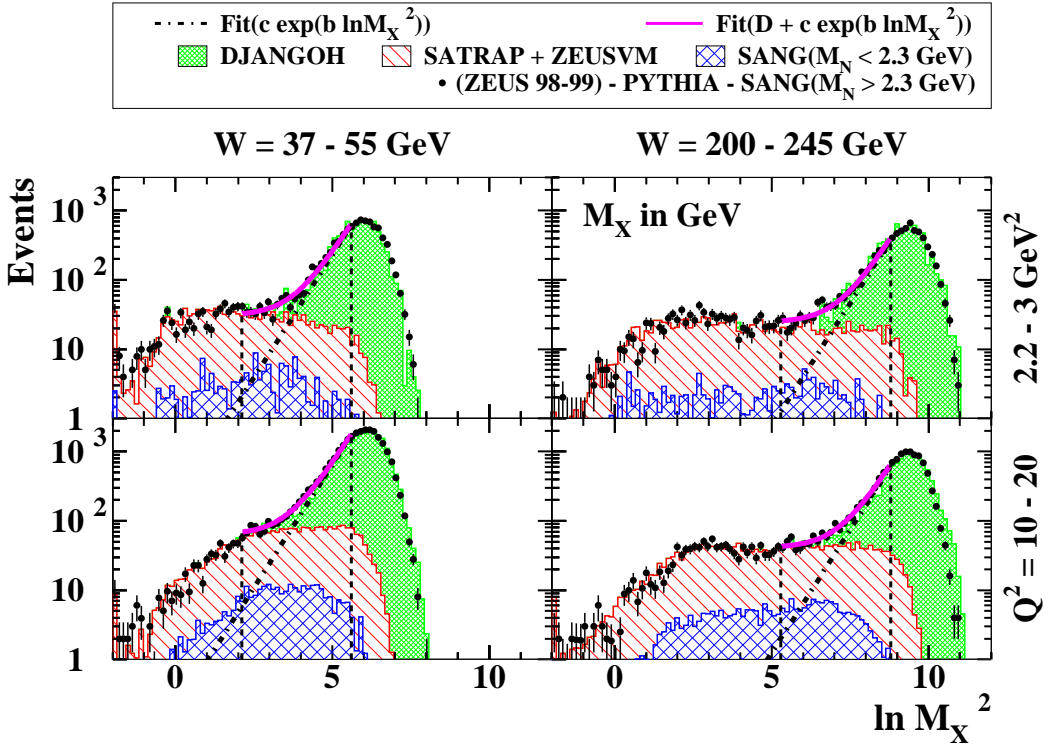


Figure 4: Distributions of $\ln M_X^2$ (M_X in units of GeV) at the detector level for different (W, Q^2) bins. The points with error bars show the data. The shaded areas show the non-peripheral contributions as predicted by DJANGOH. The diffractive contributions from $\gamma^*p \rightarrow Xp$ ($\gamma^*p \rightarrow XN$, $M_N < 2.3$ GeV) as predicted by SATRAP+ZEUSVM (SANG) are shown as hatched (cross-hatched) areas. The dash-dotted lines show the results for the non-diffractive contribution from fitting the data in the $\ln M_X^2$ range delimited by the two vertical dashed lines.

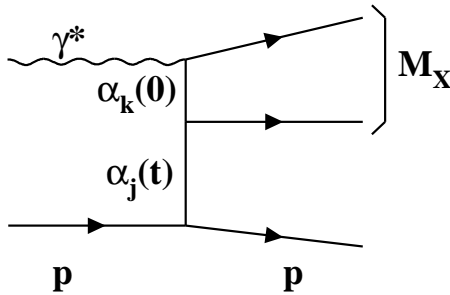


Figure 5: The reaction $\gamma^*p \rightarrow Xp$ proceeding via the exchange of a Reggeon α_j in the t -channel. The system X is produced by the scattering of the virtual photon on the Reggeon via the exchange of the pole α_k .

ZEUS

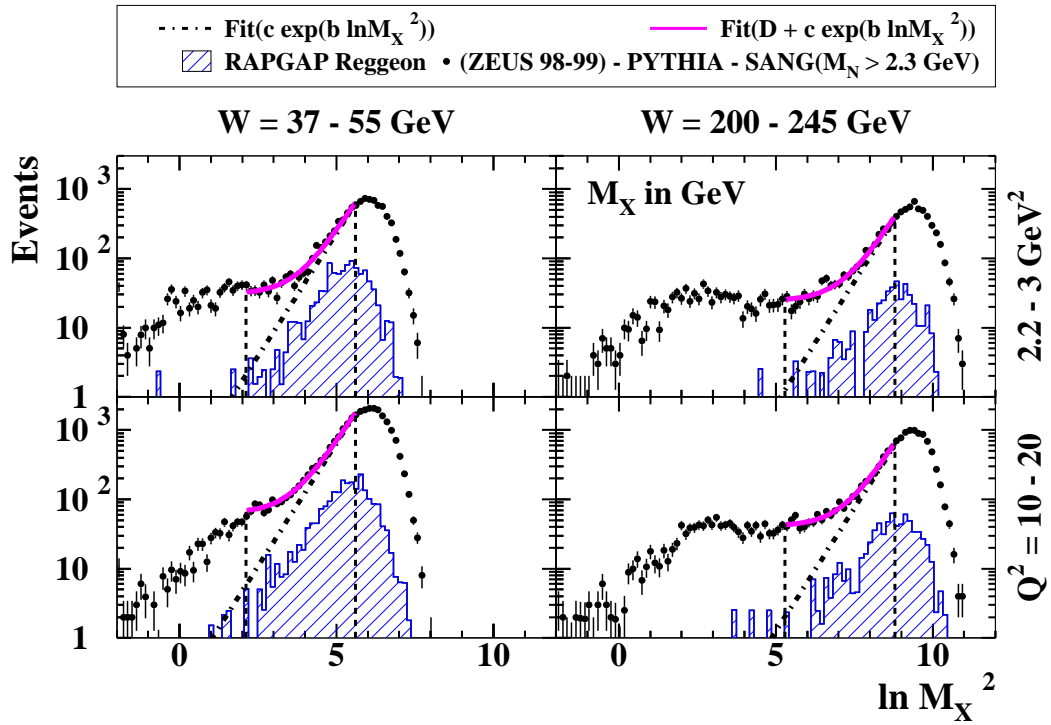


Figure 6: Distributions of $\ln M_X^2$ (M_X in units of GeV) at the detector level for different (W, Q^2) bins. The points with error bars show the data. The hatched histograms show the contributions predicted by the exchange of the ρ -Reggeon trajectory. The dash-dotted lines show the results for the non-diffractive contribution from fitting the sum of the diffractive and non-diffractive contributions in the $\ln M_X^2$ range delimited by the two vertical dashed lines.

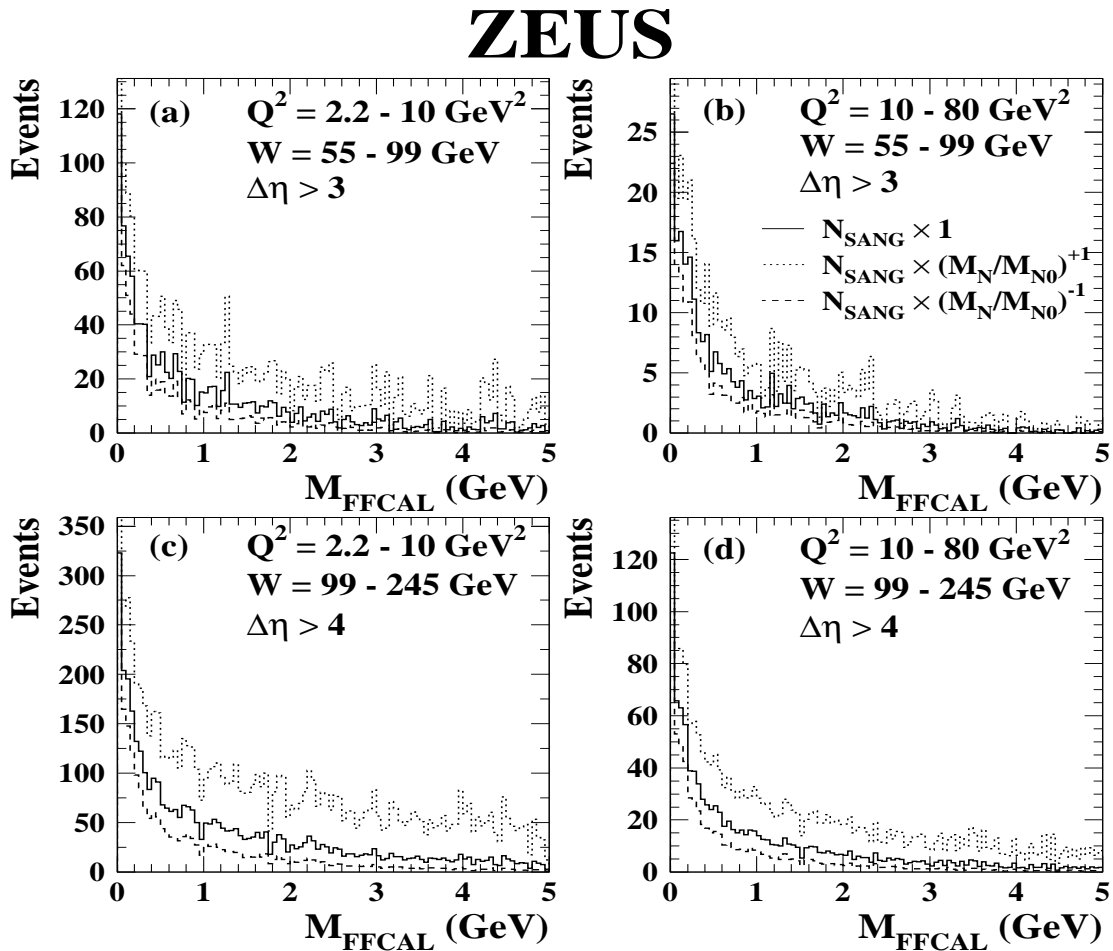


Figure 7: The M_{FFCAL} distributions predicted by SANG (solid histograms), weighted by an extra factor $(\frac{M_N}{M_{N0}})^{-1}$ (dashed histograms) or by $(\frac{M_N}{M_{N0}})^{+1}$ (dotted histograms), where $M_{N0} = 2.3 \text{ GeV}$. The M_{FFCAL} distributions are shown for four different regions of W, Q^2 and $\Delta\eta$.

ZEUS

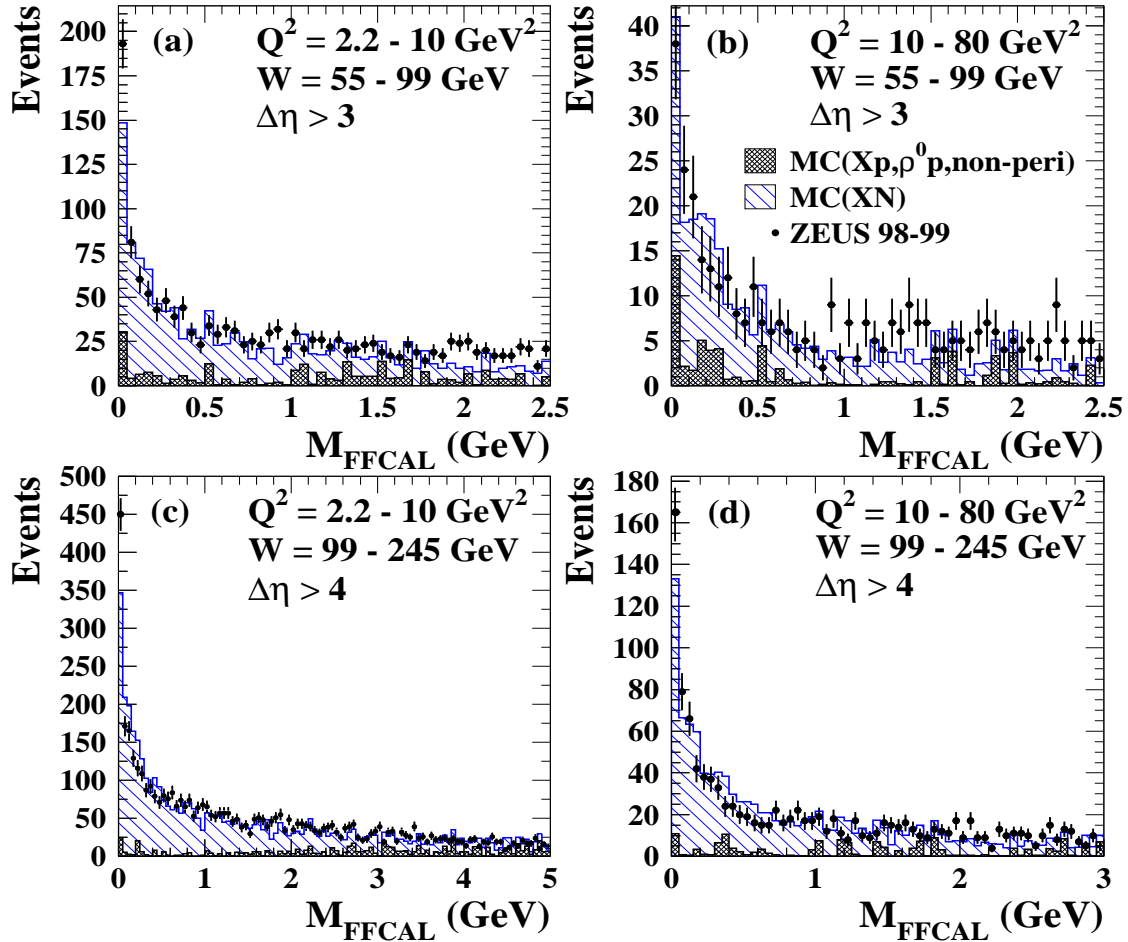


Figure 8: Distributions of M_{FFCAL} for four different $(W, Q^2, \Delta\eta)$ regions. The points with error bars show the data. The hatched histograms show the MC predictions for the contribution from diffractive double dissociation (XN); the cross-hatched histograms show the sum of the contributions from Xp , $\rho^0 p$ and non-peripheral processes.

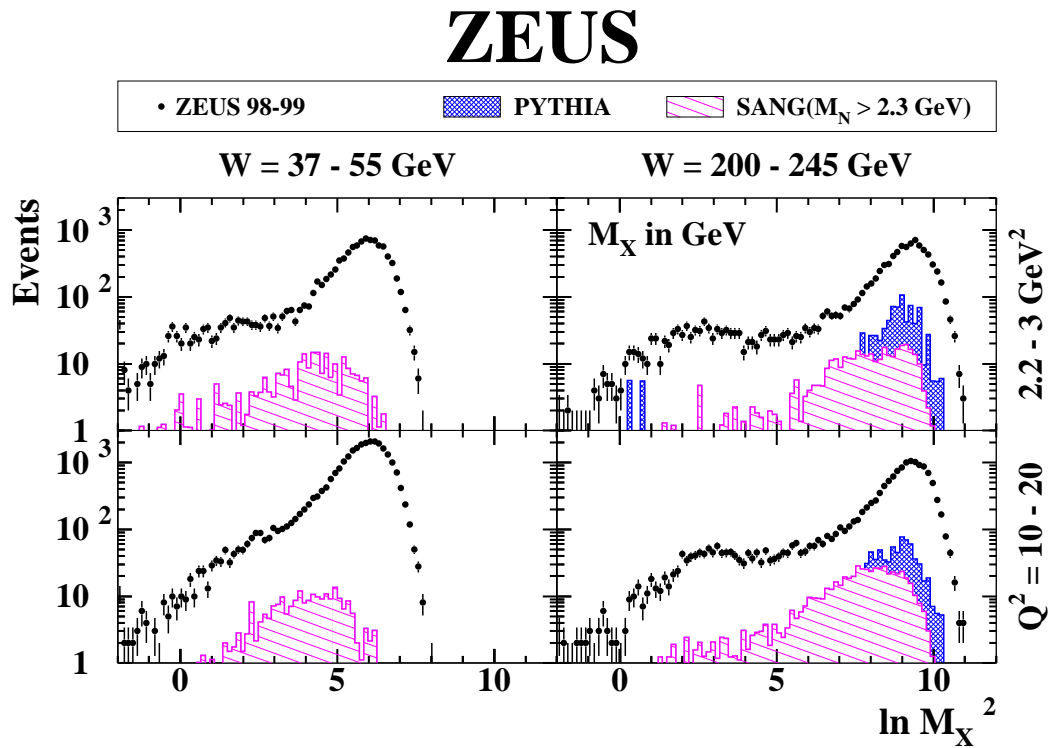
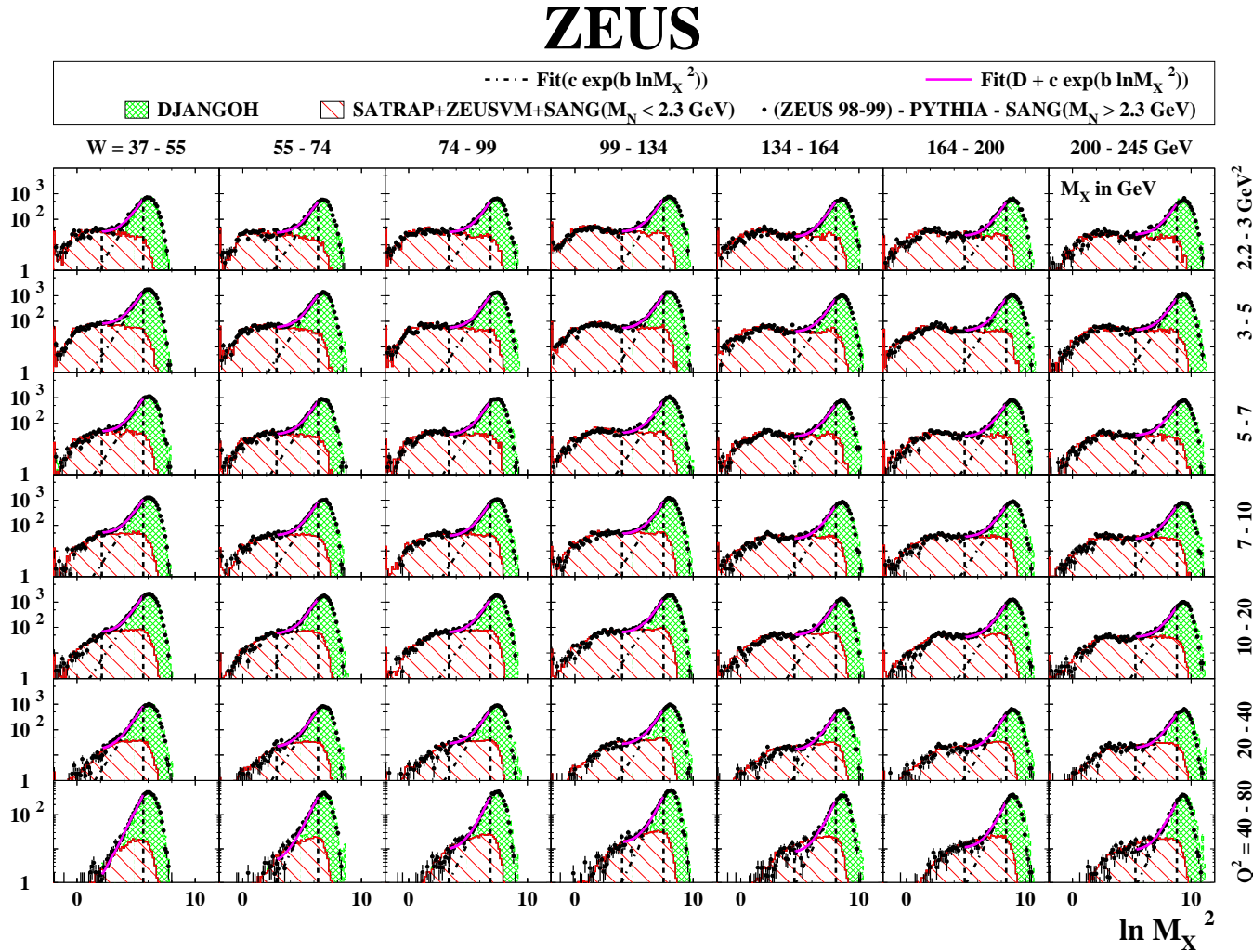


Figure 9: Distributions of $\ln M_X^2$ (M_X in units of GeV) at the detector level for different (W, Q^2) bins. The points with error bars show the data. The hatched histograms show the expectation for the contribution from diffractive double dissociation, $\gamma^*p \rightarrow XN$, where N has a mass more than 2.3 GeV, as predicted by SANG. The cross-hatched histograms show the background expected from photoproduction determined with PYTHIA.

Events

Figure 10: *Distributions of $\ln M_X^2$ (M_X in units of GeV) at the detector level for different (W , Q^2) bins. The full points with error bars show the data. The diffractive contributions from $\gamma^* p \rightarrow XN$, $M_N < 2.3$ GeV, as predicted by SATRAP+ZEUSVFM+SANG are shown by the hatched histograms. The cross-hatched histograms show the non-peripheral contributions as predicted by DJANGOH. The dash-dotted lines show the results for the non-diffractive contribution from fitting the data in the $\ln M_X^2$ range delimited by the two vertical dashed lines.*



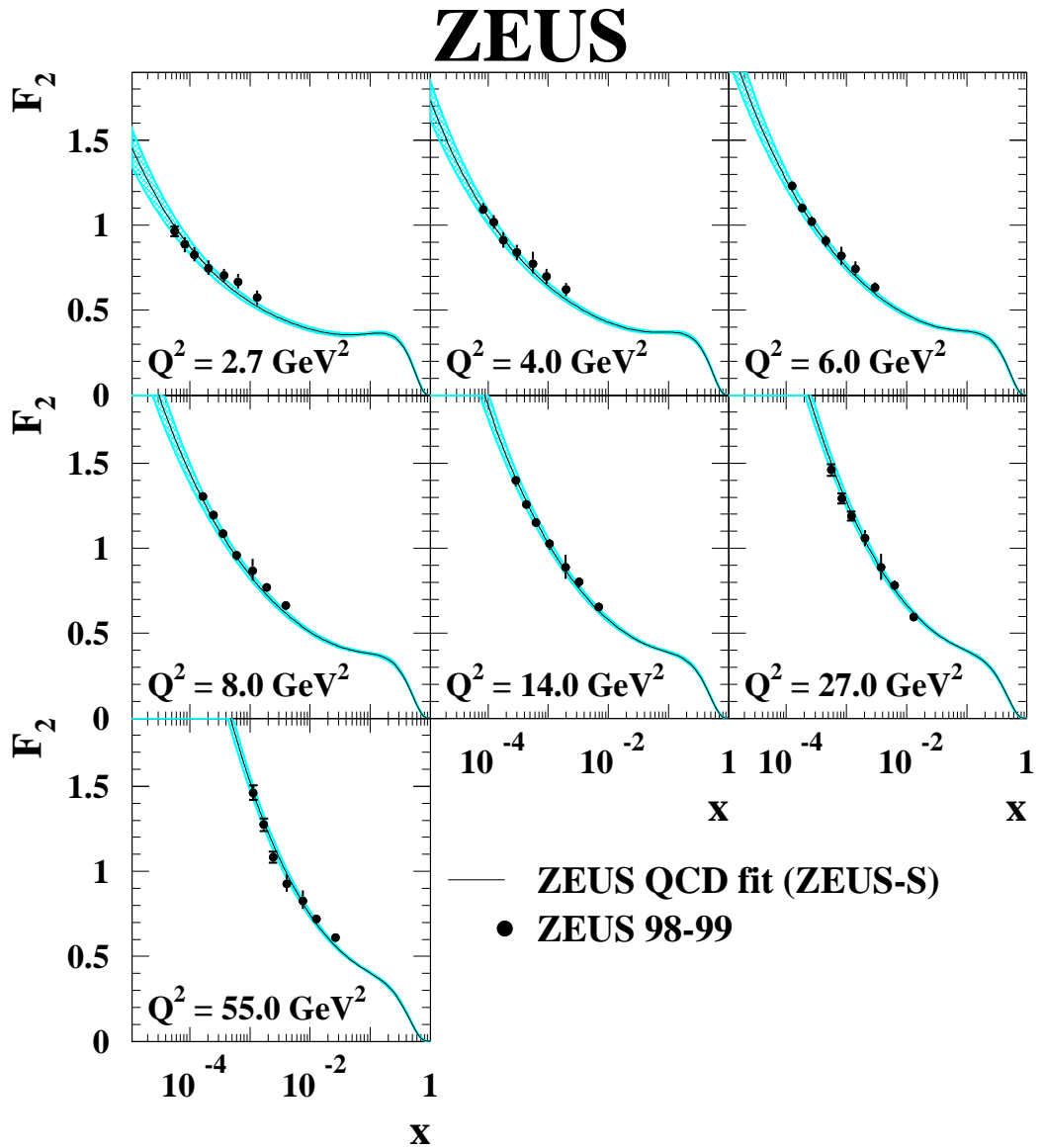


Figure 11: The proton structure function F_2 determined in this analysis for the Q^2 values indicated. The inner error bars show the statistical uncertainties and the full bars the statistical and systematic systematic uncertainties added in quadrature. The line shows the result of ZEUS QCD fit with its uncertainty band.

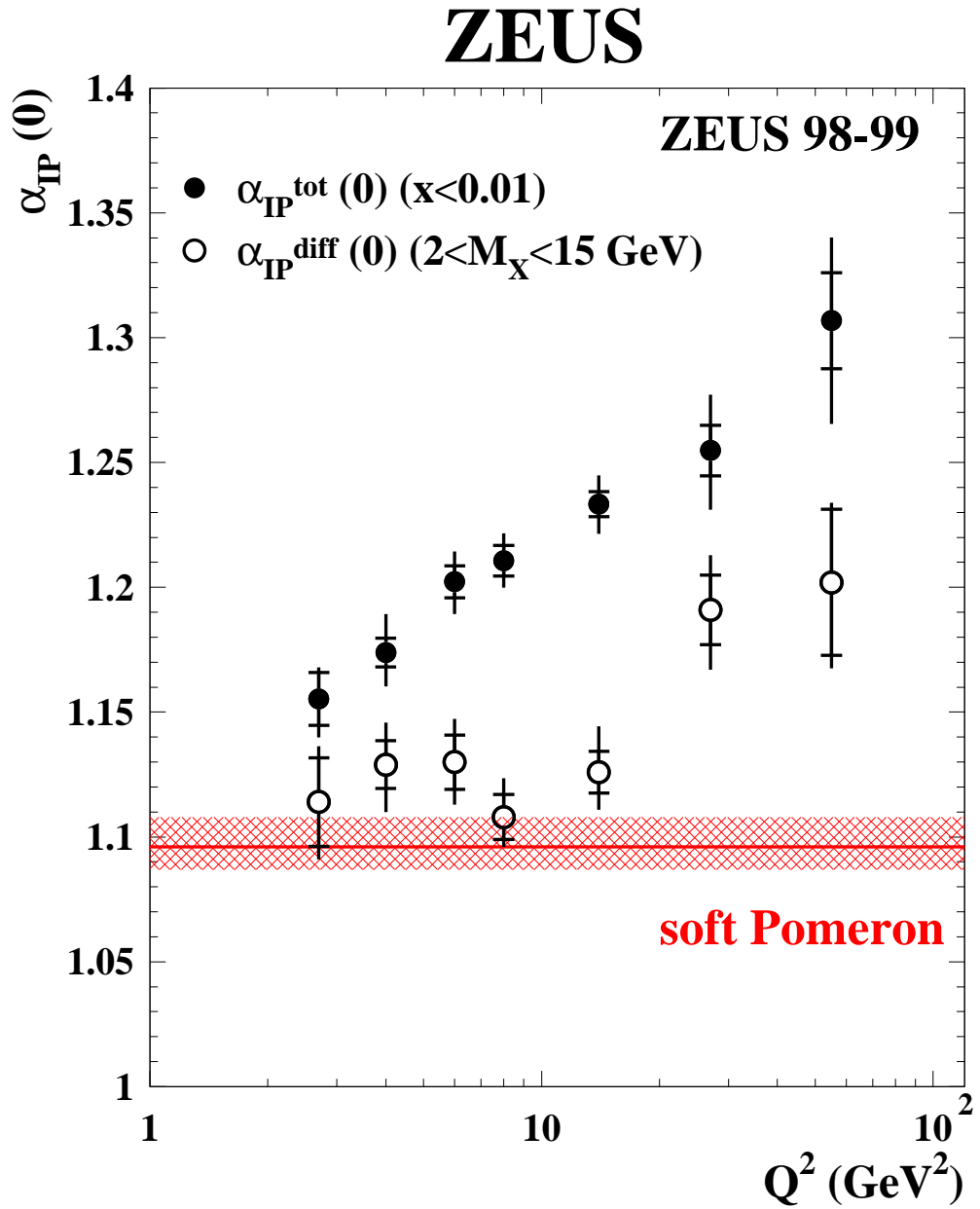


Figure 12: The intercepts of the Pomeron trajectory, $\alpha_{IP}^{\text{tot}}(0)$ and $\alpha_{IP}^{\text{diff}}(0)$, as a function of Q^2 , obtained from the W dependences of the total γ^*p cross section and of the diffractive cross section, $d\sigma_{\gamma^*p \rightarrow XN}^{\text{diff}}/dM_X$ for $2 < M_X < 15$ GeV. The inner error bars show the statistical uncertainties and the full bars the combined statistical and systematic systematic uncertainties. The $\alpha_{IP}(0)$ values for the latter were corrected for the t dependence of $\alpha_{IP}^{\text{diff}}$. The cross-hatched band shows the expectation for the soft Pomeron.

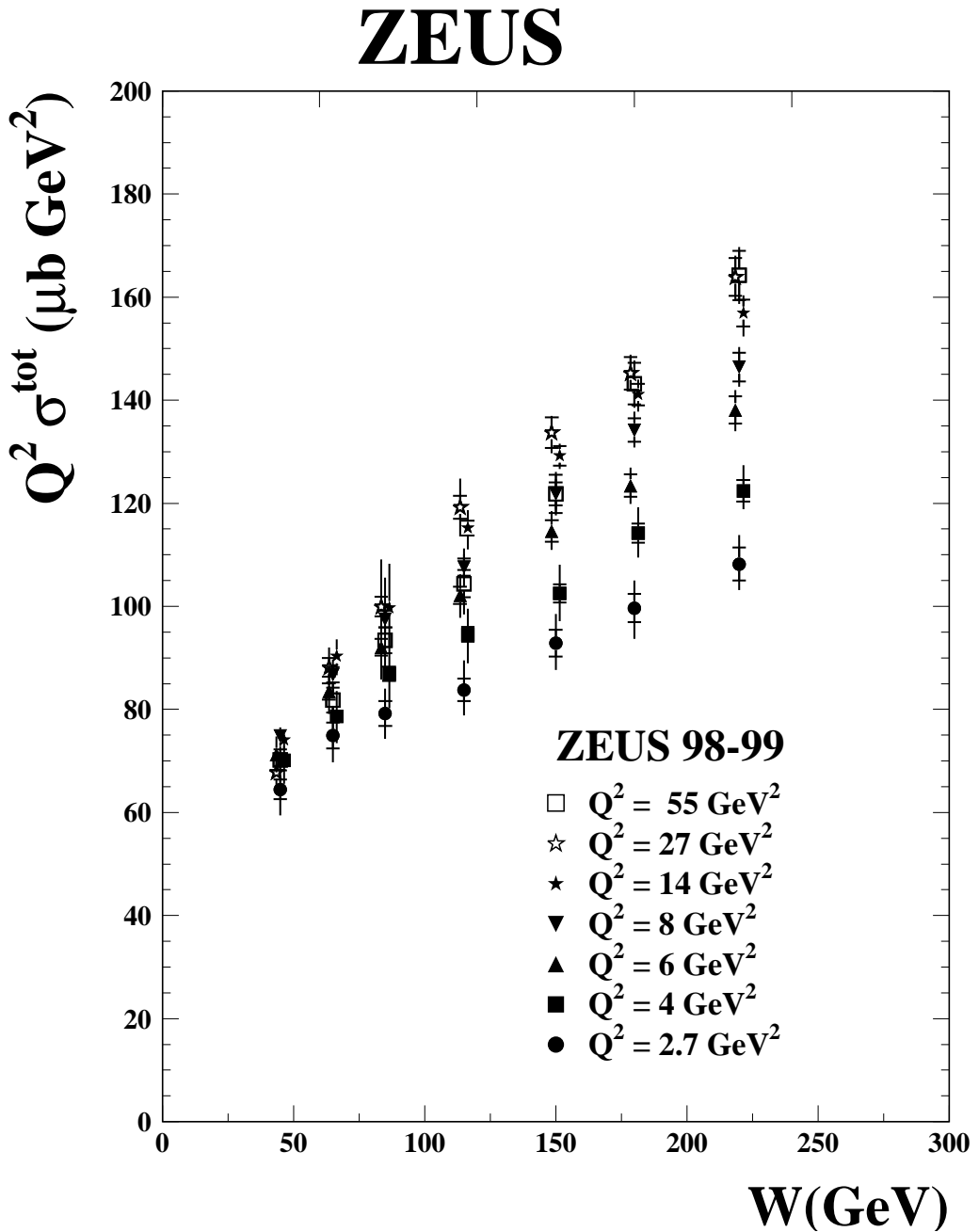


Figure 13: The total virtual photon-proton cross section, $\sigma_{\gamma^* p}^{\text{tot}}$, multiplied by Q^2 , as a function of W , for the Q^2 intervals indicated. The inner error bars show the statistical uncertainties and the full bars the statistical and systematic systematic uncertainties added in quadrature. For better visibility, the points for adjacent values of Q^2 were shifted in W by zero, $+1.5$ GeV or -1.5 GeV.

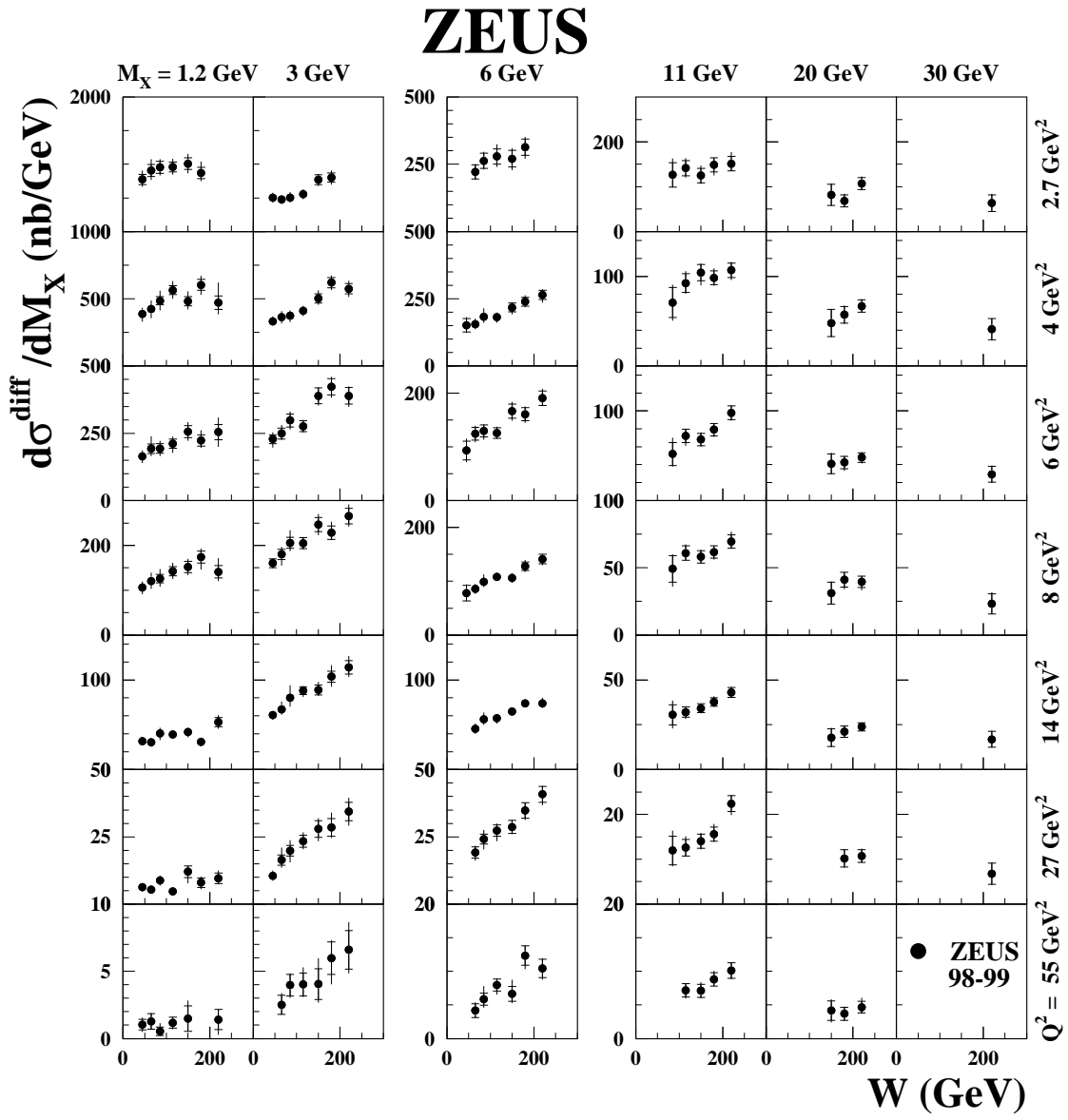


Figure 14: The differential cross sections, $d\sigma_{\gamma^* p \rightarrow XN}^{\text{diff}}/dM_X$, $M_N < 2.3$ GeV, as a function of W for bins of M_X and Q^2 . The inner error bars show the statistical uncertainties and the full bars the statistical and systematic uncertainties added in quadrature.

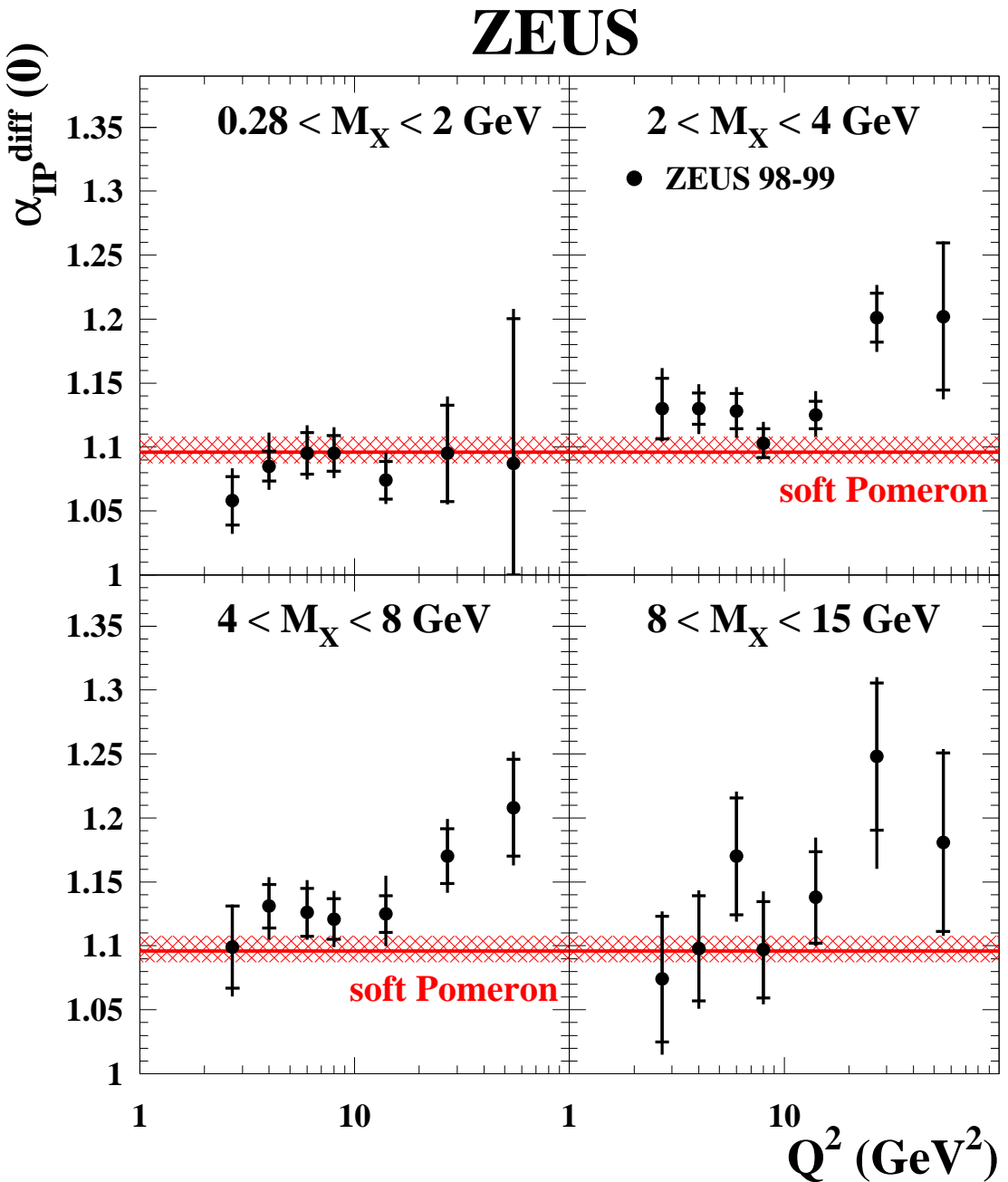


Figure 15: The intercept $\alpha_{IP}^{\text{diff}}(0)$, obtained from fitting the diffractive cross section, $d\sigma_{\gamma^* p \rightarrow XN}^{\text{diff}}(M_X, W, Q^2)/dM_X$, as a function of Q^2 for the different M_X bins. The inner error bars show the statistical uncertainties and the full bars the combined statistical and systematic systematic uncertainties. The cross-hatched band shows the expectation for the soft Pomeron, see text.

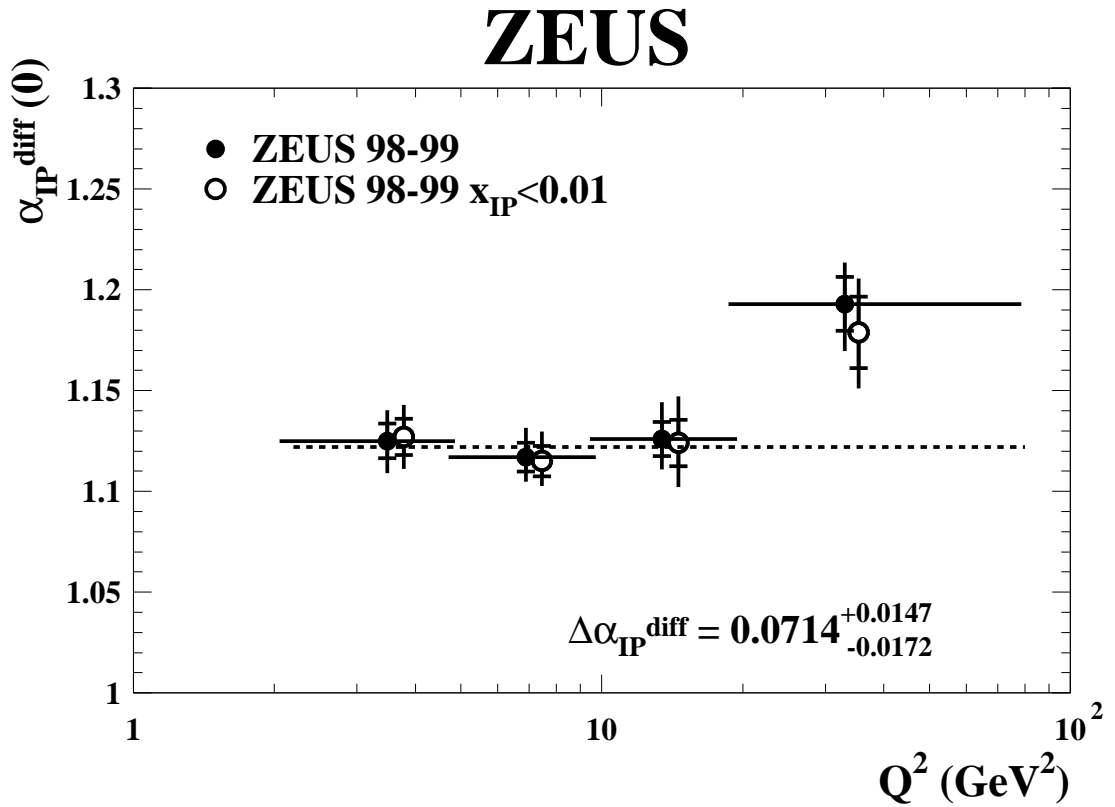


Figure 16: The Q^2 dependence of $\alpha_{IP}^{\text{diff}}(0)$ as determined from fitting the W dependence of the diffractive cross section for $2 < M_X < 15$ GeV. The inner error bars show the statistical uncertainties and the full bars the combined statistical and systematic systematic uncertainties. The horizontal bars represent the bin widths. The open symbol indicates the results which were determined using the diffractive cross section with $x_{IP} < 0.01$. For better visibility, the points obtained from the same Q^2 range were shifted in Q^2 by 4 % and -4 %. The dashed line shows $\alpha_{IP}^{\text{diff}}(0)$ averaged over $2.2 < Q^2 < 20$ GeV 2 . The difference $\Delta\alpha_{IP}^{\text{diff}}$ is defined as $\alpha_{IP}^{\text{diff}}(0, \langle Q^2 \rangle = 34.6 \text{ GeV}^2) - \alpha_{IP}^{\text{diff}}(0, \langle Q^2 \rangle = 7.8 \text{ GeV}^2)$.

ZEUS

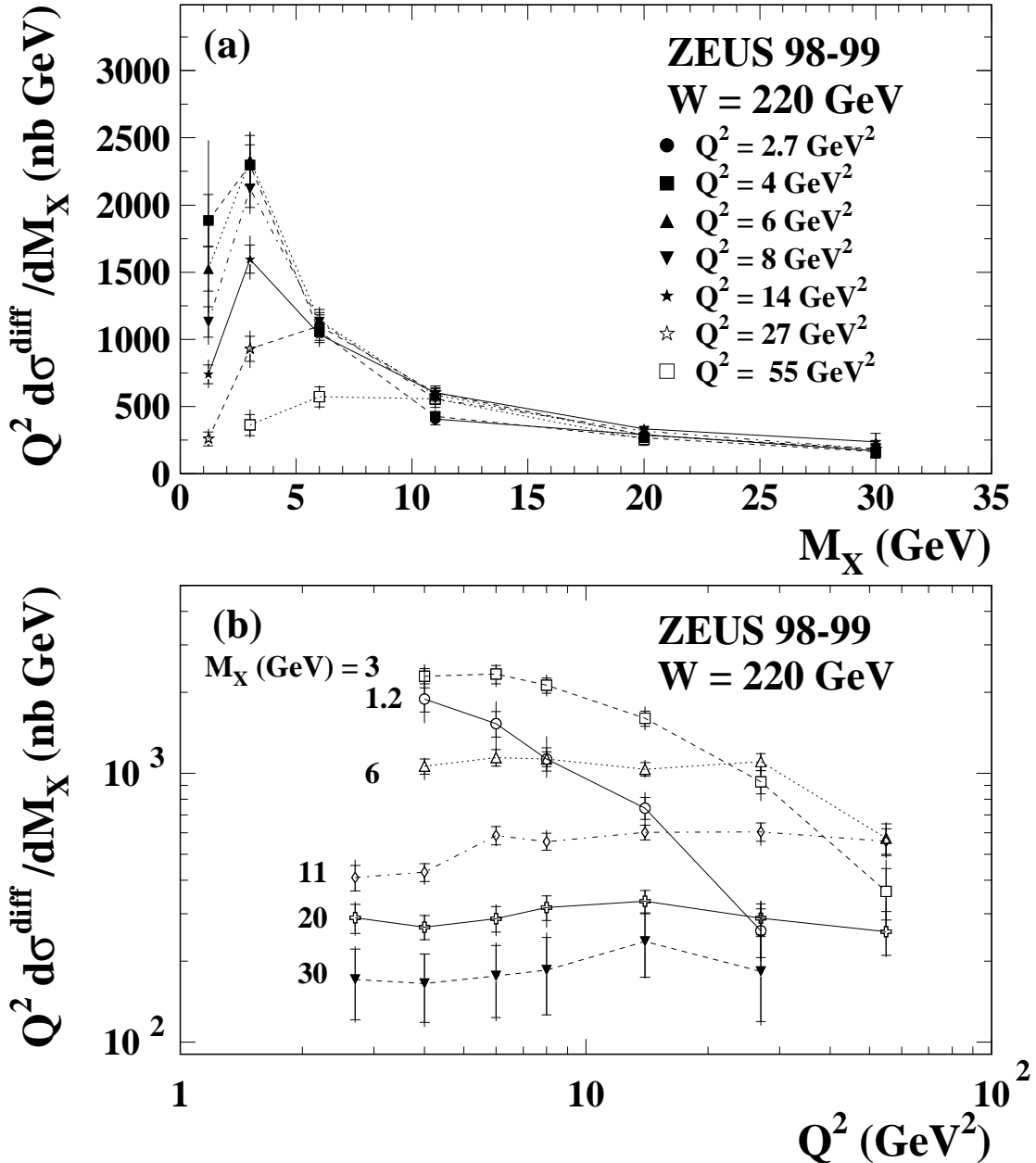


Figure 17: The diffractive cross section multiplied by Q^2 , $Q^2 d\sigma_{\gamma^* p \rightarrow XN}^{\text{diff}} / dM_X$, $M_N < 2.3 \text{ GeV}$, for $W = 220 \text{ GeV}$: (a) as a function of M_X for the Q^2 intervals indicated; the lines connect the points measured for the same value of Q^2 ; (b) as a function of Q^2 for the M_X intervals indicated; the lines connect the points measured for the same value of M_X . The inner error bars show the statistical uncertainties and the full bars the statistical and systematic uncertainties added in quadrature.

ZEUS

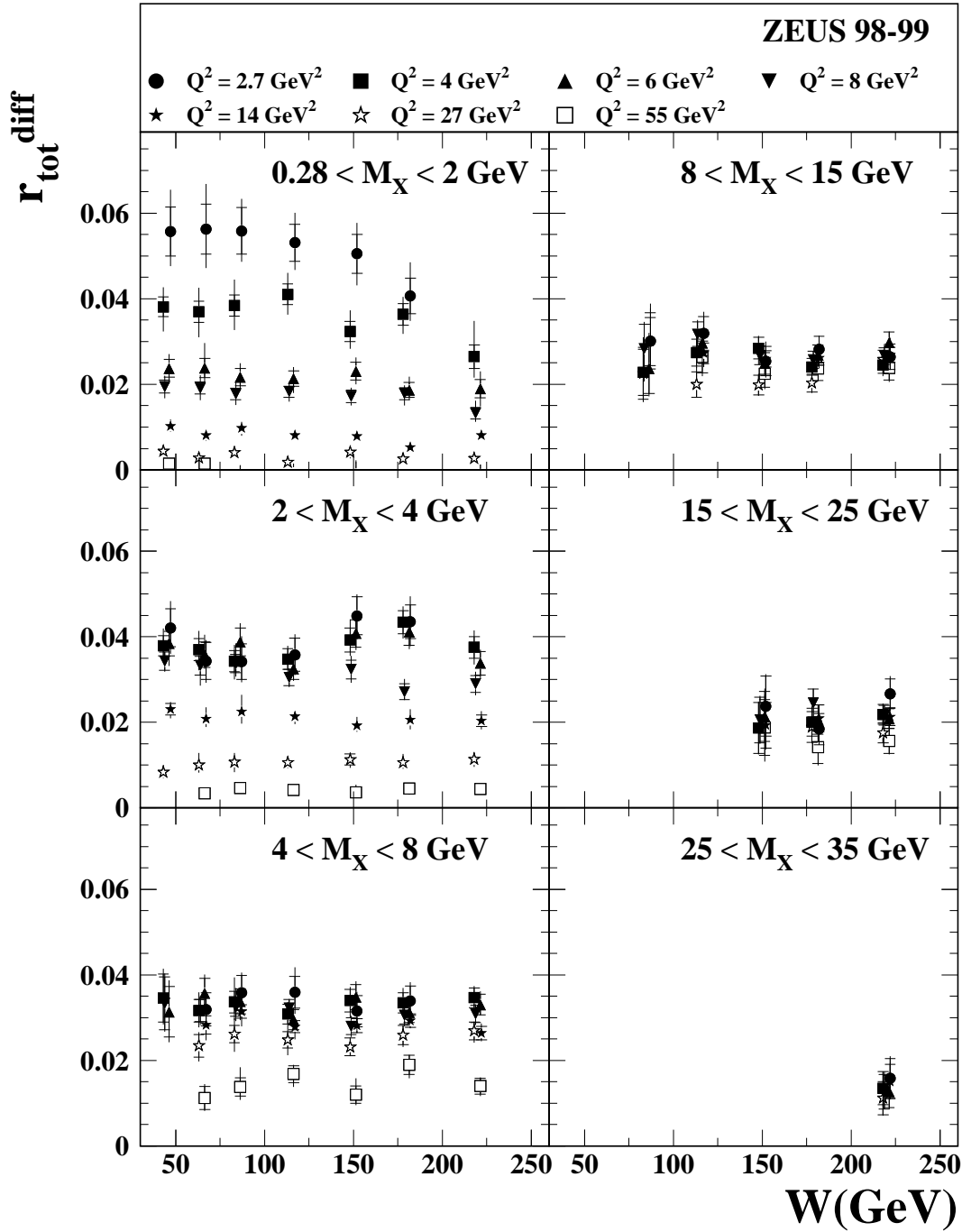


Figure 18: The ratio of the diffractive cross section, integrated over the M_X intervals indicated, $\int_{M_a}^{M_b} dM_X d\sigma_{\gamma^* p \rightarrow X N, M_N < 2.3 \text{ GeV}}^{\text{diff}} / dM_X$, to the total $\gamma^* p$ cross section, $r_{\text{tot}}^{\text{diff}} = \sigma^{\text{diff}} / \sigma_{\gamma^* p}^{\text{tot}}$, as a function of W for the M_X and Q^2 intervals indicated. The inner error bars show the statistical uncertainties and the full bars the statistical and systematic uncertainties added in quadrature.

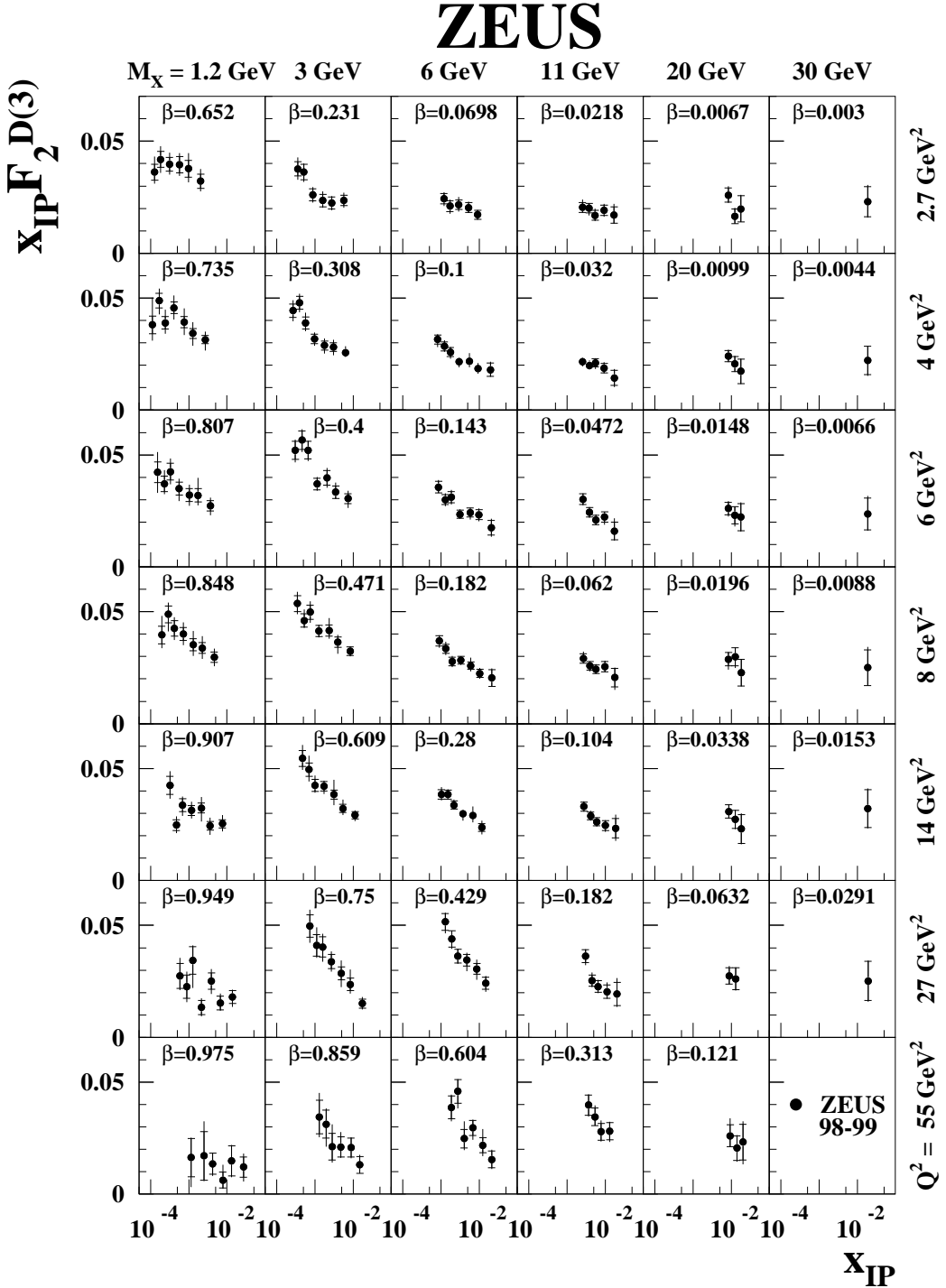


Figure 19: The diffractive structure function of the proton multiplied by x_{IP} , $x_{IP} F_2^{D(3)}$, for $\gamma^* p \rightarrow XN$, $M_N < 2.3$ GeV as a function of x_{IP} for different regions of β and Q^2 . The inner error bars show the statistical uncertainties and the full bars the statistical and systematic uncertainties added in quadrature.

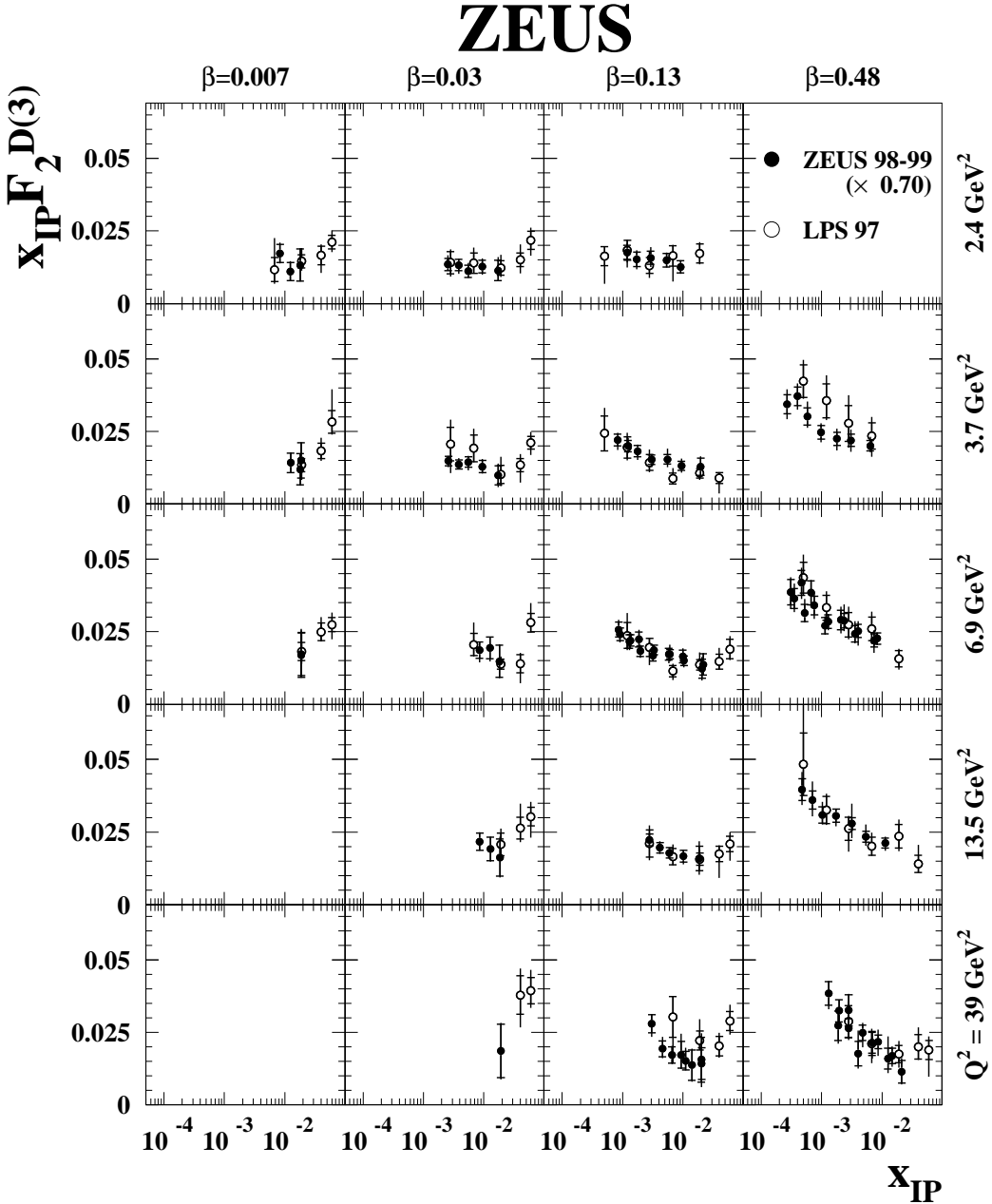


Figure 20: The diffractive structure function of the proton multiplied by x_{IP} , $x_{IP} F_2^{D(3)}$, from this analysis multiplied by a factor 0.70 to account for the contribution from diffractive nucleon dissociation with $M_N < 2.3$ GeV (solid points), compared with the results from the ZEUS LPS measurement. The inner error bars show the statistical uncertainties and the full bars the statistical and systematic uncertainties added in quadrature. For ease of comparison, the results from this analysis have been transported to the (β, Q^2) values used by the ZEUS LPS analysis (open points). Only bins of (β, Q^2) in which both analyses have results are shown.

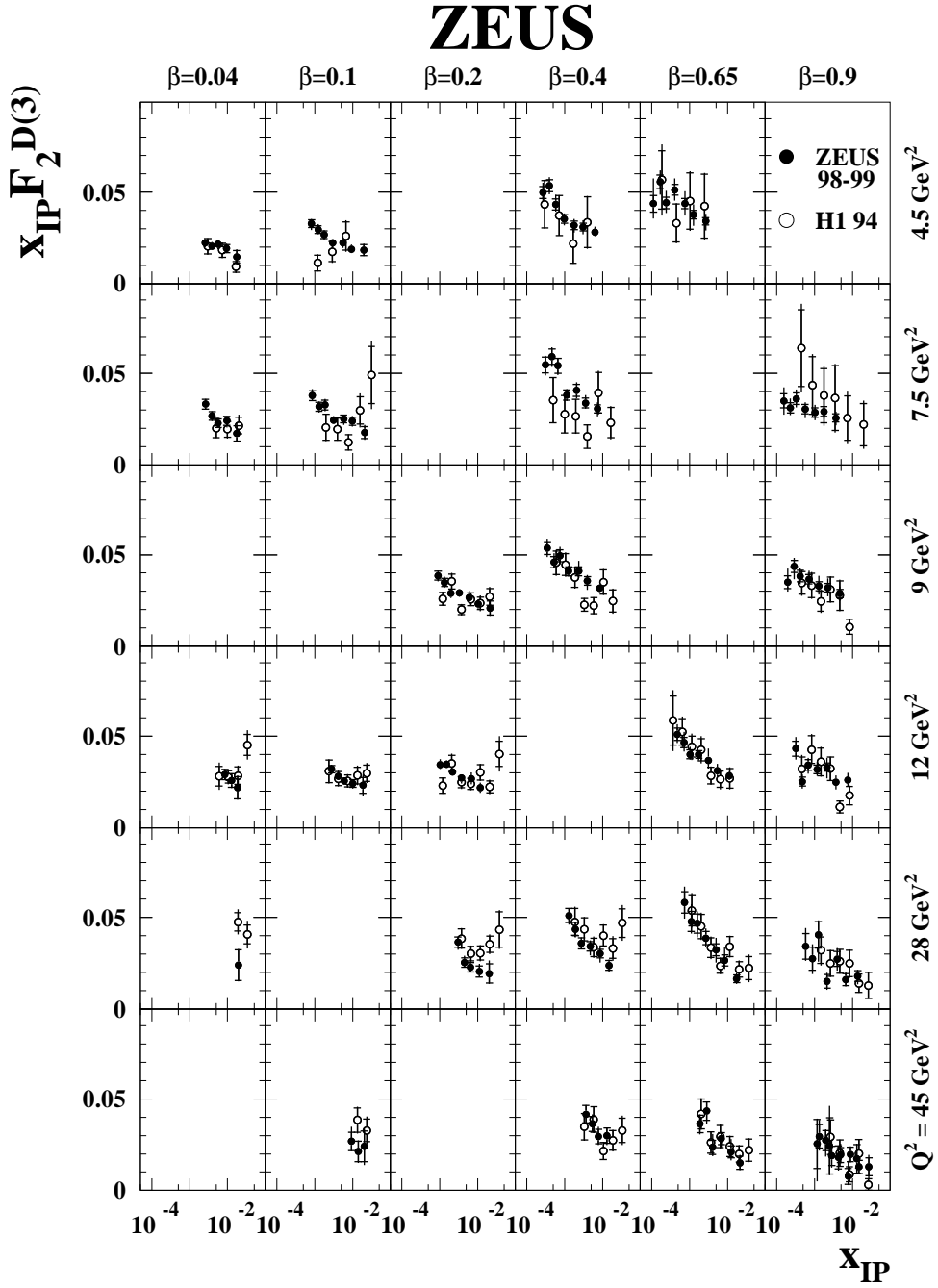


Figure 21: The diffractive structure function of the proton multiplied by x_{IP} , $x_{IP} F_2^{D(3)}$, from this analysis for $\gamma^* p \rightarrow XN$, $M_N < 2.3$ GeV (solid points) compared with the H1 results given for $M_N < 1.6$ GeV (open points). The inner error bars show the statistical uncertainties and the full bars the statistical and systematic systematic uncertainties added in quadrature. For ease of comparison, the results from this analysis have been transposed to (β, Q^2) values used by the H1 analysis. Only bins of (β, Q^2) in which both analyses have results are shown.

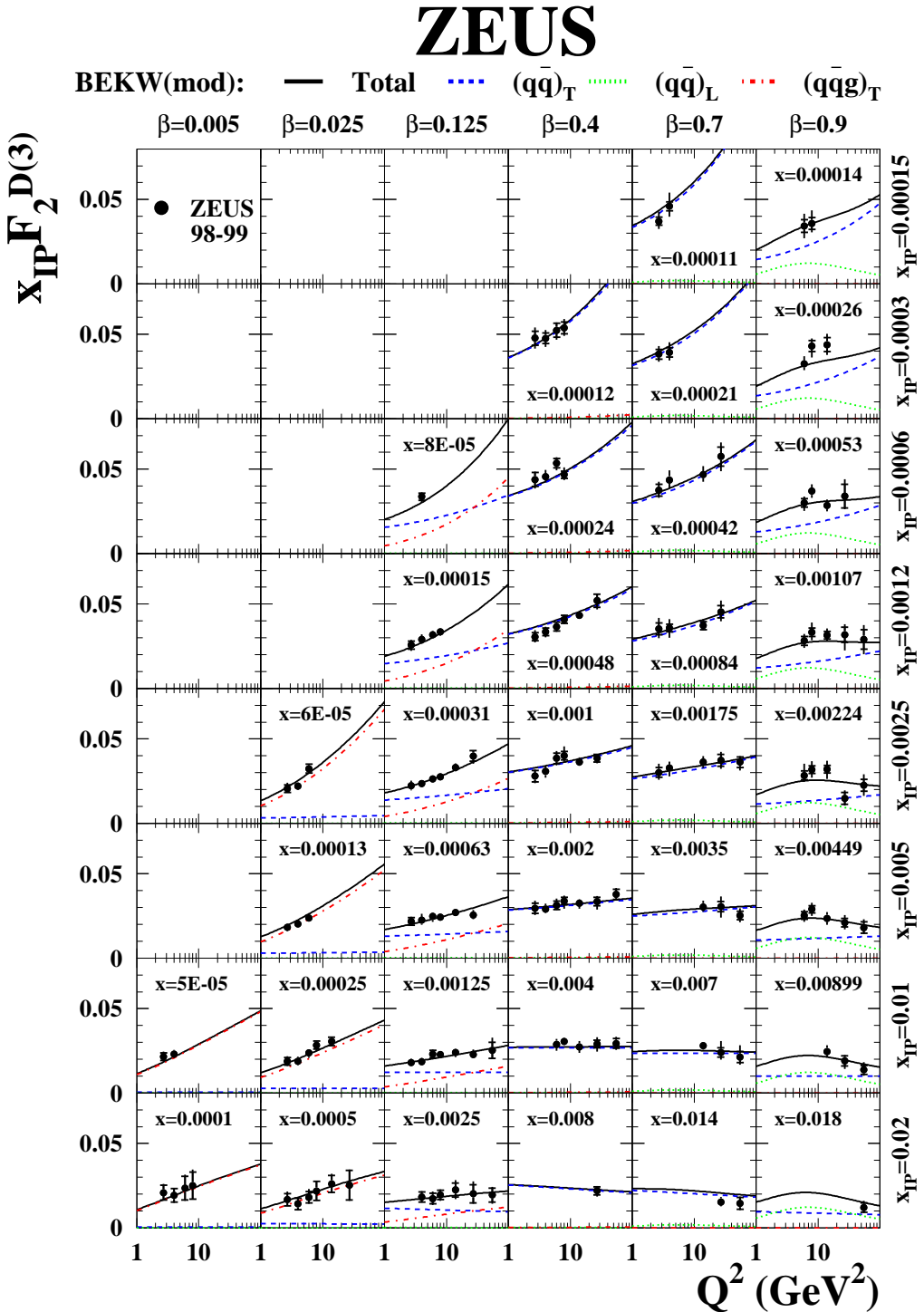
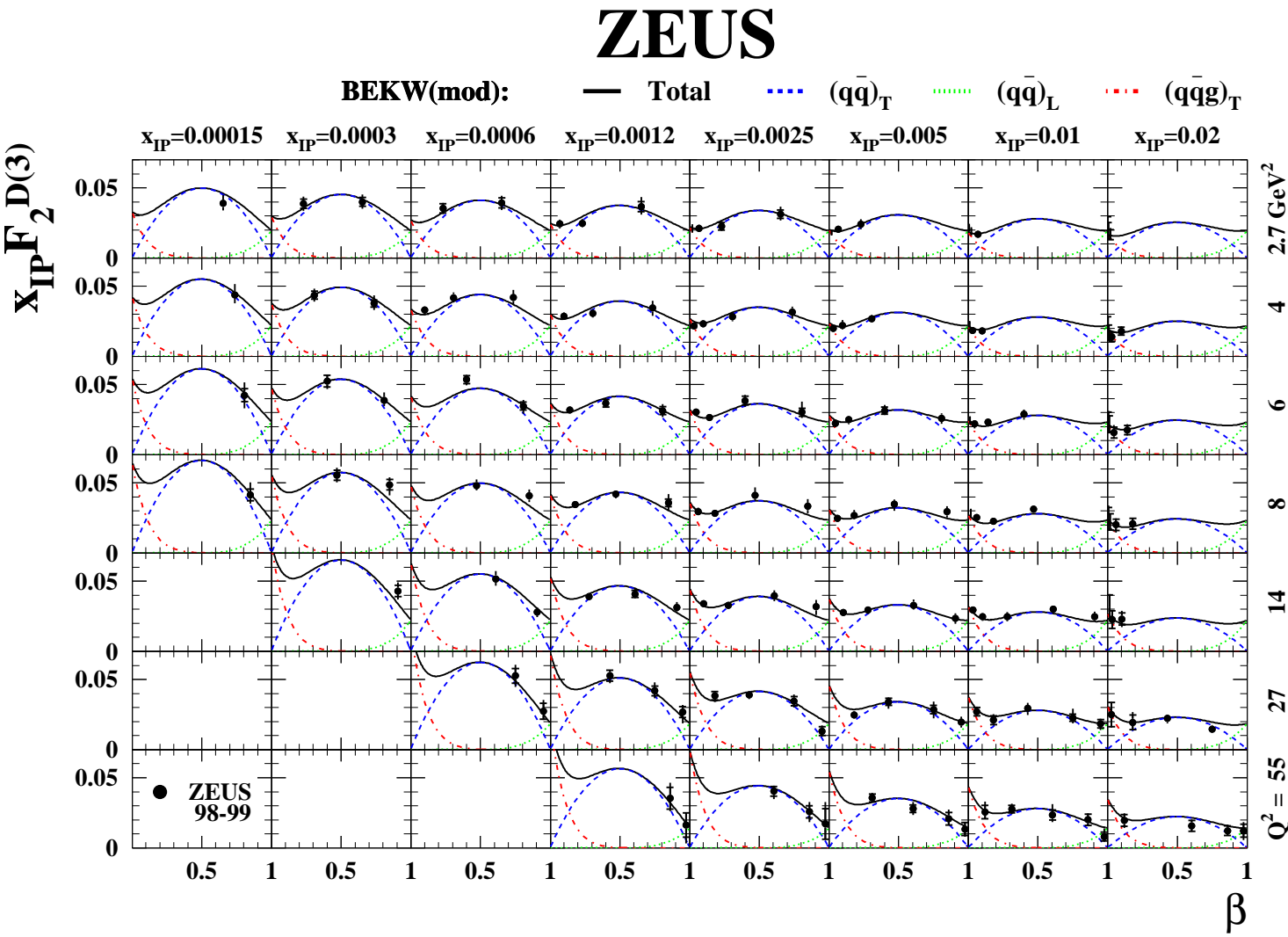


Figure 22: The diffractive structure function of the proton multiplied by $x_P x_P F_2^{D(3)}$, as a function of Q^2 for different regions of β and x_P . The inner error bars show the statistical uncertainties and the full bars the statistical and systematic uncertainties added in quadrature. The curves show the result of the BEKW(mod) fit for the contributions from $(q\bar{q})$ for transverse (dashed) and longitudinal photons (dotted) and for the $(q\bar{q}g)$ contribution for transverse photons (dashed-dotted) together with the sum of all contributions (solid).

Figure 23: The diffractive structure function of the proton multiplied by x_p , $x_p F_2^{D(3)}$, as a function of β for different regions of Q^2 and x_p . The inner error bars show the statistical uncertainties and the full bars the statistical and systematic systematic uncertainties added in quadrature. The curves show the result of the BEKW(mod) fit for the contributions from $(q\bar{q})$ for transverse (dashed) and longitudinal photons (dotted) and for the $(q\bar{q}g)$ contribution for transverse photons (dashed-dotted) together with the sum of all contributions (solid).



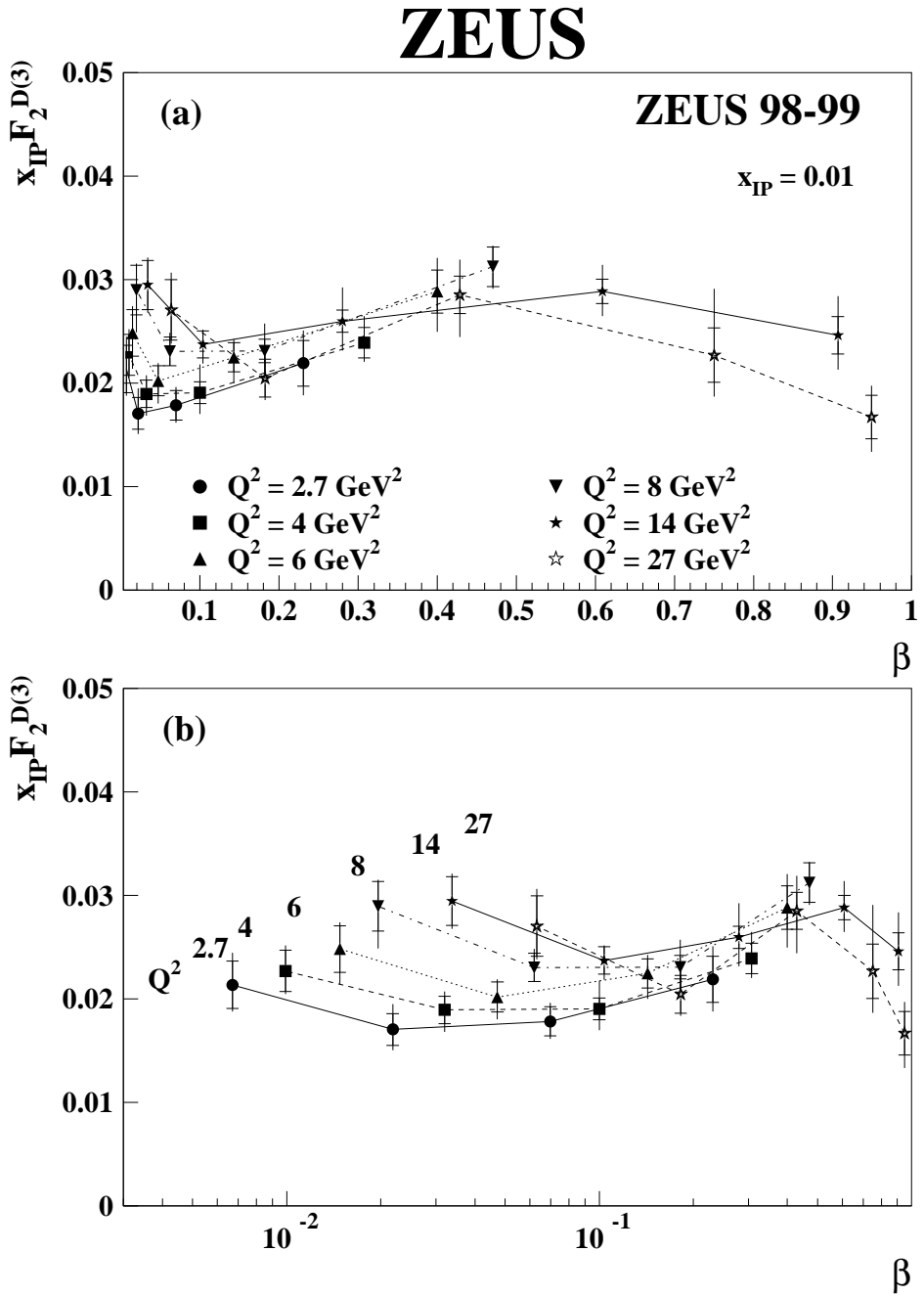


Figure 24: The diffractive structure function of the proton multiplied by x_{IP} , $x_{IP} F_2^{D(3)}$, for $x_{IP} = 0.01$ as a function of β for the Q^2 intervals indicated, (a) on a linear scale, (b) on a logarithmic scale. The inner error bars show the statistical uncertainties and the full bars the statistical and systematic systematic uncertainties added in quadrature. The lines connect measurement at the same value of Q^2 .

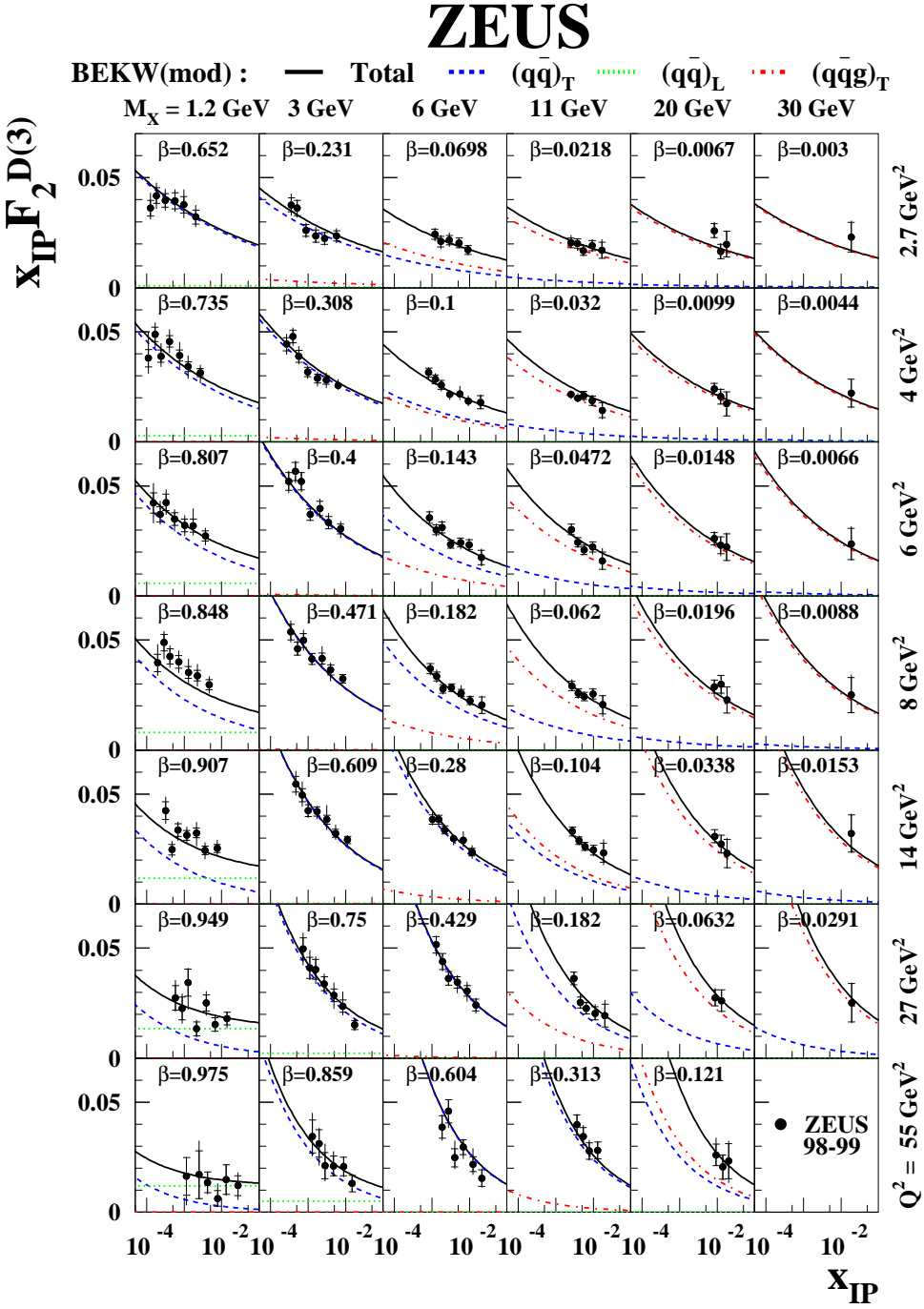


Figure 25: The diffractive structure function of the proton multiplied by x_{IP} , $x_{IP} F_2^{D(3)}$, as a function of x_{IP} for different regions of β and Q^2 . The inner error bars show the statistical uncertainties and the full bars the statistical and systematic systematic uncertainties added in quadrature. The curves show the result of the BEKW fit for the contributions from $(q\bar{q})$ for transverse (dashed) and longitudinal photons (dotted) and for the $(q\bar{q}g)$ contribution for transverse photons (dashed-dotted) together with the sum of all contributions (solid).